Charged multihadron systems in lattice QCD + QED

S. R. Beane,[1] W. Detmold,[2] R. Horsley[●],[3] M. Illa[●],[4] M. Jafry[●],[1] D. J. Murphy,[2] Y. Nakamura,[5] H. Perlt[●],[6] P. E. L. Rakow,[7] G. Schierholz[●],[8] P. E. Shanahan,[2] H. Stüben,[9] M. L. Wagman[●],[2,10] F. Winter[●],[11] R. D. Young,[12] and J. M. Zanotti[12]

(NPLQCD and QCDSF collaborations)

[1]*Department of Physics, University of Washington, Box 351560, Seattle, Washington, D.C. 98195, USA*
[2]*Center for Theoretical Physics, Massachusetts Institute of Technology,*
Cambridge, Massachusetts 02139, USA
[3]*School of Physics and Astronomy, University of Edinburgh, Edinburgh EH9 3FD, United Kingdom*
[4]*Departament de Física Quàntica i Astrofísica, Institut de Ciènces del Cosmos (ICCUB),*
Universitat de Barcelona, Martí Franquès 1, E08028 Barcelona, Spain
[5]*RIKEN Center for Computational Science, Kobe, Hyogo 650-0047, Japan*
[6]*Institut für Theoretische Physik, Universität Leipzig, 04109 Leipzig, Germany*
[7]*Theoretical Physics Division, Department of Mathematical Sciences, University of Liverpool,*
Liverpool L69 3BX, United Kingdom
[8]*Deutsches Elektronen-Synchrotron DESY, 22603 Hamburg, Germany*
[9]*Regionales Rechenzentrum, Universität Hamburg, 20146 Hamburg, Germany*
[10]*Fermi National Accelerator Laboratory, Batavia, Illinois 60510, USA*
[11]*Jefferson Laboratory, 12000 Jefferson Avenue, Newport News, Virginia 23606, USA*
[12]*CSSM, Department of Physics, University of Adelaide, Adelaide, SA 5005, Australia*

Systems with the quantum numbers of up to 12 charged and neutral pseudoscalar mesons, as well as one-, two-, and three-nucleon systems, are studied using dynamical lattice quantum chromodynamics and quantum electrodynamics (QCD + QED) calculations and effective field theory. QED effects on hadronic interactions are determined by comparing systems of charged and neutral hadrons after tuning the quark masses to remove strong isospin breaking effects. A nonrelativistic effective field theory, which perturbatively includes finite-volume Coulomb effects, is analyzed for systems of multiple charged hadrons and found to accurately reproduce the lattice QCD + QED results. QED effects on charged multihadron systems beyond Coulomb photon exchange are determined by comparing the two- and three-body interaction parameters extracted from the lattice QCD + QED results for charged and neutral multihadron systems.

I. INTRODUCTION

The interplay between the strong and electromagnetic (EM) interactions of the Standard Model is subtle but central to the complexity of visible matter. While EM interactions are typically much weaker than the strong interactions, it is their competition with strong isospin breaking effects that leads to the observed proton-neutron mass difference and determines the stability of atomic nuclei. Moreover, the hierarchy between the length scales where strong and EM

interactions are important leads to the existence of chemistry and all of the complexity that it entails. Progress towards understanding the combined effects of the strong and EM interactions from first principles has been made in recent years, and the EM–strong interaction decomposition of the neutron-proton mass difference, $M_n - M_p$, has been calculated from the Standard Model for the first time using the numerical lattice formulation of quantum chromodynamics (QCD) and quantum electrodynamics (QED) [1–3]. Coupled lattice QCD + QED calculations have also been performed for meson and baryon masses [4–7], leptonic decay rates [8–10], and the anomalous magnetic moment of the muon [11–20], as both QCD and QED must be accounted for in precision tests of the Standard Model.

Systems of multiple charged hadrons exhibit rich phenomenology in which the interplay between QCD and

QED effects is less well understood than for single-hadron systems. The differences between pp, np, and nn two-nucleon scattering channels are much more poorly constrained than their isospin average. Lattice QCD + QED can potentially provide phenomenologically useful information on such isospin breaking effects in nucleon-nucleon scattering; furthermore, calculations with a range of quark masses and values of the QED fine structure constant can provide insight into the fine-tuning of QED effects and strong isospin breaking interactions, providing complementary information to the experiment. In large nuclei with charge $Z \sim 1/\alpha$, where α is the EM fine structure constant, relativistic QED effects are expected to become nonperturbative and give rise to electron-positron pair production and interesting consequences for the structure of elements [21].

QCD + QED studies of systems involving two or more protons are of great phenomenological interest, but calculations of large nuclei are difficult using current lattice QCD + QED techniques [22]. It is also interesting to consider systems of multiple charged mesons, which allow an investigation of similar QED effects without a number of the numerical complexities of multiproton calculations. In particular, charged multihadron systems include QED effects that become nonperturbative for hadron pairs with sufficiently small relative velocity $v \ll \alpha$. All calculations of charged hadrons must also reconcile the presence of net charge in a finite volume (FV) with Gauss's law, which can be accomplished in several ways [1–3,5,6,8,9,19,23–38]. The current study makes use of the QED_L formulation [26], in which the photon spatial zero mode is removed, as has been recently studied in detail for single-hadron systems in Refs. [1–3,5,6,8,9,19,23–28,30,32–38]. Subtleties related to the nonlocality of zero-mode subtraction in QED_L have been understood for single-hadron systems [2,30,32,36,38,39], and similar methods are used to understand nonlocality in multihadron systems in this framework as described below.

In lattice QCD calculations, hadronic scattering phase shifts are determined by relating them to the FV energies of two-hadron systems using FV relations first derived by Lüscher [40,41] and generalized in recent years (see Ref. [42] for a review). Understanding scattering in lattice QCD + QED is complicated by the lack of a FV formalism that includes nonperturbative Coulomb effects and thereby relates FV energy shifts calculable in lattice QCD + QED to infinite-volume (Coulomb-corrected) scattering phase shifts. In the QED_L formulation, Ref. [43] argues that Coulomb effects can be treated perturbatively for sufficiently small volumes where $L \ll 1/(\alpha M)$, and therefore the Bohr radius of the charged-particle system is larger than the infrared cutoff provided by the FV. However, the volume must also satisfy $L \gg 1/M$ in order for relativistic FV effects not accounted for in Lüscher's analysis to be negligible. For some systems there may be a window of

intermediate-sized volumes where relativistic FV effects and nonperturbative Coulomb effects can both be neglected. Nonrelativistic effective field theory (EFT) can be used to investigate this issue and to relate FV energy shifts for systems with more than two particles to two-, three-, and higher-body EFT low-energy constants (LECs).

This work studies QCD + QED effects for systems of multiple hadrons including up to 12 charged or neutral mesons and up to three nucleons in multiple finite volumes. A larger than physical value of the fine-structure constant, $\alpha \simeq 0.1$, is used in order to increase the size of QED effects and permit the study of systems with total charge Z satisfying $Z\alpha \gtrsim 1$. As described in Ref. [4] and summarized below, the quark masses are tuned to remove strong isospin breaking effects so that splittings between particles that are degenerate in QCD can be identified as pure QED effects. Calculations are performed in both lattice QCD + QED_L (LQCD + QED_L) and in an EFT appropriate for nonrelativistic charged hadrons, referred to as nonrelativistic QED_L (NRQED$_L$) below. Two-body scattering lengths and three-body interactions of charged and neutral mesons are determined by tuning the hadronic interaction parameters appearing in the NRQED$_L$ Lagrangian to reproduce the LQCD + QED_L FV energy levels. QED effects on hadron interactions beyond Coulomb photon exchange are determined by comparing the two-body and three-body interaction parameters determined for charged and neutral mesons. Studies of multibaryon systems are used to probe volumes where $L > 1/(\alpha M)$ and Coulomb effects may not be perturbative according to the criteria of Ref. [43]. It is noteworthy that no significant nonperturbative Coulomb effects or relativistic effects are seen at the level of precision of the results obtained here, even for systems with $L > 1/(\alpha M)$ or $Z\alpha > 1$.

The practical window of L where relativistic effects can be neglected and Coulomb effects can be treated perturbatively is explored by comparing LQCD + QED_L and NRQED$_L$ results for a variety of FV systems. From these studies, it is argued that this window requires the spatial extent L of a cubic FV to satisfy

$$\frac{1}{ML} \ll 1, \qquad \frac{\alpha ML}{4\pi} \ll 1. \qquad (1)$$

The combination $\alpha ML/(4\pi)$ in Eq. (1) that quantifies the size of FV Coulomb effects is equivalent to the infinite-volume Coulomb expansion parameter α/v for a pair of hadrons moving back to back with one unit of FV momentum, i.e., $\pm 2\pi/L$. Equation (1) indicates that Coulomb effects can be treated perturbatively in current and future LQCD + QED_L calculations over a wide range of volumes and in particular for systems with $L \sim 1/(\alpha M)$, where the Bohr radius is commensurate with the volume. This scaling differs from that suggested in Ref. [43] by the factor of 4π in the denominator of the $\alpha ML/(4\pi)$.

This manuscript is structured as follows. Section II presents the details and methodology of the LQCD + QED$_L$ calculations that are performed. Section III discusses the construction of NRQED$_L$ for charged multihadron systems and provides the formalism needed to extract hadronic scattering lengths and other parameters from the results of these LQCD + QED$_L$ calculations. Section IV describes the determination of hadronic scattering parameters from LQCD + QED$_L$ and presents results for multimeson and multinucleon systems. Conclusions are presented in Sec. V. Appendix A contains further technical details on the matching between QED$_L$ and NRQED$_L$, and Appendix B contains details on the fitting procedure used to extract energy levels from Euclidean correlation functions computed in LQCD + QED$_L$.

II. LATTICE QCD + QED

Lattice QCD + QED is a nonperturbative approach to QCD + QED that at intermediate stages implements an ultraviolet regulator defined by a lattice spacing a (where $1/a$ is assumed to be much smaller than the QED Landau pole). Calculations are performed in Euclidean spacetime with a cubic spatial volume of extent $L \times L \times L$ and a finite temporal extent T; the quark, gluon, and photon fields satisfy periodic boundary conditions (PBCs) in all spatial directions. Here, the QED$_L$ formalism [26] is used to define charged-particle correlation functions as detailed below, which defines the LQCD + QED$_L$ formalism. The LQCD + QED$_L$ gauge field configurations used were generated by the QCDSF collaboration. The full details of the generation of these ensembles are presented in Refs. [3,4]. For completeness, relevant aspects of the ensemble generation are described below.

A. Lattice action and parameters

The LQCD + QED$_L$ action used in this study is given by

$$S = S_G + S_A + S_F, \tag{2}$$

where S_G is the tree-level Symanzik-improved $SU(3)$ gauge action as defined in Refs. [44–46]. The quark dynamics are encoded by an $\mathcal{O}(a)$-improved stout link nonperturbative clover action:

$$
\begin{aligned}
S_F = \sum_{q \in \{u,d,s\}} \sum_x \Bigg\{ &\frac{1}{2} \sum_\mu [\bar{q}(x)(\gamma_\mu - 1)e^{-ie_q A_\mu(x)} \tilde{U}_\mu(x) q(x+\hat{\mu}) \\
&- \bar{q}(x)(\gamma_\mu + 1)e^{ie_q A_\mu(x-\hat{\mu})} \tilde{U}_\mu^\dagger(x-\hat{\mu}) q(x-\hat{\mu})] \\
&+ \frac{1}{2\kappa_q} \bar{q}(x)q(x) - \frac{1}{4} c_{SW} \sum_{\mu\nu} \bar{q}(x) \sigma_{\mu\nu} F_{\mu\nu} q(x) \Bigg\}, \tag{3}
\end{aligned}
$$

where $\tilde{U}_\mu$ is a single-iterated stout-smeared $SU(3)$ link [47], A_μ is a noncompact $U(1)$ gauge field, and the $U(1)$ quark charges are given by e_q. The field-strength $F_{\mu\nu}$

appearing in the Sheikholeslami-Wohlert or "clover" term [48] involves the unsmeared $SU(3)$ gauge field as in Ref. [49]. The clover coefficient c_{SW} was nonperturbatively determined for pure QCD in Ref. [49]. Electromagnetic gauge fields are not included in the clover term, however with these simulation parameters, the $\mathcal{O}(\alpha a)$ effects are no larger than the residual $\mathcal{O}(a^2)$ effects of pure QCD. The photon action is described by the noncompact form:

$$S_A = \frac{1}{2e^2} \sum_{x, \mu < \nu} (A_\mu(x) + A_\nu(x+\mu) - A_\mu(x+\nu) - A_\nu(x))^2, \tag{4}$$

where e is the $U(1)$ gauge coupling corresponding to $\alpha = e^2/(4\pi)$. Gauge fixing and the treatment of zero modes are discussed in Sec. II B.

The parameters of the lattice action were tuned by identifying a point of approximate $SU(3)$ flavor symmetry, where the average light-quark mass takes its physical value—see Ref. [46] for further discussion. With dynamical QED, this is complicated by the fact that the quark charges explicitly break the $SU(3)$ flavor symmetry. An approximate $SU(3)$ flavor symmetry is then realized by tuning the quark mass parameters such that the connected flavor-neutral pseudoscalar mesons[1] are degenerate. As it is inspired by Dashen's theorem [50], this prescription for separating strong and electromagnetic effects is known as the "Dashen scheme" [4]. This scheme preserves Dashen's theorem, whereby the neutral pseudoscalar mesons are protected from receiving an electromagnetic self-energy correction in the chiral limit. To reach the physical quark masses and charges, the $SU(3)$ flavor symmetric point can then be lowered to the physical value before the symmetry is broken to fix the individual quark masses. In this exploratory work a single set of approximately $SU(3)$ flavor symmetric parameters is used.

The Dashen scheme provides a natural framework for separating QED and QCD effects; at the $SU(3)$ symmetric point, any splittings among pure QCD multiplets are identified as pure QED effects. The explicit breaking of the quark masses from this point then allows one to independently isolate the effects of strong (or quark mass) flavor symmetry breaking and QED effects. The action parameters used in this work correspond to the $SU(3)$ symmetric point and are presented in Table I.

B. Gauge fixing and the $U(1)$ zero mode

The correlation functions of charged particles are not gauge invariant and hence ensemble-averaged quantities

---

[1]Since $\kappa_s = \kappa_d$ and $e_s = e_d$, this theory exhibits exact U-spin symmetry, and therefore the connected $d\bar{d}$ and $s\bar{s}$ correlation functions are identical to the $d\bar{s}$ correlation functions The connected part of the $u\bar{u}$ correction function can be interpreted in a partially quenched theory, see Ref. [4] for further discussion.

TABLE I.   Parameters of the gauge field ensembles and calculations performed in this work. $L^3 \times T$ is the Euclidean spacetime volume, β is the $SU(3)$ gauge coupling as defined in Refs. [44–46], $\beta_E = 1/e^2$ is related to the QED gauge coupling appearing in Eq. (4), κ_q are quark mass parameters for flavors $q \in \{u, d, s\}$ appearing in the quark action, Eq. (3), N_{cfg} is the number of gauge field configurations analyzed in this work, and N_{src} is the average number of quark propagator sources randomly distributed on each gauge field configuration.

$L^3 \times T$	β	β_E	κ_u	κ_d	κ_s	N_{cfg}	N_{src}
$32^3 \times 64$	5.50	0.80	0.124362	0.121713	0.121713	1294	27
$48^3 \times 96$	5.50	0.80	0.124362	0.121713	0.121713	692	9

are only meaningful within some gauge fixing prescription. In this work, Landau gauge is adopted by enforcing the condition

$$\sum_\mu (A_\mu(x) - A_\mu(x - \hat{\mu})) = 0. \tag{5}$$

This condition can be imposed after generation of the gauge fields. However, the Landau gauge condition leaves the four-dimensional zero mode unconstrained. These uniform background fields do not contribute to the gauge action; however they do couple to the fermionic action, Eq. (3). The action remains invariant under discrete shifts of the zero mode in units of $2\pi/L_\mu$. This redundant gauge degree of freedom can be eliminated by mapping the four-dimensional zero modes onto the finite interval $-\pi/L_\mu < \tilde{A}_\mu(k = 0) \le \pi/L_\mu$ [51], where $\tilde{A}_\mu(k)$ is the Fourier transform of $A_\mu(x)$ defined explicitly in Eq. (A3). The leading effect of these zero modes is to induce a charge-dependent twist of the single-hadron momenta. This small energy shift can be corrected in single-hadron states [3]; however this would introduce an unnecessary complication in the analysis of many-body interactions. Instead, this work adopts the QED$_L$ prescription [2,26] of setting the spatial (three-dimensional) zero modes of the gauge potential to zero on every time slice.

With respect to the action used to generate the gauge configurations, the elimination of the three-dimensional zero modes before computing quark propagators is not a gauge symmetry. As a consequence, there is a partial-quenching effect whereby the valence quarks experience a different zero mode to the quarks in the sea. The zero modes cannot affect closed fermion loops, and their only contribution to the determinant will be associated with fermion lines wrapping around the boundary of the lattice. Consequently, this partial-quenching effect is exponentially suppressed in $m_\pi L$ and is negligible in comparison to the power-law FV effects studied in this work.

C. Correlation functions

The particular gauge field ensembles used in this work are described in Table I; along with the parameters used in their generation, the number of configurations and the average number of correlation function source locations

that are used per configuration are also reported. Up and down/strange (equivalent for the masses used here) quark propagators are computed from each of the randomly chosen source locations using three-dimensionally Jacobi smeared sources [52] (100 iterations with $\rho = 0.21$) using a solver tolerance of 10^{-12}. Local and smeared fields are used in the sink interpolating operator to construct smeared-point (SP) and smeared-smeared (SS) correlation functions with the former providing cleaner signals in all cases.

FV energy levels are determined by analyzing two-point correlation functions

$$G_h(t; \mathbf{x}_0) = \left\langle \sum_{\mathbf{x}} \tilde{\chi}_h(\mathbf{x}, t) \chi_h^\dagger(\mathbf{x}_0, 0) \right\rangle, \tag{6}$$

where χ_h ($\tilde{\chi}_h$) is a source (sink) interpolating operator with the quantum numbers of the state being considered and $\mathbf{x}_0$ is the source location. Two-point correlation functions are constructed for $n \in \{1, \ldots, 12\}$ charged pions ($u\bar{d}$) and neutral kaons ($s\bar{d}$) using the techniques developed in Refs. [53–57]. At the sink, each color-singlet meson bilinear is separately projected to zero momentum; for example, for a system of n pions ($h = n\pi^+$),

$$G_{n\pi^+}(t; \mathbf{x}_0)$$
$$= \left\langle \left(\sum_{\mathbf{x}} \bar{u}(\mathbf{x}, t)\gamma_5 d(\mathbf{x}, t) \right)^n (u(\mathbf{x}_0, 0)\gamma_5 \bar{d}(\mathbf{x}_0, 0))^n \right\rangle. \tag{7}$$

The correlation functions for the single proton and neutron make use of standard local interpolating operators $\chi_{p;\alpha} = \epsilon^{ijk}(u^i C\gamma_5 d^j)u_\alpha^k$ and $\chi_{n;\alpha} = \epsilon^{ijk}(d^i C\gamma_5 u^j)d_\alpha^k$ where the parentheses indicate contraction of spin indices. For two-baryon and three-baryon systems, the contraction techniques of Refs. [58,59] are used, again with each baryon separately projected to zero momentum at the sink.

D. Finite-volume energy level determinations

Finite-volume energy levels are extracted from the correlation functions for each system using correlated fits to their time dependence. For the multimeson systems, which factorize easily into color-singlet components, thermal contributions where one component propagates forward in time and another propagates backwards in time are

particularly relevant. The corresponding functional forms that are used to fit these correlation functions are

$$f_{nM}(t, \mathbf{E}, \mathbf{Z}) = \sum_{m=0}^{n} Z_{nM;m} e^{-E_{mM}t} e^{-E_{(n-m)M}(T-t)}$$
$$+ \sum_{e=1}^{N_{\text{states}}-1} Z_{nM}^{(e)} e^{-E_{nM}^{(e)}t}, \tag{8}$$

where $M \in \{\pi^+, \overline{K^0}\}$ labels the type of meson, N_{states} is the total number of nonthermal states included in the fit, E_{nM} is the ground-state energy of the system with the quantum numbers of n mesons of type M, $Z_{nM;m}$ is the overlap factor describing the amplitude of thermal contributions with m forwards propagating mesons and $n - m$ backwards propagating mesons, and nonthermal excited states are also included with energies $E_{nM}^{(e)}$ and overlap factors $Z_{nM}^{(e)}$. In practice, fits with $N_{\text{states}} \in \{1, 2, 3\}$ are used in this work. The vectors $\mathbf{E}$ and $\mathbf{Z}$ indicate the energy and overlap factor parameters to be constrained in the fit. In order to determine the many parameters of these fitting functions, fits are performed sequentially for increasing n, with the energies E_{mM} for $m < n$ used as input for f_{nM} as in Ref. [56]. Thermal effects arising from excited states are not found to be significant.

For baryon systems, statistical noise grows rapidly with the temporal separation between the source and the sink, and the contributions of thermal states are negligible with respect to the statistical uncertainties. For these systems a simpler fit function is used:

$$f_b(t, \mathbf{E}, \mathbf{Z}) = Z_b e^{-E_b t} + \sum_{e=1}^{N_{\text{states}}-1} Z_b^{(e)} e^{-E_b^{(e)}t}, \tag{9}$$

where b labels the type of baryon system and, as for meson systems, the second term corresponds to a sum over the excited states included in the fitting model. This work investigates single-nucleon systems with $b \in \{p, n\}$ as well as two-nucleon systems with $b \in \{nn, np(^1S_0), np(^3S_1), pp\}$ and three-nucleon systems with $b \in \{^3\text{H}, ^3\text{He}\}$.

Best-fit parameters are determined from the minimization of the correlated χ^2 function

$$\chi^2(\mathbf{E}, \mathbf{Z}) = \sum_{t,t'=t_{\min}}^{t_{\max}} (G(t) - f(t, \mathbf{E}, \mathbf{Z}))(\mathcal{S}(\lambda^*)^{-1})_{t,t'}$$
$$\times (G(t') - f(t', \mathbf{E}, \mathbf{Z})) \tag{10}$$

for the appropriate correlation functions, $G(t)$, and fit function, $f \in \{f_{nM}, f_b\}$, $[t_{\min}, t_{\max}]$ is the range of times included in the fit, and $\mathcal{S}(\lambda^*)$ is an estimate of the covariance matrix described below. Finite sample-size fluctuations may make the sample covariance matrix ill-conditioned, and shrinkage techniques [60,61] are used to

obtain a numerical stable inverse covariance matrix. Following the application of shrinkage to LQCD in Ref. [62], the covariance matrix including shrinkage is defined as $\mathcal{S}(\lambda) = (1 - \lambda)\mathcal{C} + \lambda\mathcal{T}$, where $\mathcal{C}$ is the bootstrap covariance matrix and $\mathcal{T} = \text{diagonal}(\mathcal{C})$, and therefore χ^2 minimization with $\mathcal{S}(\lambda)$ interpolates between correlated χ^2 minimization for $\lambda = 0$ and uncorrelated χ^2 minimization for $\lambda = 1$. The optimal shrinkage parameter λ^* appearing in Eq. (10) is chosen to maximize the expected closeness to the true covariance matrix and defined in Eq. (B2), see Appendix B and Ref. [61] for further discussion.

Systematic uncertainties arise from the dependence of the fits on the functional forms and time ranges that are used. To address these, the time ranges are systematically sampled, and fits with and without excited states are attempted, with an information criterion used to select the appropriate number of excited states to include for each fit range choice. A weighted average of the results from all successful fits passing various reliability checks is used to determine the final results. Further details are presented in Appendix B.

For one- and two-nucleon systems, combined fits to the SS and SP correlation functions are performed using common energies but different overlap factors for local and smeared sources. For mesons and three-nucleon systems, combined fits performed in this way are only marginally more precise than fits using SP correlation functions alone, and fits using only SP correlation functions are therefore used in what follows for simplicity.

An effective energy plot that removes thermal effects from backwards propagating states for $n = 1$ systems, as well as constant contributions from thermal effects on $n \geq 2$ correlation functions, is defined as

$$E(t) = \text{ArcCosh}\left(\frac{G(t) - G(t + 4)}{2[G(t + 1) - G(t + 3)]}\right). \tag{11}$$

Note that this effective ground-state energy function differs from the form $\text{ArcCosh}[(G(t + 1) + G(t - 1))/(2G(t))]$ commonly used to remove thermal effects from single-pion correlation functions. The advantage of Eq. (11) is that constant terms present in the spectral representation Eq. (8) for $n \geq 2$ mesons exactly cancel in the correlation function differences appearing in Eq. (11), and in particular Eq. (11) is able to exactly isolate the ground-state energy from a two-meson correlation function including thermal effects of the form $e^{-Et} + e^{-E(T-t)} + \text{const}$. Additional terms with more complicated t dependence arise for $n \geq 3$ meson correlation functions as shown in Eq. (8). Effective energies for $n \geq 3$ systems will therefore include contamination from thermal effects and will only plateau to the true ground-state energy in the region $t \ll T$ where thermal effects can be neglected.

Figures 1–3 show effective energy plots, including correlation function results and fit results for $E(t)$ for each
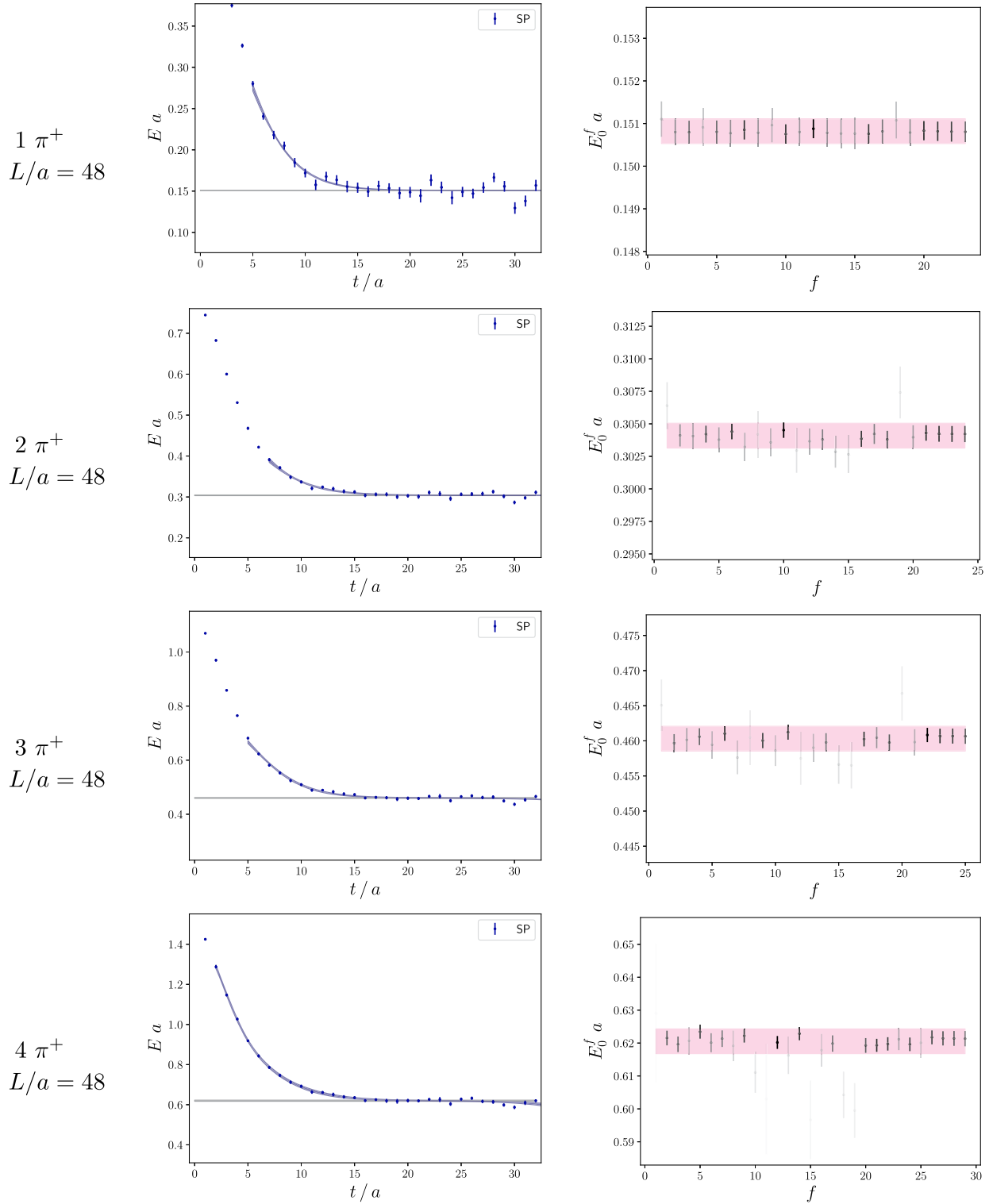
FIG. 1. Fit results for $n \in \{1, \ldots, 4\}\pi^+$ systems with $L/a = 48$. Blue points in the left plots show LQCD + QED$_L$ results for $E(t)$ defined in Eq. (11). Blue bands show 67% confidence intervals from fits to Eq. (8) described in Appendix B. Horizontal light (dark) gray bands show the statistical (total) uncertainty of the fitted ground-state energy. The right plot shows ground-state energy results from each successful fit range with opacity equal to their relative weight in the average determining the total statistical plus systematic uncertainty shown as a pink band.
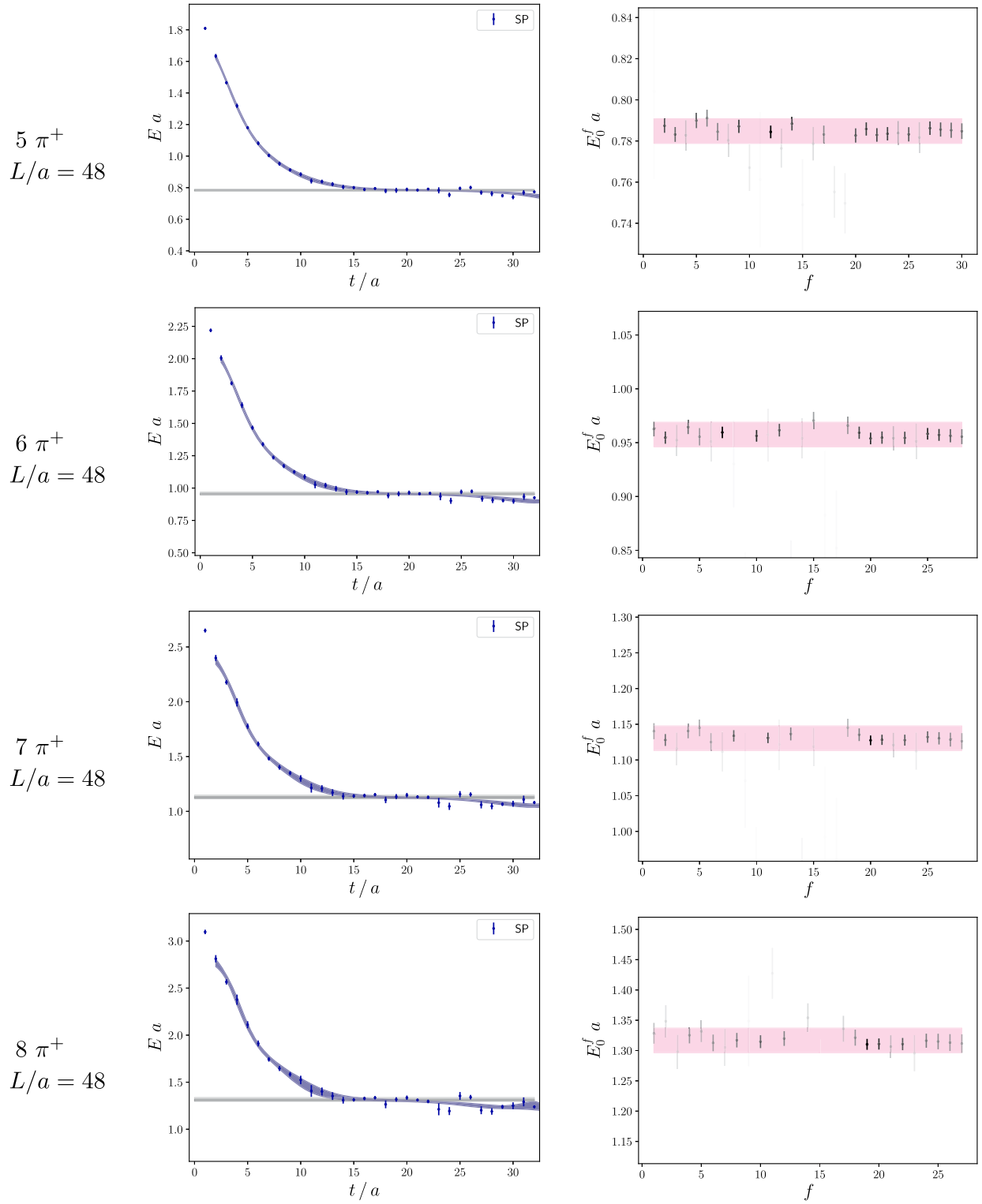
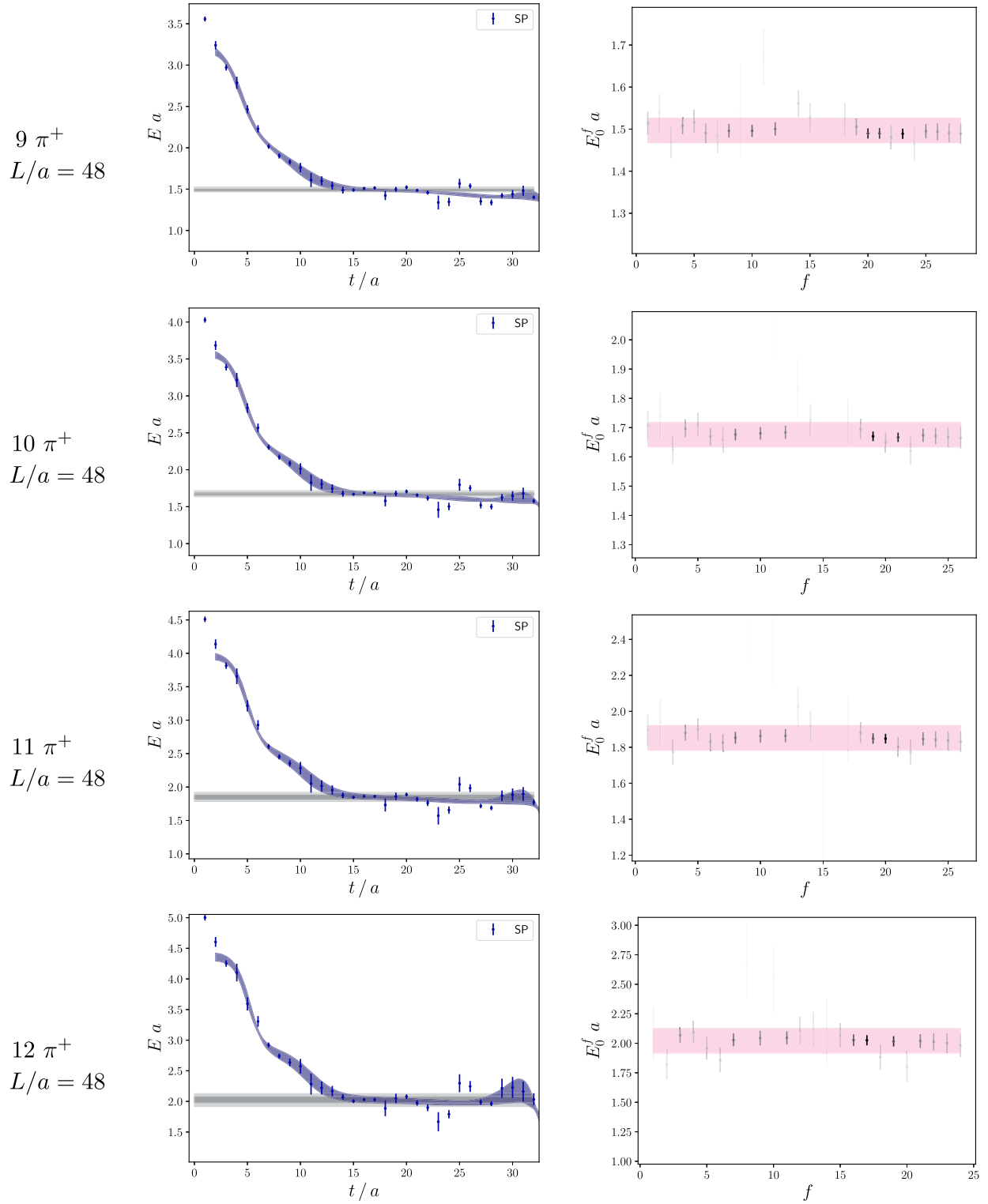FIG. 2. Fit results for systems of $n \in \{5, ..., 8\}\pi^+$ mesons for the $L/a = 48$ lattice volume. The figures are analogous to Fig. 1, see Appendix B for a definition of the fitting procedure employed.

case of $n \in \{1, ..., 12\}\pi^+$ on the $L/a = 48$ lattice volume as well as the ground-state energy results from all successful fit range choices. Analogous results for the $L/a = 32$ volume and for $n = \{1, ..., 12\}\bar{K}^0$ systems on the $L/a \in \{32, 48\}$ volumes are shown in Appendix B. The resulting ground-state energies for $n \in \{1, ..., 12\}$ meson systems on both lattice volumes are shown in Table II.

FIG. 3.   Fit results for systems of $n \in \{9, ..., 12\}\pi^+$ mesons for the $L/a = 48$ lattice volume. The figures are analogous to Fig. 1, see Appendix B for a definition of the fitting procedure employed.

E. Hadron mass results

Single-meson masses computed with the gauge field ensembles used here have already been presented in Ref. [3]; the meson mass results obtained using the fitting produce employed here are shown for completeness in Fig. 4. The $\bar{K}^0$ energy is equal within statistical uncertainties

TABLE II. Ground-state energy results for systems of $n \in \{1, \ldots, 12\}$ neutral $\bar{K}^0$ mesons and charged π^+ mesons with lattice volumes L/a shown. Results are determined by fitting Eq. (8) to the LQCD + QED$_L$ Euclidean correlation functions using the methods described in Appendix B. Dimensionful energy results can be obtained using the lattice spacing $a = 0.068(2)$ fm obtained for this gauge field ensemble in Ref. [3].

	$aE_{n\bar{K}^0}$		$aE_{n\pi^+}$	
n	$L/a = 32$	$L/a = 48$	$L/a = 32$	$L/a = 48$
1	0.13910(45)	0.13921(30)	0.14921(49)	0.15082(29)
2	0.2864(19)	0.2808(10)	0.3058(22)	0.30409(95)
3	0.4431(32)	0.4250(17)	0.4713(37)	0.4603(18)
4	0.6164(86)	0.5730(39)	0.6535(81)	0.6205(37)
5	0.803(14)	0.7245(63)	0.8479(13)	0.7848(60)
6	1.024(23)	0.886(11)	1.076(21)	0.958(11)
7	1.253(32)	1.049(14)	1.316(27)	1.130(17)
8	1.527(63)	1.227(19)	1.591(49)	1.317(20)
9	1.82(11)	1.404(26)	1.865(81)	1.497(29)
10	2.28(17)	1.597(41)	2.17(12)	1.676(42)
11	1.8(1.1)	1.796(58)	2.54(19)	1.852(68)
12	2.7(1.1)	2.002(79)	3.20(20)	2.02(10)

for the $L/a = 48$ and $L/a = 32$ lattice volumes. Volume dependence in $E_{\pi^+}(L)$ and differences in the FV single-particle energies $E_{\pi^+}(L) - E_{\bar{K}^0}(L)$, however, are clearly visible. Because of the quark mass tuning described in Sec. II A, which is designed to remove strong isospin breaking effects, these energy differences are ascribed to QED effects. In order to interpret these QED effects, results for $E_{\pi^+}(L)$ can be compared to the $\mathcal{O}(\alpha, L^{-2})$ prediction of QED$_L$ [2] or equivalently NRQED$_L$ [30],
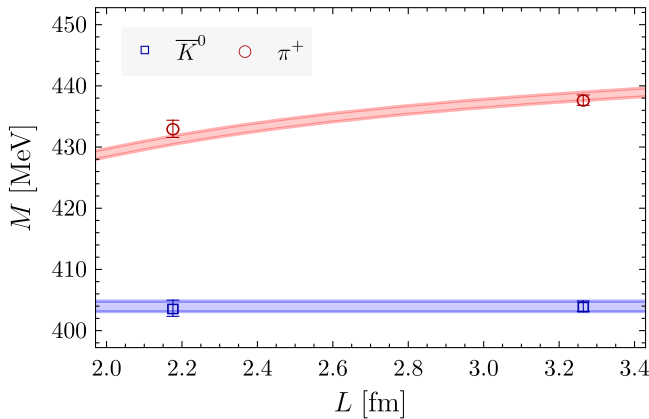

FIG. 4. The blue and red points show the LQCD + QED$_L$ results from Table II for the $\bar{K}^0$ and π^+ single-particle energies for the $L/a \in \{32, 48\}$ volumes. The blue band shows a constant fit to $E_{\bar{K}^0}$ results, and the red band shows a fit to QED$_L$ power-law FV effects at $\mathcal{O}(\alpha/(ML)^2)$ derived in Refs. [2,30] and presented in Eq. (12). The width of the bands corresponds to 67% confidence intervals estimated using bootstrap resampling.

$$E_{\pi^+}(L) = m_\pi + \frac{\alpha}{2L} c_1 \left(1 + \frac{2}{m_\pi L}\right) + \mathcal{O}(\alpha^2, L^{-3}), \quad (12)$$

where $c_1 = -0.266596$ is a geometric constant that does not depend on the system under consideration. Nonlocal effects from zero mode subtraction and charge radius effects introducing a new parameter both arise at next-to-next-to-next-to-leading-order (N^{3}LO) and are neglected here. Fitting the $L/a \in \{32, 48\}$ results to Eq. (12) gives

$$am_{\pi^+} = 0.15419(29), \quad m_{\pi^+} = 449(1)(13) \, \text{MeV}, \quad (13)$$

where the lattice spacing $a = 0.068(2)$ fm is determined in Ref. [3]. The first uncertainty in each term of Eq. (13) includes statistical and systematic fitting uncertainties as detailed in Appendix B, and the second uncertainty in the expression for m_{π^+} arises from the uncertainty in a. A constant fit to the $L/a \in \{32, 48\}$ results for $E_{\bar{K}^0}(L)$ gives

$$am_{\bar{K}^0} = 0.13918(25), \quad m_{\bar{K}^0} = 404(1)(12) \, \text{MeV}. \quad (14)$$

For the values of the quark masses and $\alpha \simeq 0.1$ used in this work, strong isospin breaking effects approximately vanish and the difference between the charged and neutral pseudoscalar meson masses $m_{\pi^+} - m_{\bar{K}^0} = 45(2)$ MeV is attributed entirely to QED effects. It is noteworthy that QED effects account for approximately 10% of the π^+ mass with these parameters.

Results for the proton and neutron ground-state energies are shown in Table III and Fig. 5. Volume dependence of the neutron mass is expected to be exponentially suppressed and is found to be consistent with zero within statistical uncertainties. The proton mass includes power-law FV corrections from QED effects identical to those shown for the π^+ in Eq. (12). These relativistic FV effects are suppressed by $\mathcal{O}((M_p L)^{-1})$ and are therefore suppressed in $E_p(L)$ compared to $E_{\pi^+}(L)$ by $m_{\pi^+}/M_p \ll 1$.

TABLE III. Ground-state energies of systems of $n \in \{1, 2, 3\}$ protons and neutrons determined by fitting Eq. (9) to the LQCD + QED$_L$ Euclidean correlation functions as described in Appendix B.

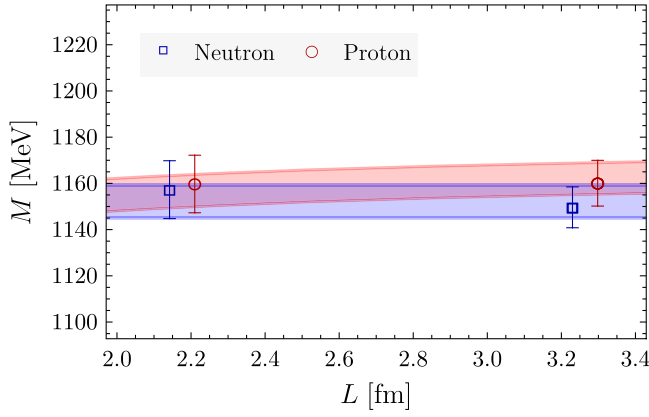|	aE_b	
b	$L/a = 32$	$L/a = 48$
p	0.3997(43)	0.3998(34)
n	0.3988(43)	0.3962(30)
pp	0.816(19)	0.816(16)
$np(^1S_0)$	0.807(20)	0.820(13)
nn	0.806(18)	0.823(12)
$np(^3S_1)$	0.825(16)	0.811(12)
^{3}He	1.294(77)	1.268(42)
^{3}H	1.291(53)	1.294(31)

FIG. 5.　The blue and red points show the $LQCD + QED_L$ results from Table III for the neutron and proton single-particle energies for the $L/a \in \{32, 48\}$ volumes. The blue band shows a fit to a constant for the $L/a \in \{32, 48\}$ results for the neutron, and the red band shows a fit to Eq. (12) (which is valid for arbitrary charged hadrons as well as the pion) for the proton. The band widths correspond to 67% bootstrap confidence intervals. A small horizontal offset is applied symmetrically to proton and neutron results.

The proton energy is found to have mild FV effects consistent with zero and with Eq. (12). Fits to the NLO QED_L prediction for $E_p(L)$ and to a constant for $E_n(L)$ give the results

$$aM_p = 0.4037(23), \quad M_p = 1171(7)(34)\,\text{MeV}, \quad (15)$$

$$aM_n = 0.3971(25), \quad M_n = 1152(7)(34)\,\text{MeV}, \quad (16)$$

where the uncertainties are as defined for the π^+ after Eq. (13). Combining these results gives $M_p - M_n = 20(10)\,\text{MeV}$. This result is approximately ten times larger than the QED contribution to the proton-neutron mass difference at the physical values of the quark masses and α [1–3], which is consistent with the expected linear dependence of the proton-neutron mass difference on α, given the value $\alpha \simeq 0.1$ that is used here.

III. FINITE-VOLUME NONRELATIVISTIC QED

Hadronic EFT results relating FV energy levels to the LECs appearing in EFT Lagrangians are useful for interpreting $LQCD + QED_L$ results, as evidenced by the use of fits to Eq. (12) to describe the volume dependence of single-hadron energies and to extract m_{π^+} and M_p at $L = \infty$. Analogous EFT results for charged multihadron systems are needed to extract hadronic scattering information from $LQCD + QED_L$ results for multihadron FV energy levels, but EFT for charged multihadron systems is complicated by the presence of Coulomb interactions that are nonperturbative for hadron pairs with sufficiently small relative momentum as discussed below. Further

complications arise for nonrelativistic EFTs for QCD + QED_L because of the nonlocality inherent in zero-mode subtraction. However, nonrelativistic EFTs have the advantage that FV energy shifts for systems of arbitrary particle number can be computed more simply than in relativistic EFTs, where the relation between scattering parameters and FV energy levels is not yet known for systems of four or more hadrons. This work therefore pursues the application of non-relativistic EFT to charged multihadron FV systems, and this section develops the formalism necessary for studying multihadron systems in $NRQED_L$ including nonlocal effects arising from zero-mode subtraction.

A. Finite-volume formalism for two charged hadrons

Interactions of two electrically neutral particles with mass M and relative momentum $2\mathbf{p}$ are described at low energies by a scattering phase shift $\delta(p)$, where $p = |\mathbf{p}|$. The phase shift is an analytic function of the center-of-mass energy $E^* = 2\sqrt{p^2 + M^2}$ for energies below both the t-channel cut and the s-channel inelastic particle production threshold. For $p \ll M$, the energy can be described by the nonrelativistic expansion $E^* = 2M + p^2/M + \cdots$, and below the t-channel cut and inelastic threshold the phase shift admits a convergent effective range expansion $p \cot \delta(p) = -\frac{1}{a} + \frac{r}{2}p^2 + \cdots$, where a is the scattering length (not to be confused with the lattice spacing a appearing elsewhere) and r is the effective range. For neutral particles, this expansion is straightforwardly reproduced in terms of pionless EFT [63,64], a theory of hadrons interacting via contact interactions organized in powers of derivatives.

Interactions of electrically charged particles are complicated by the fact that the t-channel cut associated with one-photon exchange and the inelastic photon production threshold start at $p = 0$. This leads to $p = 0$ singularities in contributions to the scattering amplitude from Coulomb ladder diagrams describing iterated one-photon-exchange, shown in Fig. 6. Increasingly higher-loop Coulomb ladder diagrams are suppressed by powers of α, but the $p = 0$ singularity becomes more severe. The loop expansion for Coulomb ladder diagrams corresponds to a perturbative expansion in powers of

$$\eta(p) \equiv \frac{\alpha}{v(p)} = \frac{\alpha M}{2p}, \quad (17)$$

where v is the relative velocity of the two charged particles and $p \ll M$ is assumed throughout this section. For $\eta(p) \gtrsim 1$, QED becomes nonperturbative and Coulomb ladder diagrams must be resummed to all orders in α. As shown in nonrelativistic quantum mechanics by Bethe [65], and in EFT by Kong and Ravndal [66,67], the resummed scattering amplitude is nonanalytic in η and the effective range expansion is modified as
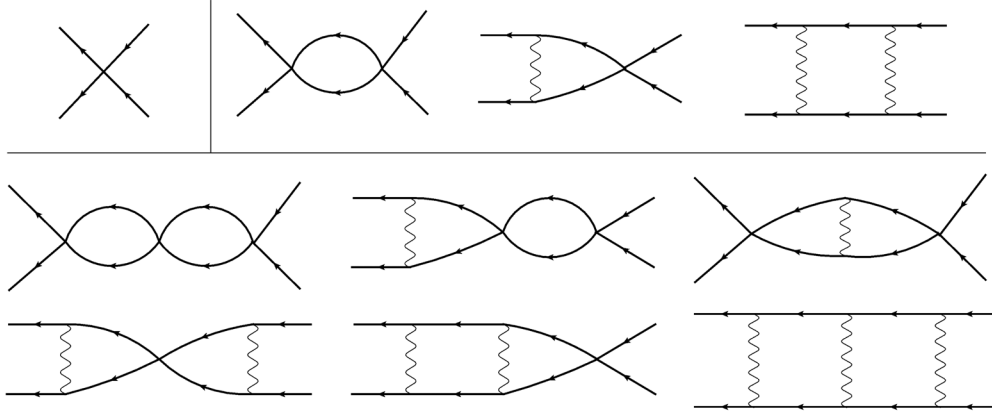
FIG. 6.   The strong-interaction and Coulomb scattering diagrams contributing to the two-body FV energy shift in NRQED$_L$. The top-left section shows the LO diagram. The top-right section shows the NLO diagrams. The bottom section shows the NNLO diagrams in the power counting of Eq. (33). Diagrams that vanish because of zero-mode subtraction, including the tree-level one-photon-exchange diagram, are not shown.

$$\left(\frac{2\pi\eta}{e^{2\pi\eta} - 1}\right) p \cot\delta(p) + 2p\eta[\text{Re}\psi(i\eta) - \ln(\eta)]$$

$$= -\frac{1}{a_C} + \frac{1}{2}r_C p^2 + \ldots, \tag{18}$$

where $\psi(x) = \Gamma'(x)/\Gamma(x)$ is the digamma function, a_C is the Coulomb-corrected scattering length, and r_C is the effective range of the charged particle system. To leading order in α, and at all orders in η and in the four-particle contact interactions as in pionless EFT, the charged particle effective range is unaffected by QED interactions and $r_C = r$ [67]. Conversely, the contact interaction associated with the scattering length must be renormalized to absorb divergences from Coulomb ladder diagrams. In the $\overline{\text{MS}}$ scheme, the running coupling that would be identified with the scattering length in the absence of QED is related to the Coulomb-corrected scattering length by [67]

$$\frac{1}{a^{\overline{\text{MS}}}(\mu)} = \frac{1}{a_C} + \alpha M\left[\ln\left(\frac{\mu\sqrt{\pi}}{\alpha M}\right) + 1 - \frac{3}{2}\gamma_E - \frac{1}{2}\mu r\right], \tag{19}$$

and can be understood as the physical scattering length with Coulomb effects from infrared length scales $>1/\mu$ removed.

The FV two-particle energy spectrum can be related to the scattering phase shift in nonrelativistic quantum mechanics [68] and in quantum field theory [40,41]. In a finite spatial volume of size L^3 with PBCs, the system exhibits reduced spatial symmetries characterized by covariance under the cubic group, and the momentum carried by a free particle is quantized as $\mathbf{p} = 2\pi\mathbf{n}/L$ with $\mathbf{n} \in \mathbb{Z}_3$. In QED$_L$, zero-mode subtraction implies that the momentum carried by a photon propagator is restricted to $p \geq 2\pi/L$. The expansion parameter $\eta(p)$ in Eq. (17) is therefore restricted to

$$\eta(p) \leq \eta_L \equiv \frac{\alpha ML}{4\pi} \tag{20}$$

in QED$_L$ Coulomb ladder diagrams. For sufficiently small volumes, $\eta \leq \eta_L \ll 1$ and Coulomb photon exchange can be treated perturbatively.

The $\mathcal{O}(\alpha)$ quantization condition relating the s-wave scattering amplitude to the two-particle spectrum in the A_1^+ representation of the cubic group in nonrelativistic EFT in the approximation of negligible partial wave mixing was derived in Ref. [43],

$$\left(\frac{2\pi\eta}{e^{2\pi\eta} - 1}\right) p \cot\delta(p) + 2p\eta[\text{Re}\psi(i\eta) - \ln(\eta)]$$

$$= \frac{1}{\pi L}\mathcal{S}^C(p) + \alpha M\left[\ln\left(\frac{4\pi}{\alpha ML}\right) - \gamma_E\right], \tag{21}$$

where $\eta(p)$ is defined in Eq. (17) and

$$\mathcal{S}^C(x) = \mathcal{S}(x) - \frac{\alpha ML}{4\pi^3}\mathcal{S}_2(x) + \frac{\alpha M a_C^2 r_C}{\pi^2 L^2}\mathcal{I}\mathcal{S}(x)^2 + O(\alpha^2), \tag{22a}$$

$$\mathcal{S}(x) = \lim_{\Lambda_n \to \infty} \sum_{\mathbf{n} \in \mathbb{Z}^3}^{|\mathbf{n}| < \Lambda_n} \frac{1}{|\mathbf{n}|^2 - x^2} - 4\pi\Lambda_n, \tag{22b}$$

$$\mathcal{S}_2(x) = \lim_{\Lambda_n \to \infty} \sum_{\mathbf{n} \in \mathbb{Z}^3}^{|\mathbf{n}| < \Lambda_n} \sum_{\mathbf{m} \in \mathbb{Z}^3 \setminus \{\mathbf{n}\}} \frac{1}{|\mathbf{n}|^2 - x^2} \frac{1}{|\mathbf{m}|^2 - x^2} \frac{1}{|\mathbf{n} - \mathbf{m}|^2}$$

$$- 4\pi^4 \ln\Lambda_n, \tag{22c}$$

where $\mathcal{I} \approx -8.9136$ is a geometric constant whose evaluation is detailed in Refs. [40] and sums over integer triplets $\mathbf{n}$ are restricted to $|\mathbf{n}| \leq \Lambda_n$ where Λ_n is a cutoff and the $\Lambda_n \to \infty$ limit should be taken as indicated.

LQCD + QED$_L$ results for the p associated with FV energy levels below three-particle thresholds can be related to charged particle scattering phase shifts by Eq. (21) and used to constrain parametrizations of the phase shift such as Eq. (18). Since Eq. (21) neglects exponentially small FV effects present in small volumes, as well as $(\alpha ML)^n$ effects from Coulomb ladder diagrams with n photon propagators that must be resummed for sufficiently large volumes, Eq. (21) is necessarily valid only for an intermediate range of L. An important goal of this work is to test the range of volumes over which Eq. (21) can be reliably used to extract Coulomb-corrected scattering parameters from LQCD + QED$_L$ results.

B. Charged two-hadron systems in NRQED$_L$

Equation (21) can be perturbatively expanded in powers of a_C/L and other higher-order effective range expansion coefficients. Reference [43] determined this expansion to $\mathcal{O}(\alpha ML)$ and $\mathcal{O}(a_C/L)^3$ under the assumption that $\alpha ML \ll a_C/L \ll 1$. Following Refs. [69,70], the same result can be derived in nonrelativistic quantum mechanics using a Hamiltonian that perturbatively includes the effects of relativity and allows straightforward generalization to many-particle systems. The NRQED$_L$ Lagrangian is given by

$$\mathcal{L} = \psi^\dagger \left(i D_0 - \frac{\mathbf{D}^2}{2M} \right) \psi - \frac{1}{2} \left(\frac{4\pi a}{M} \right) (\psi^\dagger \psi)^2$$
$$- \frac{\eta_3(\mu)}{3!} (\psi^\dagger \psi)^3 + \mathcal{L}_\gamma^\xi + \mathcal{L}_r. \qquad (23)$$

In this expression ψ is a nonrelativistic hadron field, $D_\mu = \partial_\mu + ieQA_\mu$ where Q is the electric charge operator, the gauge-fixed photon Lagrangian $\mathcal{L}_\gamma^\xi$ is given in Eq. (A2), $\eta_3(\mu)$ is a renormalization-scale-dependent coupling associated with short-range three-body interactions, and four- and higher-body interactions are neglected. $\mathcal{L}_r$ includes effective range contributions and relativistic corrections involving two derivatives, and is given by

$$\mathcal{L}_r = \psi^\dagger \left(\frac{\mathbf{D}^4}{8M^3} \right) \psi - \frac{1}{2} \left(\frac{\pi a}{M} \right) \left(ar - \frac{1}{M^2} \right)$$
$$\times (\psi^\dagger \psi)(\psi^\dagger \mathbf{D}^2 \psi + \psi \mathbf{D}^2 \psi^\dagger). \qquad (24)$$

The coefficient of the $(\psi^\dagger \psi)(\psi^\dagger \mathbf{D}^2 \psi + \psi \mathbf{D}^2 \psi^\dagger)$ operator in Eq. (24) can be fixed by demanding that the strong interaction EFT given by replacing D_μ with ∂_μ reproduces Eq. (21) with $\alpha = 0$ when both are expanded perturbatively in powers of L^{-1} to[2] $\mathcal{O}(L^{-6})$. This $\mathcal{O}(L^{-6})$ threshold

expansion of Lüscher's quantization condition is given in Ref. [73] and is verified below to be reproduced by the nonrelativistic EFT defined by Eqs. (23)–(24).[3] Operators in $\mathcal{L}_r$ lead to contributions to the threshold expansion suppressed by ar/L^2 as well as relativistic effects suppressed by $\mathcal{O}((ML)^{-2})$ that will be neglected in the power counting schemes discussed below. Additional relativistic corrections to Eq. (23) arise from photon loops and operators with four and more derivatives, but these give rise to FV effects suppressed by powers of $\mathcal{O}((ML)^{-1})$ that will be neglected as discussed below and detailed in Appendix A.

Introducing Fourier transformed fields

$$\tilde{\psi}_{\mathbf{k}} = \frac{1}{L^{3/2}} \int d^3x \, e^{i\mathbf{k}\cdot\mathbf{x}} \psi(\mathbf{x}), \quad \psi(\mathbf{x}) = \frac{1}{L^{3/2}} \sum_{\mathbf{k}} e^{-i\mathbf{k}\cdot\mathbf{x}} \tilde{\psi}_{\mathbf{k}}, \qquad (25)$$

the FV Hamiltonian for NRQED$_L$ is given by

$$H = \sum_{\mathbf{k}} \tilde{\psi}_{\mathbf{k}}^\dagger \left(\frac{\mathbf{k}^2}{2M} \right) \tilde{\psi}_{\mathbf{k}} + H_\gamma^\xi + H_{\text{int}}, \qquad (26)$$

where H_γ^ξ is the gauge-fixed photon Hamiltonian, whose explicit form will not be used below, and

$$H_{\text{int}} = -\sum_{\mathbf{k}} \tilde{\psi}_{\mathbf{k}}^\dagger \left(\frac{\mathbf{k}^4}{8M^3} \right) \tilde{\psi}_{\mathbf{k}}$$
$$+ \frac{1}{2L^3} \sum_{\mathbf{p}',\mathbf{p},\mathbf{Q}} V(\mathbf{p},\mathbf{p}') \tilde{\psi}_{\mathbf{Q}-\mathbf{p}'}^\dagger \tilde{\psi}_{\mathbf{Q}+\mathbf{p}'}^\dagger \tilde{\psi}_{\mathbf{Q}-\mathbf{p}} \tilde{\psi}_{\mathbf{Q}+\mathbf{p}}$$
$$+ \frac{\eta_3(\mu)}{(3!)L^6} \sum_{\mathbf{Q},\mathbf{p},\mathbf{p}',\mathbf{q},\mathbf{q}'} \tilde{\psi}_{\mathbf{Q}+\mathbf{p}'}^\dagger \tilde{\psi}_{\mathbf{Q}+\mathbf{q}'}^\dagger \tilde{\psi}_{\mathbf{Q}-\mathbf{p}'-\mathbf{q}'}^\dagger \tilde{\psi}_{\mathbf{Q}+\mathbf{p}}$$
$$\times \tilde{\psi}_{\mathbf{Q}+\mathbf{q}} \tilde{\psi}_{\mathbf{Q}-\mathbf{p}-\mathbf{q}}, \qquad (27)$$

where the two-body potential includes strong interaction and Coulomb terms,

$$V(\mathbf{p}',\mathbf{p}) = \frac{4\pi}{M} \left(a + \frac{a}{4} \left(ar - \frac{1}{M^2} \right) (\mathbf{p}^2 + \mathbf{p}'^2) + \dots \right)$$
$$+ \frac{4\pi\alpha}{|\mathbf{p}' - \mathbf{p}|^2} (1 - \delta_{\mathbf{p},\mathbf{p}'}). \qquad (28)$$

Relativistic corrections to the potential, including photon loop effects as well as nonlocal effects of zero-mode removal, can in principle be calculated by carrying out the FV analog of higher-order matching between QED, NRQED, and potential NRQED (pNRQED) [74–76], but

---

[2]The Lagrangian in Eq. (24) can also be obtained by studying the nonrelativistic limit of relativistic scalar field theory as in Refs. [71,72].

[3]References [69,70] include the operators in Eq. (24), but a factor of 2 discrepancy in the coefficient of the last term leads to a difference in the $\mathcal{O}(L^{-6})$ threshold expansion result.

these terms give rise to $\mathcal{O}(ML)^{-1}$ effects that are neglected below.

Specializing to the case of identical bosons, operators are associated with the fields in Eq. (26) and are defined to satisfy commutation relations $[\tilde{\psi}^{\dagger}_{\mathbf{p}'}, \tilde{\psi}_{\mathbf{p}}] = \delta_{\mathbf{p},\mathbf{p}'}$. FV two-particle states defined by

$$|\mathbf{p}_1, \mathbf{p}_2\rangle = \frac{1}{\sqrt{2}} \tilde{\psi}^{\dagger}_{\mathbf{p}_1} \tilde{\psi}^{\dagger}_{\mathbf{p}_2} |0\rangle \qquad (29)$$

satisfy $\langle \mathbf{p}_1, \mathbf{p}_2 | \mathbf{p}_1, \mathbf{p}_2 \rangle = 1$. The ground state of the two-particle system in its center-of-mass frame is $|\mathbf{p}_1 = \mathbf{0}$,

$\mathbf{p}_2 = \mathbf{0}\rangle$. Splitting the Hamiltonian into kinetic energy terms and an interaction term H_{int} that will be treated perturbatively, the ground-state FV energy shift at leading order in Rayleigh-Schrödinger perturbation theory is then given by

$$\Delta E^{\text{LO}} = \langle \mathbf{0}, \mathbf{0} | H_{\text{int}} | \mathbf{0}, \mathbf{0} \rangle = \frac{1}{L^3} V(\mathbf{0}, \mathbf{0}) = \frac{4\pi a}{ML^3}. \qquad (30)$$

Standard perturbation theory techniques can be used to extended this result to higher orders in a/L and α. At next-to-next-to-leading order (NNLO) in H_{int}, the result is given by

$$\Delta E^{\text{NNLO,PC1}} = \frac{4\pi a_C}{ML^3} \left\{ 1 - \left(\frac{a_C}{\pi L}\right) \mathcal{I} + \left(\frac{a_C}{\pi L}\right)^2 [\mathcal{I}^2 - \mathcal{J}] \right\}$$
$$+ \frac{\alpha}{\pi L} \left\{ -\left(\frac{a_C}{\pi L}\right) 2\mathcal{J} + \left(\frac{a_C}{\pi L}\right)^2 \left\{ 2\mathcal{I}\mathcal{J} + \mathcal{R}_{22} - 2\mathcal{K} + 4\pi^4 \left[\ln\left(\frac{4\pi}{\alpha ML}\right) - \gamma_E\right] \right\} \right\}$$
$$- \left(\frac{\alpha ML}{4\pi^3}\right) \mathcal{K} + \left(\frac{a_C}{\pi L}\right) \left(\frac{\alpha ML}{4\pi^3}\right) [2\mathcal{R}_{24} + \mathcal{J}^2 - \mathcal{L}] + \left(\frac{\alpha ML}{4\pi^3}\right)^2 \mathcal{R}_{44} \right\}, \qquad (31)$$

where PC1 is a label for the power counting scheme discussed below and higher-order corrections in $a_C/L \sim r/L$, as well as relativistic effects suppressed by $\mathcal{O}((ML)^{-1})$, have been neglected. All sum-integral differences $\mathcal{I}$, $\mathcal{J}$, $\mathcal{K}$, $\mathcal{L}$, and $\mathcal{R}_{nm}$ which appear in this expression are evaluated[4] in Ref. [43], which includes an evaluation of Eq. (31) in EFT to leading order in αML and to higher order in a/L, except for $\mathcal{R}_{44}$ which is a convergent sum given by $\mathcal{R}_{44} \approx 55.47$.

Equation (31) can be expressed as an expansion in a_C/L and the FV Coulomb parameter η_L defined in Eq. (20),

$$\Delta E^{\text{NNLO,PC1}} = \frac{4\pi a_C}{ML^3} \left\{ 1 - \left(\frac{a_C}{\pi L}\right) \mathcal{I} + \left(\frac{a_C}{\pi L}\right)^2 [\mathcal{I}^2 - \mathcal{J}] \right\}$$
$$+ \frac{4\eta_L}{ML^2} \left\{ -\left(\frac{a_C}{\pi L}\right) 2\mathcal{J} + \left(\frac{a_C}{\pi L}\right)^2 [2\mathcal{I}\mathcal{J} + \mathcal{R}_{22} - 2\mathcal{K} - 4\pi^4[\ln(\eta_L) + \gamma_E]] \right.$$
$$\left. - \left(\frac{\eta_L}{\pi^2}\right) \mathcal{K} + \left(\frac{a_C}{\pi L}\right) \left(\frac{\eta_L}{\pi^2}\right) [2\mathcal{R}_{24} + \mathcal{J}^2 - \mathcal{L}] + \left(\frac{\eta_L}{\pi^2}\right)^2 \mathcal{R}_{44} \right\}. \qquad (32)$$

This resembles a double power series expansion in the parameters η_L and a_C/L, suggesting that the NRQED_L threshold expansion should provide a good approximation of FV energy shifts for

$$\text{PC1:} \quad \eta_L \sim \frac{a_C}{L} \ll 1. \qquad (33)$$

It is noteworthy that $\eta_L \ll 1$ only requires $\alpha ML \ll 4\pi$ and is less restrictive than the condition $\alpha ML \ll 1$ discussed in Ref. [43]. In the matching to the $\text{LQCD} + \text{QED}_L$ simulations discussed below, the power counting $\eta_L \sim a_C/L$ numerically overestimates the size of QED effects,

particularly on the smaller volumes studied, and the alternative power counting[5]

$$\text{PC2:} \quad \eta_L^{1/2} \sim \frac{a_C}{L} \ll 1, \qquad (34)$$

will also be used in fits to $\text{LQCD} + \text{QED}_L$ results. Higher-order results for the threshold expansion for short-range contact interactions without QED [69,70,73,79] can be used to extend Eq. (32) from NNLO in Eq. (33) to N^3LO in Eq. (34),

---

[4]See also Refs. [40,41,43,77,78] for more details on evaluating FV sums.

[5]The description of FV effects on charged hadron masses in QED_L as a dual expansion in α and $(ML)^{-1}$ and the possibility of using alternative power countings in $\text{LQCD} + \text{QED}_L$ calculations depending on the values of these parameters is explored in Ref. [36].

$$\Delta E^{\text{N}^3\text{LO,PC2}} = \frac{4\pi\bar{a}_C}{ML^3}\left\{1 - \left(\frac{\bar{a}_C}{\pi L}\right)\mathcal{I} + \left(\frac{\bar{a}_C}{\pi L}\right)^2[\mathcal{I}^2 - \mathcal{J}]\right.$$
$$- \left(\frac{\bar{a}_C}{\pi L}\right)^3[\mathcal{I}^3 - 3\mathcal{I}\mathcal{J} + \mathcal{K}]\left.\right\}$$
$$+ \frac{4\eta_L}{ML^2}\left\{-\left(\frac{\bar{a}_C}{\pi L}\right)2\mathcal{J} - \left(\frac{\eta_L}{\pi^2}\right)\mathcal{K}\right.$$
$$+ \left(\frac{\bar{a}_C}{\pi L}\right)^2[2\mathcal{I}\mathcal{J} + \mathcal{R}_{22} - 2\mathcal{K}$$
$$- 4\pi^4[\ln(\eta_L) + \gamma_E]]\left.\right\}. \tag{35}$$

The parameter $\bar{a}_C(L)$ is equal to a_C plus a $1/L^3$ suppressed correction arising from the interaction terms in Eq. (24),

$$a_C = \bar{a}_C(L) - \frac{2\pi\bar{a}_C(L)^2}{L^3}\left(\bar{a}_C(L)r - \frac{1}{2M^2}\right), \tag{36}$$

where $(ML)^{-2}$ suppressed effects are shown for completeness and lead to agreement with the $\mathcal{O}(L^{-6})$ strong interaction relativistic threshold expansion of Ref. [73] after taking[6] $\alpha = 0$.

In principle, LQCD + QED$_L$ results for $\pi^+\pi^+$ FV energy shifts on multiple lattice volumes could be used to extract both a_C and r by constraining the $\mathcal{O}(L^{-6})$ difference between $\bar{a}_C$ and a_C. In the LQCD + QED$_L$ calculations discussed below, $(\bar{a}_C(L) - a_C)/a_C$ can be estimated at LO in chiral perturbation theory (χPT) to be 2% and 8% for the $L/a = 48$ and $L/a = 32$ lattice volumes respectively. To see whether $\bar{a}_C - a_C$ can be reliably determined, this estimate must be compared with an estimate of relativistic effects neglected in Eq. (35), which as discussed in Sec. III C modify the dominant QED FV effects by $\mathcal{O}((ML)^{-1})$. For $\pi^+\pi^+$ systems on the $L/a = 48$ lattice volume, the dominant (NLO) QED effect in Eq. (35) amounts to a shift $\bar{a}_C \rightarrow \bar{a}_C - 2\mathcal{J}(\eta_L/\pi^2)\bar{a}_C$, and radiation photon effects can be estimated to lead to a $\mathcal{O}((ML)^{-1})$ suppressed shift in $(\bar{a}_C(L) - a_C)/a_C$ of order $\sim 2\mathcal{J}(\eta_L/\pi^2)/(ML) = \mathcal{J}\alpha/(2\pi^3) \sim 3\%$ for $\alpha \simeq 0.1$. Relativistic effects are therefore comparable to $\bar{a}_C - a_C$ for $\pi^+\pi^+$ systems and prevent the effective range contribution to $\bar{a}_C(L)$ from being disentangled from other FV effects neglected in Eq. (35). Therefore, $\bar{a}_C(L) - a_C$ will be neglected when fitting $\pi^+\pi^+$ LQCD + QED$_L$ results to Eq. (35).

---

[6]The operators in Eq. (24) lead to additional effective range and relativistic corrections to the right-hand side of Eq. (36), namely an additional term of the form $-2a_C^2 r\eta_L\mathcal{I}/(ML^5) - \eta_L^2\mathcal{J}/(4\pi^2 M^3 L^4)$, but these are higher order than the effective range term in Eq. (36) according to the power counting of Eq. (34).

C. Zero-mode effects

The derivation of Eq. (21) in Ref. [43] and the form of the NRQED$_L$ Lagrangian in Eq. (23) assume that charged particle NRQED$_L$ contact interactions in FV are equal to their infinite-volume counterparts up to exponentially suppressed corrections. More recently, however, it has been shown in Refs. [2,30,32,36,38,39] that this assumption is violated in the single-particle sector of NRQED$_L$ because of the inherent nonlocality of zero-mode subtraction. NRQED$_L$ parameters can be obtained by calculating masses, scattering amplitudes, or other observables in both NRQED$_L$ and QED$_L$ and tuning the parameters of the NRQED$_L$ Lagrangian to reproduce QED$_L$ results. In QED$_L$, on shell photon exchange leads to power-law FV effects on charged particle masses suppressed by powers of α and $1/(ML)$ that have been studied in Refs [2,30,32,36,38,39]. The $\mathcal{O}(\alpha/(ML))$ and $\mathcal{O}(\alpha/(ML)^2)$ corrections are independent of the structure of the charged particle and are described by one-loop diagrams in both QED$_L$ and NRQED$_L$. At order $\mathcal{O}(\alpha/(ML)^3)$, structure-dependent effects involving magnetic moments and charge radii arise. Nonlocal effects from zero-mode subtraction also enter at order $\mathcal{O}(\alpha/(ML)^3)$ because zero-mode subtraction leads to power-law FV effects from off shell antiparticle modes in QED$_L$ that are not reproduced by NRQED$_L$ loop diagrams. These effects can be included in NRQED$_L$ by adjusting the Lagrangian to include additional particle-antiparticle interactions [32,39], or more simply by adjusting the coefficients of mass operators in the NRQED$_L$ Lagrangian by factors proportional to $\alpha/(ML)^3$ [38]. For charged scalars, although not for charged fermions, these effects vanish in the charged particle rest frame [38]. This nondecoupling of antiparticle modes is a consequence of the nonlocality of NRQED$_L$, and for EFTs with breakdown scale Λ generically produces $\mathcal{O}(\alpha/(\Lambda L)^3)$ corrections to LECs [38].

Nonlocal effects from zero-mode subtraction could lead to power-law FV effects that modify four-hadron contact interaction couplings proportional to a_C in NRQED$_L$. Considering the $\mathcal{O}(ML)$ enhancement of FV effects associated with Coulomb ladder diagrams, it is necessary to analyze nonlocal effects of zero-mode subtraction on a_C in order to determine whether Eq. (21) is modified within the order of approximation considered. The effects of zero-mode subtraction on a_C can be determined by matching any QED$_L$ and NRQED$_L$ correlation functions sensitive to four-hadron contact interactions. One-particle FV self-energies only receive contributions from four-hadron contact interactions in $\mathcal{O}(\alpha^2)$ diagrams containing closed loops of particle-antiparticle pairs. Two-particle FV Green's functions receive contributions from four-hadron contact interactions at $\mathcal{O}(\alpha^0)$, and it is convenient to calculate nonlocal FV effects on four-hadron contact interactions in NRQED$_L$ by directly matching two-particle FV Green's functions in QED$_L$ and NRQED$_L$. This matching is detailed in Appendix A and summarized below.
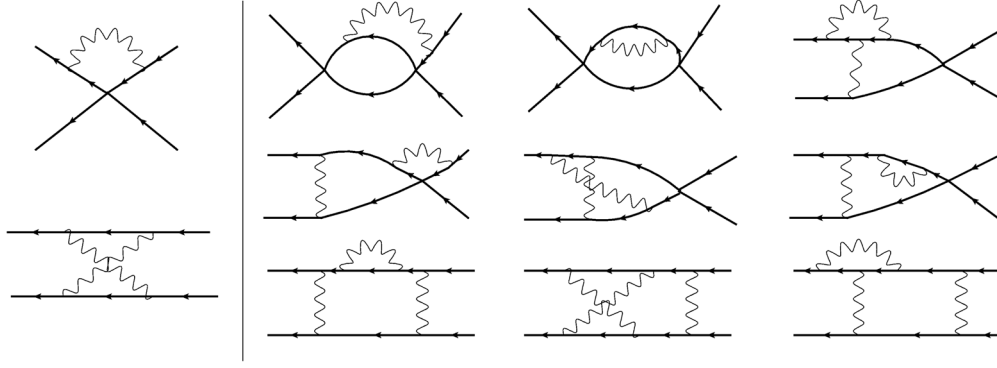
FIG. 7. Radiation photon diagrams making power-suppressed contributions to the two-body FV energy shift in NRQED$_L$. The left and right sections show NLO and NNLO diagrams in the power counting of Eq. (33), respectively, which lead to FV effects suppressed by $\mathcal{O}((ML)^{-1})$.

The $\mathcal{O}(ML)$ enhancement of Coulomb ladder diagrams arises when one intermediate particle propagator is placed on shell and another intermediate particle propagator is nearly on shell with virtuality k^2/M, as compared with virtuality k when a photon propagator is placed on shell. This can be explicitly seen by comparing the integrands of the "box" diagram (rightmost top row in Fig. 6) with the "crossed-box" diagram (leftmost bottom row in Fig. 7). In NRQED$_L$, the box diagram involves the integral

$$
\begin{aligned}
&i \int \frac{dk^0}{2\pi} \left(\frac{1}{k^0 - k^2/2M + i\epsilon} \right) \left(\frac{1}{-k^0 - k^2/2M + i\epsilon} \right) \left(\frac{1}{(k^0)^2 - k^2 + i\epsilon} \right)^2 \\
&= -\left(\frac{M}{k^2} \right) \left(\frac{1}{(k^2/2M)^2 - k^2} \right) + \frac{d}{dk^0} \left[\left(\frac{1}{k^0 - |k|} \right)^2 \left(\frac{1}{k^0 - k^2/2M} \right) \left(\frac{1}{-k^0 - k^2/2M} \right) \right]_{k^0 \to -k} \\
&= \frac{-M}{k^6} [1 + \mathcal{O}(k^2/M^3)] - \frac{3}{4k^5} [1 + \mathcal{O}(k^2/M^2)].
\end{aligned}
\tag{37}
$$

In this expression, the first contribution involving the particle pole places the second particle propagator nearly on shell with kinetic energy $k^2/2M$. The second contribution from the photon double pole gives both particle propagators off shell kinetic energies k. When FV effects are computed, k is replaced by the quantized values $2\pi n/L$ with $n \in \mathbb{Z}_3$, and (after adding all necessary UV counterterms) amplitude suppression by powers of k/M implies suppression of FV effects by the corresponding power of $(ML)^{-1}$. The NRQED$_L$ crossed-box diagram involves the integral

$$
\begin{aligned}
&i \int \frac{dk^0}{2\pi} \left(\frac{1}{k^0 - k^2/2M + i\epsilon} \right)^2 \left(\frac{1}{(k^0)^2 - k^2 + i\epsilon} \right)^2 \\
&= \frac{d}{dk^0} \left[\left(\frac{1}{k^0 - |k|} \right)^2 \left(\frac{1}{k^0 - k^2/2M} \right)^2 \right]_{k^0 \to -k}, \\
&= \frac{3}{4k^5} [1 + \mathcal{O}(k^2/M^2)],
\end{aligned}
\tag{38}
$$

where only the photon pole contributes and leads to particle propagators with off shell kinetic energies k. FV effects associated with the crossed-box diagram are therefore

suppressed by $\mathcal{O}((ML)^{-1})$ compared to the dominant contribution of the box diagram.

The $\mathcal{O}(ML)$ power enhancement of the box diagram is only present in the diagrams involving repeated s-channel Coulomb interactions shown in Fig. 6 but not in the diagrams in Figs. 7 and 8 or other diagrams involving particle-antiparticle pair creation that vanish nonrelativistically.[7] Furthermore, the $\mathcal{O}(ML)$ enhancement only occurs when the intermediate-state charged particles are both nearly on shell. As detailed in Appendix A, power-law FV effects in QED$_L$ that are not reproduced by loop diagrams with the leading order NRQED$_L$ Lagrangian arise from antiparticle poles where intermediate states have a large virtuality of order $2M$. These do not receive the $\mathcal{O}(ML)$ enhancement of particle pole contributions, and zero-mode effects are found to be suppressed by $\mathcal{O}(\alpha/(ML)^3)$. Matching between QED$_L$ and NRQED$_L$ is explicitly performed for charged scalars in Appendix A, and zero-mode effects are found to modify the

---

[7]More details on the power-counting of diagrams involving FV photon exchange are given in Ref. [43] and discussions of analogous power counting arguments for radiation pions are given in Ref. [80].
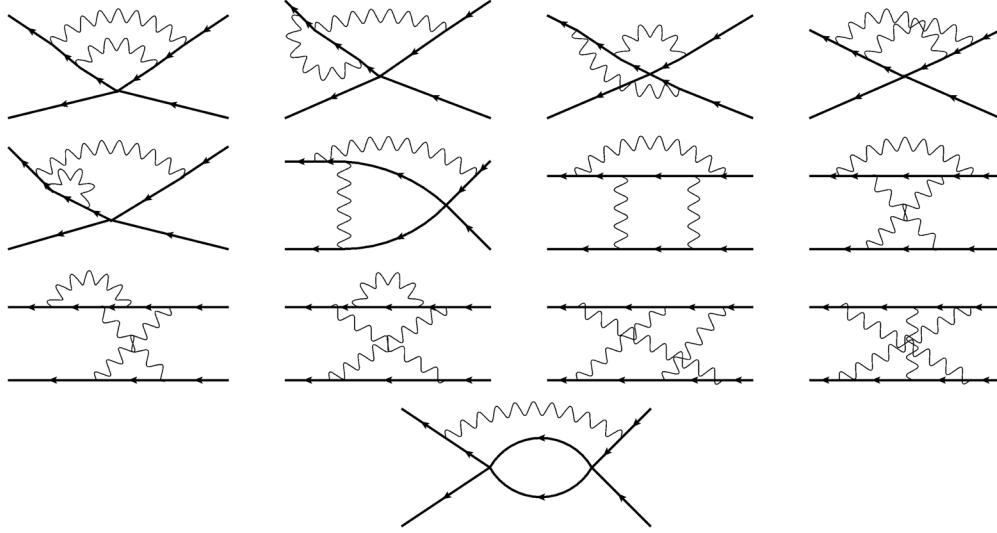
FIG. 8. Radiation photon diagrams, including the jellyfish diagram on the forth row, that appear at NNLO in the power counting of Eq. (33) and lead to FV effects suppressed by $\mathcal{O}((ML)^{-2})$.

four-scalar coupling in NRQED$_L$ at order $\mathcal{O}(\alpha/(ML)^3)$ for boosted systems but not to modify the coupling for scalars at rest at this order. This shows that Eq. (21) is valid for charged scalars in NRQED$_L$ up to $\mathcal{O}(\alpha^2)$ effects and $\mathcal{O}(ML)^{-1}$ relativistic effects. The vanishing of these effects in the center-of-mass frame arises from cancellations due to the specific form of the scalar-photon vertex functions. It is possible that for charged fermions nonlocal effects also arise at $\mathcal{O}(\alpha/(ML)^3)$ in the charged fermion rest frame. The $\mathcal{O}(\alpha/(ML)^3)$ suppression factor is consistent with the physical arguments of Ref. [38] that nonlocal effects arise from interactions between the subtracted zero mode, which can be interpreted as a uniform background charge density that ensures Gauss's law is satisfied for the FV system [26], and high-energy modes that have been integrated out of the EFT, and therefore that FV effects from zero-mode subtraction are suppressed by α times the inverse volume.

D. Charged many-hadron systems in NRQED$_L$

The two-particle energy shifts in Eqs. (32)–(35) can be extended to a threshold expansion for FV effects on systems of n nonrelativistic particles using Rayleigh-Schrödinger perturbation theory. Unit-normalized many-particle states are given by

$$|\mathbf{p}_1,...,\mathbf{p}_n\rangle = \frac{1}{\sqrt{n}}\tilde{\psi}^\dagger_{\mathbf{p}_1}\times...\times\tilde{\psi}^\dagger_{\mathbf{p}_2}|0\rangle, \qquad (39)$$

and the leading order FV energy shift for the ground state of n identical bosons in the center-of-mass frame is given by

$$\langle 0,...0|H_{\text{int}}|0,...0\rangle = \frac{1}{L^3}\binom{n}{2}V(\mathbf{0},\mathbf{0}) + \frac{1}{L^6}\binom{n}{3}\eta_3(\mu). \qquad (40)$$

Working to NNLO in the power counting of Eq. (33), the energy shift of an n-hadron state is equal to $\binom{n}{2}$ times the two-body energy shift of Eq. (32), plus additional contributions from induced three-body and four-body forces shown in Fig. 9. Additional diagrams associated with radiation photon exchange shown in Fig. 10 are suppressed by $\mathcal{O}((ML)^{-1})$. The resulting threshold expansion for the FV energy shift for a system of n like-charged hadrons at rest is given by

$$\Delta E_n^{\text{NNLO,PC1}} = \frac{4\pi a_C}{ML^3}\binom{n}{2}\left\{1 - \left(\frac{a_C}{\pi L}\right)\mathcal{I} + \left(\frac{a_C}{\pi L}\right)^2[\mathcal{I}^2 + (2n-5)\mathcal{J}]\right\} + \frac{4\eta_L}{ML^2}\binom{n}{2}\left\{-\left(\frac{a_C}{\pi L}\right)2\mathcal{J} - \left(\frac{\eta_L}{\pi^2}\right)\mathcal{K} + \left(\frac{\eta_L}{\pi^2}\right)^2\mathcal{R}_{44}\right.$$
$$\left. + \left(\frac{a_C}{\pi L}\right)^2[2\mathcal{I}\mathcal{J} + \mathcal{R}_{22} + (4n-10)\mathcal{K} - 4\pi^4[\ln(\eta_L) + \gamma_E]] + \left(\frac{a_C}{\pi L}\right)\left(\frac{\eta_L}{\pi^2}\right)[2\mathcal{R}_{24} + \mathcal{J}^2 + (2n-5)\mathcal{L}]\right\}, \qquad (41)$$

where omitted terms are quartic or higher in $\eta_L \sim a_C/L$; relativistic effects suppressed by $\mathcal{O}((ML)^{-1})$; or three-body contact interactions where $\eta_3 \sim a_C^4/M$ is assumed so that $\mathcal{O}(L^{-6})$ terms of the strong interaction threshold expansion appear at the same order.
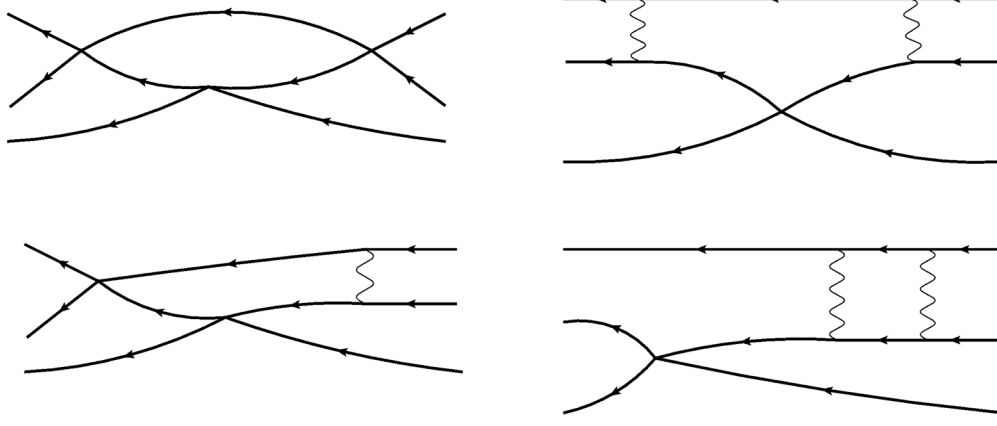
FIG. 9.   The strong-interaction and Coulomb diagrams contributing to three- and higher-body FV energy shifts in NRQED_L at leading order in $(ML)^{-1}$ and NNLO in short-range and Coulomb interactions in the power counting of Eq. (33). Diagrams that vanish because of zero-mode subtraction, partially disconnected diagrams involving pairs of two-body interactions among four and more particles, and diagrams that involve on shell internal propagators and vanish in Rayleigh-Schrödinger perturbation theory, are not shown.
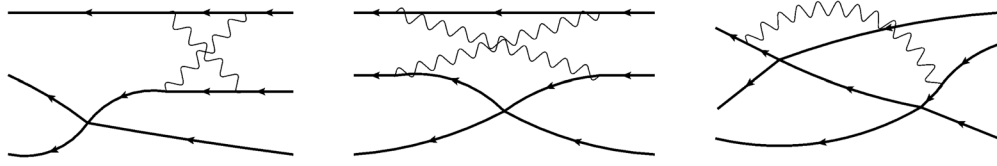
FIG. 10.   Radiation photon diagrams with negligible contributions to three- and higher-body FV energy shifts in NRQED_L at NNLO. The left and center diagrams are suppressed by $\mathcal{O}((ML)^{-1})$, while the right diagram is suppressed by $\mathcal{O}((ML)^{-2})$. As in Fig. 9, partially disconnected diagrams and diagrams that vanish because of zero-mode subtraction or kinematical constraints are not shown.

At N^3LO in the power counting of Eq. (34) there are contributions from short-distance three-body interactions well as the induced few-body interactions discussed above. These introduce a new free parameter $\eta_3(\mu)$ that parametrizes the strength of six-particle operators in the NRQED_L Hamiltonian, Eq. (26). Combining Eq. (41) with the N^3LO results for the QCD threshold expansion from Ref. [69], the N^3LO FV energy shift for a system of n like-charged hadrons in the power counting of Eq. (34) is given by

$$\Delta E_n^{\text{N}^3\text{LO,PC2}} = \frac{4\pi\bar{a}_C}{ML^3}\binom{n}{2}\left\{1-\left(\frac{\bar{a}_C}{\pi L}\right)\mathcal{I}+\left(\frac{\bar{a}_C}{\pi L}\right)^2[\mathcal{I}^2+(2n-5)\mathcal{J}]-\left(\frac{\bar{a}_C}{\pi L}\right)^3[\mathcal{I}^3+(2n-7)\mathcal{I}\mathcal{J}+(5n^2-41n+63)\mathcal{K}]\right\}$$

$$+\frac{4\eta_L}{ML^2}\binom{n}{2}\left\{-\left(\frac{\bar{a}_C}{\pi L}\right)2\mathcal{J}-\left(\frac{\eta_L}{\pi^2}\right)\mathcal{K}+\left(\frac{\bar{a}_C}{\pi L}\right)^2[2\mathcal{I}\mathcal{J}+\mathcal{R}_{22}+(4n-10)\mathcal{K}-4\pi^4[\ln(\eta_L)+\gamma_E]]\right\}$$

$$+\binom{n}{3}\frac{1}{L^6}\left[\eta_3(\mu)+\frac{64\pi\bar{a}_C^4}{M}(3\sqrt{3}-4\pi)\ln(\mu L)-\frac{96\bar{a}_C^4}{\pi^2 M}\mathcal{S}_{\text{MS}}\right]. \tag{42}$$

The nonrelativistic EFT three-body coupling $\eta_3(\mu)$ is renormalization scheme and scale dependent. The scale dependence of $\eta_3(\mu)$ cancels the explicit $\ln(\mu L)$ scale dependence shown in Eq. (42), and the scheme dependence is compensated by scheme dependence in the finite term $\mathcal{S}_{\text{MS}}$. This scale dependence arises from the ambiguity in separating short-distance three-body interactions described by contact operators in NRQED_L from long-distance two-body rescattering effects. In relativistic theories this ambiguity does not arise, and the particle mass plays the role of the scale μ in relativistic descriptions of the $L^{-6}\ln L$ term in the three-body threshold expansion derived for generic relativistic field theories in Ref. [79]. Equating the $\mathcal{O}(L^{-6})$ term in the relativistic threshold expansion of the three-particle threshold amplitude $\mathcal{M}_{3,\text{th}}$ in Ref. [79] with the corresponding $\mathcal{O}(L^{-6})$ nonrelativistic threshold expansion provides a relation between the nonrelativistic coupling $\eta_3(\mu)$ and the scale-independent $\mathcal{M}_{3,\text{th}}$ in the absence of QED,

$$\eta_3(\mu) = -\frac{\mathcal{M}_{3,\text{th}}}{48M^3} + \frac{64\pi a^4}{M}(3\sqrt{3} - 4\pi)\ln\left(\frac{M}{2\pi\mu}\right) + \frac{48a^2\pi^2}{M^3}$$
$$+ \frac{48a^3\pi^2 r}{M} + \frac{12a^4}{\pi^2 M}\mathcal{S}_3 + \frac{768\pi^3 a^3}{M^2}\mathcal{C}_3, \qquad (43)$$

where a is the scattering length for a neutral two-particle system, $\mathcal{C}_3 = -0.05806$ is a FV sum evaluated in Ref. [79], and $\mathcal{S}_3 = 571.398$ is related to $\mathcal{S}_{\text{MS}}$, evaluated in Ref. [70], and to other FV sums from Ref. [79] by $\mathcal{S}_3 = \mathcal{C}_F + \mathcal{C}_4 + \mathcal{C}_5 + 8\mathcal{S}_{\text{MS}}$. QED effects will modify Eq. (43), but these modifications can be neglected at the EFT order considered here. Below, QED effects on three-body forces will be studied by comparing the three-body interaction parameters extracted from $\text{LQCD} + \text{QED}_L$ results for systems of charged and neutral mesons.

IV. RESULTS FOR CHARGED MULTIHADRON SYSTEMS

This section combines the $\text{LQCD} + \text{QED}_L$ results from Sec. II with the NRQED_L results from Sec. III in order to obtain $\text{QCD} + \text{QED}$ predictions for scattering lengths and other hadronic interaction parameters at the values of the quark masses and α used here.

A. Charged meson scattering

The $\text{LQCD} + \text{QED}_L$ results for the FV spectrum results in Table II can be used to constrain the low-energy EFTs for charged and neutral meson interactions. It is convenient to focus on results for the FV energy shifts

$$\Delta E_{nM}(L) = E_{nM}(L) - nE_M(L), \quad M \in \{\bar{K}^0, \pi^+\}. \qquad (44)$$

Results for correlated differences between n-particle ground-state energies and n times the one-particle ground-state energy, as defined in Eq. (44), are more precise than n-particle energies alone. Furthermore, this subtraction non-perturbatively removes single-particle FV effects from n-meson FV energy shift results. For multi-π^+ systems, $\text{LQCD} + \text{QED}_L$ results for these FV energy shifts can be identified with the interaction energy shifts ΔE_n computed perturbatively in NRQED_L in Sec. III. For multi-$\bar{K}^0$ systems, $\text{LQCD} + \text{QED}_L$ results can be identified with the same EFT results after setting α to zero. In the numerical $\text{LQCD} + \text{QED}_L$ calculation, FV energy shifts are computed in a correlated manner using bootstrap resampling as detailed in Appendix B, and the results are shown in Table IV. To access QED-specific effects, the correlated differences of the n charged pions and n neutral kaon FV energy shifts are also computed similarly. The double subtraction suppresses any strong isospin breaking effects arising from the mistuning of the quark masses for different charge quarks. In the numerical $\text{LQCD} + \text{QED}_L$ calculation, correlated differences of FV energy shifts are computed using bootstrap resampling as detailed in Appendix B, and the results are shown in Table V.

TABLE IV. FV energy shift results for systems of $n \in \{2, ..., 12\}$ neutral $\bar{K}^0$ mesons and charged π^+ mesons for lattice volumes with $L/a \in \{32, 48\}$. Results are determined by taking correlated differences between $\text{LQCD} + \text{QED}_L$ ground-state energies during the fit range sampling procedure described in Appendix B.

	$a\Delta E_{n\bar{K}^0}$		$a\Delta E_{n\pi^+}$	
n	$L/a = 32$	$L/a = 48$	$L/a = 32$	$L/a = 48$
2	0.0087(13)	0.00241(62)	0.0080(16)	0.00256(60)
3	0.0268(24)	0.0074(15)	0.0249(28)	0.0080(14)
4	0.0622(66)	0.0163(39)	0.0588(62)	0.0179(38)
5	0.107(11)	0.0286(62)	0.103(12)	0.0313(63)
6	0.177(20)	0.050(11)	0.175(21)	0.053(11)
7	0.267(30)	0.073(14)	0.263(28)	0.075(17)
8	0.399(62)	0.113(20)	0.382(51)	0.111(22)
9	0.53(11)	0.151(28)	0.495(86)	0.141(33)
10	0.75(28)	0.206(42)	0.64(12)	0.167(47)
11	0.5(1.2)	0.265(57)	0.80(25)	0.191(74)
12	0.3(1.8)	0.331(77)	0.76(46)	0.21(12)

Results for the two-particle FV energy shifts $\Delta E_{\pi^+\pi^+}$ and $\Delta E_{\bar{K}^0\bar{K}^0}$ are shown in Fig. 11. Both energy shifts are clearly resolved from zero with relative uncertainties in the range of 15–25% for both volumes, although $\Delta E_{\pi^+\pi^+}$ and $\Delta E_{\bar{K}^0\bar{K}^0}$ on a given volume are indistinguishable. The small magnitude of QED effects on $\Delta E_{\pi^+\pi^+}$ might appear surprising because $\alpha m_\pi L \sim 0.74$ for this volume, but as discussed in Sec. III the appropriate FV analog of the Coulomb expansion parameter is $\eta_L = \alpha m_\pi L/(4\pi) \sim 0.06$ for the $L/a = 48$ volume. Equations (32)–(35) therefore predict that in addition to differences arising from $a_C^{\pi^+\pi^+} \neq a^{\bar{K}^0\bar{K}^0}$, NLO corrections from Coulomb photon exchange modify the LO FV energy shift by $\sim 20\%$ on the $L/a = 48$ lattice volume, which is not expected to be distinguishable given

TABLE V. FV energy shift differences between systems of $n \in \{2, ..., 12\}$ charged π^+ and neutral $\bar{K}^0$ mesons for lattice volumes with $L/a \in \{32, 48\}$. Results are obtained by taking correlated differences between fitted energies as in Table IV.

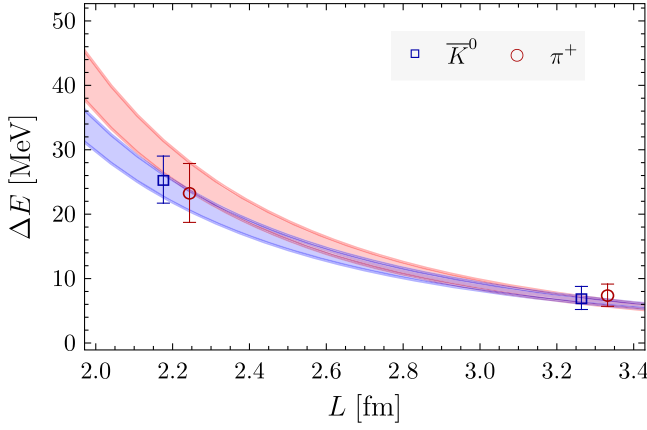|	$a\Delta E_{n\pi^+} - a\Delta E_{n\bar{K}^0}$	
n	$L/a = 32$	$L/a = 48$
2	−0.0006(12)	0.00009(20)
3	−0.0054(29)	−0.00009(86)
4	−0.0070(68)	0.0008(16)
5	−0.013(11)	0.0012(31)
6	−0.022(22)	0.0001(67)
7	−0.040(39)	−0.003(11)
8	−0.065(96)	−0.016(22)
9	−0.10(17)	−0.028(25)
10	−0.14(30)	−0.045(37)
11	0.30(95)	−0.070(59)
12	0.3(1.1)	−0.081(66)

FIG. 11. The blue and red points show the LQCD + QED$_L$ results from Table IV for the $\bar{K}^0\bar{K}^0$ and $\pi^+\pi^+$ FV energy shifts for the $L/a \in \{32, 48\}$ volumes. The red band shows the NRQED$_L$ predictions of Eq. (32) using the best result for $a_C^{\pi^+\pi^+}$ in Eq. (45) obtained by fitting the $L/a \in \{32, 48\}$ results to Eq. (32). The blue band shows the prediction of Eq. (32) with $\alpha = 0$ using the best-fit result for $a^{\bar{K}^0\bar{K}^0}$ in Eq. (45). As in Fig. 4, the widths of the bands correspond to 67% confidence intervals estimated using bootstrap resampling. A small horizontal offset is applied symmetrically to π^+ and $\bar{K}^0$ results.

the statistical uncertainties on $\Delta E_{\pi^+\pi^+}$ and $\Delta E_{\bar{K}^0\bar{K}^0}$. This expectation is consistent with LQCD + QED$_L$ results, as shown in Fig. 11.

The scattering lengths $a_C^{\pi^+\pi^+}$ and $a^{\bar{K}^0\bar{K}^0}$ can be extracted from a combined fit to the results for $\Delta E_{\pi^+\pi^+}$ and $\Delta E_{\bar{K}^0\bar{K}^0}$ shown in Table IV and the results for the precisely determined correlated differences $\Delta E_{\pi^+\pi^+} - \Delta E_{\bar{K}^0\bar{K}^0}$ shown in Table V. Fitting to Eq. (32), as is appropriate for the power counting PC1 of Eq. (33), gives the results,

$$\text{NNLO, PC1}: \quad a^{\bar{K}^0\bar{K}^0} m_{\bar{K}^0} = 0.335(26),$$
$$a_C^{\pi^+\pi^+} m_{\bar{K}^0} = 0.463(41), \quad (45)$$

where the common scale $m_{\bar{K}^0}$ has been included for both $\pi^+\pi^+$ and $\bar{K}^0\bar{K}^0$ to facilitate comparison of $a^{\bar{K}^0\bar{K}^0}$ and $a_C^{\pi^+\pi^+}$. The lowest-order QED effect on $\Delta E_{\pi^+\pi^+}$ from Coulomb photon exchange in Eq. (32) decreases $\Delta E_{\pi^+\pi^+}$ compared to the FV energy shift for neutral particles.[8]

---

[8] Coulomb photon exchange leads to a decrease in the energy of a system of π^+ mesons in QED$_L$ because of zero-mode subtraction. Physically, the energy decrease can be understood as arising from attraction between the charged particle system and the uniform background of opposite charge associated with zero-mode subtraction [26]. Formally, zero-mode subtraction removes the LO one-photon-exchange diagrams associated with repulsion between charged particles. The dominant QED contribution therefore arises at NLO and necessarily lowers the ground-state energy since it appears at second order in perturbation theory.

The scattering length results in Eq. (45) show that this effect from Coulomb photon exchange competes with additional QED effects that lead to $a_C^{\pi^+\pi^+} > a^{\bar{K}^0\bar{K}^0}$. Fitting to Eq. (35), as is appropriate for the power counting PC2 of Eq. (34), gives consistent results,

$$\text{N}^3\text{LO, PC2}: \quad a^{\bar{K}^0\bar{K}^0} m_{\bar{K}^0} = 0.332(27),$$
$$a_C^{\pi^+\pi^+} m_{\bar{K}^0} = 0.465(42), \quad (46)$$

demonstrating that the fit is not overly sensitive to higher-order terms absent in one or the other power counting.

Both Eqs. (32) and (35) neglect relativistic effects from radiation photon exchange leading to $\mathcal{O}((ML)^{-1})$ FV effects. These effects are estimated in Sec. III B to lead to a shift in $a_C^{\pi^+\pi^+}$ of order $\sim3\%$, which is smaller than the 6–9% statistical uncertainty on $a_C^{\pi^+\pi^+}$ in Eqs. (45)–(46) and can be consistently neglected.

B. Charged multinucleon systems

Two-proton states receive QED$_L$ FV effects from Coulomb photon exchange proportional to $\alpha M_p L$ that are enhanced compared with those in the $\pi^+\pi^+$ case discussed above. For both lattice volumes $\alpha M_p L > 1$, and according to the scaling estimates of Ref. [43] Coulomb effects should be nonperturbative. However, $\eta_L^p = \alpha M_p L/(4\pi) \sim 0.15$ for the $L/a = 48$ lattice volume and the NRQED$_L$ results in Sec. III expressed as power series in η_L^p show signs of convergence. Examining the QED$_L$ contributions proportional to a_C^{pp}/L in Eq. (32), the NLO mixed strong-Coulomb contribution is suppressed compared to the LO strong contribution by $(\eta_L^p/\pi^2)2\mathcal{J} \sim 0.51$, while the corresponding NNLO contribution is suppressed compared to the LO contribution by $(\eta_L^p/\pi^2)(2\mathcal{R}_{24} + \mathcal{J}^2 - \mathcal{L}) \sim 0.15$. This suggests that Coulomb effects should be perturbative and subdominant compared to strong-interaction FV effects, which are enhanced by the large size of baryon-baryon scattering lengths [59,81–88]. The quantization condition in Eq. (21), which neglects $\mathcal{O}((\eta_L^p)^2)$ perturbative Coulomb effects and $(ML)^{-1}$ relativistic effects but is nonperturbative in strong interaction effects, is therefore needed to relate the pp FV energy shifts to the infinite volume pp phase shift and determine a_C^{pp}.

The two-nucleon isospin $I = 1$ systems pp, nn, $np(^1S_0)$, as well as the deuteron, are studied on both lattice volumes. Relatively clean signals are seen for each system, and their ground-state energies are determined with total (statistical plus fitting systematic) uncertainties at the 2% level as shown in Table III. FV energy-level shifts are determined from combined analyses of the two-nucleon and single-nucleon correlation functions as described in Appendix B, and fit results for all systems are shown in Appendix B 4. As shown in Table VI and Fig. 12, the statistical precision

TABLE VI. FV energy shift results for systems of $n \in \{1, 2, 3\}$ protons and neutrons determined by fitting Eq. (9) to LQCD + QED_L Euclidean correlation function results as described in Appendix B.

	$a\Delta E_b$	
b	$L/a = 32$	$L/a = 48$
pp	0.008(14)	0.011(11)
$np(^1S_0)$	0.000(17)	0.017(10)
nn	0.002(14)	0.021(10)
$np(^3S_1)$	0.017(13)	0.010(10)
^3He	−0.011(96)	0.038(56)
^3H	0.015(75)	0.080(45)

of this calculation is insufficient to resolve either the proton-proton or neutron-neutron FV energy shift from zero on either volume studied. Resolving nonzero FV shifts of the $\mathcal{O}(10 \text{ MeV})$ size expected for two-nucleon systems without QED at these quark masses at a 95% confidence level for the pp, nn, and np systems on the $L/a = 32$ lattice volume would require statistical ensembles approximately ∼50–100 times larger than the one used here, as estimated by extrapolating the uncertainties of the four different two-nucleon systems considered assuming $1/\sqrt{N}$ scaling of uncertainties. Determination of a_C^{pp} through the QED_L quantization condition of Eq. (21) is therefore left to future work.

The two $I = 1/2$ three-nucleon systems ^3He and ^3H are also investigated, and their ground-state energies are given in Table III. Correlated differences between three-nucleon ground-state energies and the sums of their constituent
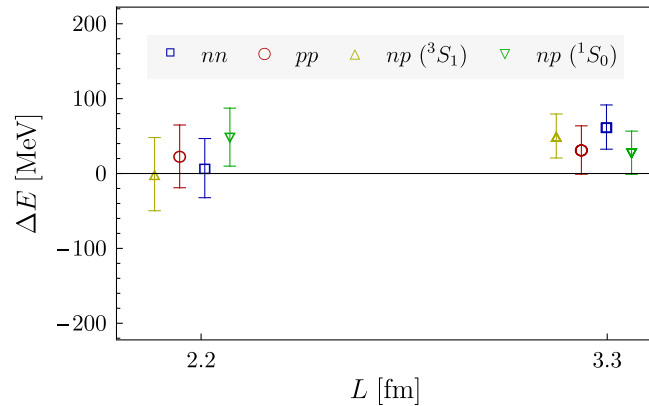
FIG. 12. Points show the LQCD + QED_L results from Table VI for FV energy shifts determined from the correlated differences of two-nucleon and one-nucleon ground-state energies for the neutron-neutron and proton-proton FV energy shifts for the $L/a \in \{32, 48\}$ volumes. A smaller (larger) horizontal offset is applied symmetrically to pp and nn ($np(^1S_0)$ and $np(^3S_1)$) results.

nucleon masses are show in Table VI. As with the two-nucleon systems, fit results are shown in Appendix B 4. The results for ^3He and ^3H are not precise enough to allow FV effects to be reliably determined. Precision in the three-nucleon sector is significantly worse than in the two-nucleon sector, as expected. The absolute size of FV energy shifts is also expected to be larger for three-nucleon systems than two-nucleon systems, and for instance resolving an $\mathcal{O}(50 \text{ MeV})$ FV energy shift at a 95% confidence level for the ^3He and ^3H systems on the $L/a = 32$ lattice volume would require a statistical ensemble approximately ∼100 times larger than the one considered here, based on an extrapolation analogous to that described for the two-nucleon case.

Future high-precision LQCD + QED_L calculations of these multinucleon systems will provide insight into QED effects on nucleon-nucleon and three-nucleon interactions through a determination of the ^3He-^3H binding-energy difference and its decomposition into QED and strong isospin breaking effects from LQCD + QED_L.

C. Systems of many charged mesons

Multipion correlation functions do not suffer from significant exponential signal-to-noise degradation with an increasing particle number and can be used to study QED in the regime where the charge $Z \sim 1/\alpha$. In particular, the correlation functions for systems with $n \leq 12$ π^+ mesons described in Sec. II can be used to study systems with $Z\alpha \leq 1.2$, reaching a charge density of $n/L^3 \sim 1.2 \text{ fm}^{-3}$. The dominant strong interactions and QED effects on many-particle FV energy shifts in Eqs. (41) and (42) both scale with n^2, and both $\Delta E_{n\pi^+}$ and $\Delta E_{n\bar{K}^0}$ can be extracted for larger n with better relative precision than from the $n = 2$ case discussed in Sec. IV A.

Results for $\Delta E_{n\pi^+}$, $\Delta E_{n\bar{K}^0}$, and the correlated differences $(\Delta E_{n\pi^+} - \Delta E_{n\bar{K}^0})$ for $n \in \{2, \dots, 12\}$ are shown in Tables II–V. QED effects leading to nonzero $(\Delta E_{n\pi^+} - \Delta E_{n\bar{K}^0})$ can be resolved to better than 1σ on the $L/a = 32$ lattice volume for $3 \leq n \leq 7$, and on the $L/a = 48$ lattice volume for $n \geq 9$. These 33 FV energy shifts and correlated differences $\Delta E_{n\pi^+}$, $\Delta E_{n\bar{K}^0}$, and $(\Delta E_{n\pi^+} - \Delta E_{n\bar{K}^0})$ can be used to constrain the low-energy interaction parameters $\{a_C^{\pi^+\pi^+}, a^{\bar{K}^0\bar{K}^0}, \eta_3^{\pi^+\pi^+\pi^+}(m_{\bar{K}^0}), \eta_3^{\bar{K}^0\bar{K}^0\bar{K}^0}(m_{\bar{K}^0})\}$ appearing in Eqs. (41) and (42).[9] Fits to the NNLO expression given in Eq. (41) in PC1, which includes $\mathcal{O}(\eta_L^3)$ Coulomb effects but neglects three-body forces, underpredict LQCD + QED_L energy-shift results for $n \gtrsim 8$ meson systems on both lattice volumes and obtain a minimum $\chi^2/N_{\text{dof}} \sim 1.3$. The N³LO expression Eq. (42) in PC2 includes additional

---

[9]The renormalization scale used to evaluate $\eta_3(\mu)$ should be chosen close to the "high" energy scale where NRQED_L is matched to QED_L in order to avoid large logarithms that can worsen EFT convergence. For simplicity, $\mu = m_{\bar{K}^0}$ is used as the renormalization scale for η_3 throughout this work.
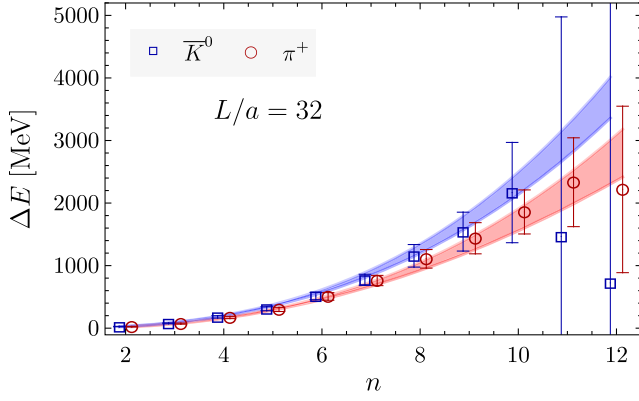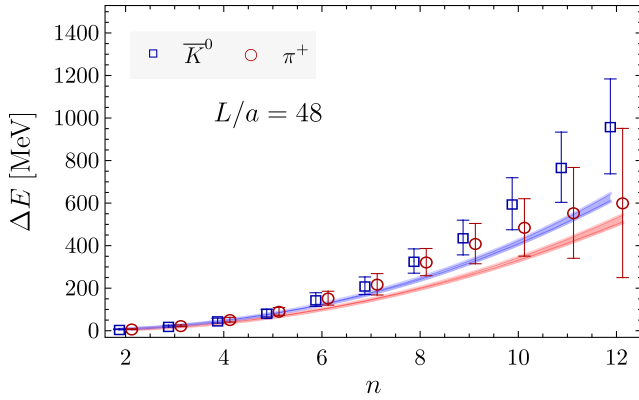
(a) Multi-meson FV energy shifts for the $L/a = 32$ lattice volume.

(b) Multi-meson FV energy shifts for the $L/a = 48$ lattice volume.

FIG. 13. Points show the LQCD + QED$_L$ results from Table IV for the FV energy shifts of multi-$\bar{K}^0$ and multi-π^+ meson systems as a function of meson number n on both lattice volumes. Shaded bands show 67% bootstrap confidence intervals for the predictions of Eq. (42) for the best-fit parameters $\{a_C^{\pi^+\pi^+}, a^{\bar{K}^0\bar{K}^0}, \eta_3^{\pi^+\pi^+\pi^+}(m_{\bar{K}^0}), \eta_3^{\bar{K}^0\bar{K}^0\bar{K}^0}(m_{\bar{K}^0})\}$ obtained from a global fit to the $L/a \in \{32, 48\}$ results for $n \in \{2, ..., 12\}$ mesons in Tables IV–V as described in the main text. A small horizontal offset is applied symmetrically to π^+ and $\bar{K}^0$ results.

(a) π^+ and $\bar{K}^0$ energy shift differences for the $L/a = 32$ lattice volume.
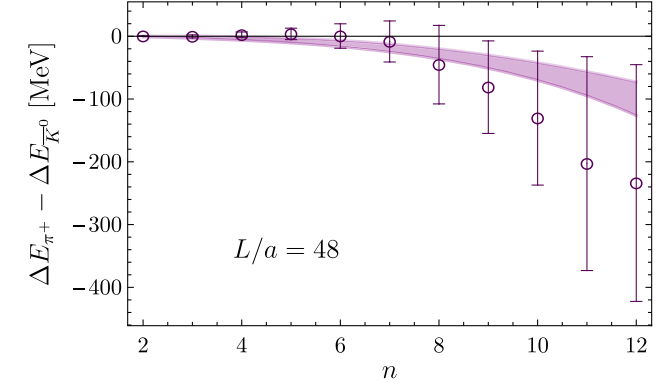
(b) π^+ and $\bar{K}^0$ energy shift differences for the $L/a = 48$ lattice volume.

FIG. 14. Points show the LQCD + QED$_L$ results from Table V for the FV energy-shift differences between multi-π^+ and multi-$\bar{K}^0$ systems as a function of meson number n on both lattice volumes. The shaded band shows the 67% bootstrap confidence interval for the corresponding prediction of Eq. (42) for the best-fit parameters $\{a_C^{\pi^+\pi^+}, a^{\bar{K}^0\bar{K}^0}, \eta_3^{\pi^+\pi^+\pi^+}(m_{\bar{K}^0}), \eta_3^{\bar{K}^0\bar{K}^0\bar{K}^0}(m_{\bar{K}^0})\}$ obtained from a global fit to the $L/a \in \{32, 48\}$ results for $n \in \{2, ..., 12\}$ mesons, given in Tables IV–V, as described in the main text.

free parameters related to three-body forces not present at NNLO. Including three-body force parameters improves the quality of the fit, and Eq. (42) provides a better description of the LQCD+QED$_L$ results with $\chi^2/N_{dof} \sim 0.8$. Fit results using the N^{3}LO expression Eq. (42) and uncertainties computed using bootstrap resampling of the global fitting procedure are compared to LQCD + QED$_L$ results for the π^+ and $\bar{K}^0$ energy shifts in Figs. 13–14. The results for the meson scattering lengths are consistent with, but more precise than, the results obtained from the two-meson FV energy shifts alone,

$$\text{N}^3\text{LO, PC2: } a^{\bar{K}^0\bar{K}^0}m_{\bar{K}^0} = 0.337(19),$$
$$a_C^{\pi^+\pi^+}m_{\bar{K}^0} = 0.464(29). \quad (47)$$

It is noteworthy that results with $Z\alpha \geq 1$ can be fit by the NRQED$_L$ formula given in Eq. (42) without additional modifications to account for relativistic QED effects or additional nonperturbative effects. Some tensions between LQCD + QED$_L$ results and N^{3}LO NRQED$_L$ fits can be observed for $n \gtrsim 8$ meson systems on the $L/a = 48$ lattice volume in Fig. 13; however, since these tensions are more significant for multi-$\bar{K}^0$ than multi-π^+ systems they are unlikely to be signals of nonperturbative QED effects and might result from correlations between LQCD + QED$_L$ results with different n not accounted for in the fitting procedure employed here.

The three-pion scattering amplitude was calculated at LO in χPT in Ref. [89] and is given by $\mathcal{M}_{3,th} = 108m_{\bar{K}^0}^2/f_{\bar{K}^0}^4$ (with conventions for the LO Lagrangian such that

$f_{\pi^+} \sim 130$ MeV).[10] This can be combined with Eq. (43) to provide a χPT prediction for the nonrelativistic $3\bar{K}^0$ contact interaction,

$$\eta_3^{\bar{K}^0\bar{K}^0\bar{K}^0}(\mu) = \frac{3}{4m_{\bar{K}^0}f_{\bar{K}^0}^4} + \frac{m_{\bar{K}^0}}{64\pi^3 f_{\bar{K}^0}^8}(3\sqrt{3} - 4\pi)\ln\left(\frac{m_{\bar{K}^0}}{2\pi\mu}\right)$$
$$+ \frac{3m_{\bar{K}^0}^3}{1024\pi^6 f_{\bar{K}^0}^8}\mathcal{S}_{3,\text{th}} + \frac{3m_{\bar{K}^0}}{2f_{\bar{K}^0}^6}\mathcal{C}_3, \qquad (48)$$

where $\mathcal{S}_{3,\text{th}}$ and $\mathcal{C}_3$ are constants defined below Eq. (43), and to obtain a result entirely in terms of $m_{\bar{K}^0}$ and $f_{\bar{K}^0}$, the LO χPT relations [90]

$$a^{\bar{K}^0\bar{K}^0}m_{\bar{K}^0} = \frac{m_{\bar{K}^0}^2}{8\pi f_{\bar{K}^0}^2}, \qquad r^{\bar{K}^0\bar{K}^0}a^{\bar{K}^0\bar{K}^0}m_{\bar{K}^0}^2 = 3, \qquad (49)$$

have been used. The first of these relations also allows $f_{\bar{K}^0}$ and therefore $\eta_3^{\bar{K}^0\bar{K}^0\bar{K}^0}(\mu)$ to be predicted numerically at LO in χPT for the quark masses used in this work. Inserting the LQCD + QED$_L$ results for $m_{\bar{K}^0}a^{\bar{K}^0\bar{K}^0}$ from Eq. (47) into the first relation in Eq. (49) provides a prediction for $f_{\bar{K}^0}$ at the parameters of this LQCD + QED$_L$ calculation that is valid at LO in χPT:

$$af_{\bar{K}^0} = 0.0476(35), \qquad f_{\bar{K}^0} = 139(10)(4) \text{ MeV}. \qquad (50)$$

Here, the first uncertainty is statistical and the second uncertainty is from the uncertainty in the lattice spacing. In this calculation $m_{\bar{K}^0} = 404(1)(12)$ MeV is between the physical pion and kaon masses; this can be compared with $f_{\pi^+} \sim 130$ MeV and $f_{\bar{K}^0} \sim 156$ MeV extracted from experiments [91]. Inserting this result for $f_{\bar{K}^0}$, and the result for $a^{\bar{K}^0\bar{K}^0}$ in Eq. (47), into Eq. (48) then gives the numerical result $m_{\bar{K}^0}f_{\bar{K}^0}^4\eta_3^{\bar{K}^0\bar{K}^0\bar{K}^0}(m_{\bar{K}^0}) = 0.62(27)$. This result is valid at LO in χPT and can be compared to LQCD + QED$_L$ results for $\eta_3^{\bar{K}^0\bar{K}^0\bar{K}^0}(m_{\bar{K}^0})$ combined with the result for $f_{\bar{K}^0}$ given in Eq. (50).

Dimensionless LQCD + QED$_L$ results for the three-body coupling that are expected to be $\mathcal{O}(1)$ in χPT are given by

---

[10]The $SU(2)$ χPT result for $\mathcal{M}_{3,\text{th}}$ given in Ref. [89] is valid for tree-level $\bar{K}^0\bar{K}^0$ scattering after reinterpreting the $SU(2)$ isospin χPT Lagrangian in terms of the $SU(2)$ V-spin doublet $(\pi^+, \bar{K}^0)$. More formally, the V-spin analog of G-parity acts as $(\pi^+, \bar{K}^0) \rightarrow (K^0, -\pi^0)$ and $(K^0, -\pi^0) \rightarrow (-\pi^+, \bar{K}^0)$ and therefore relates the three-body contact operators of the $SU(2)$ isospin and $SU(2)$ V-spin Lagrangians by $(\pi^+\pi^-)^3 \rightarrow (\bar{K}^0K^0)^3$. For the $SU(3)$ flavor symmetric quark mass scheme used here, V-spin is an exact symmetry of the leading order χPT Lagrangian broken only by QED corrections at higher orders.
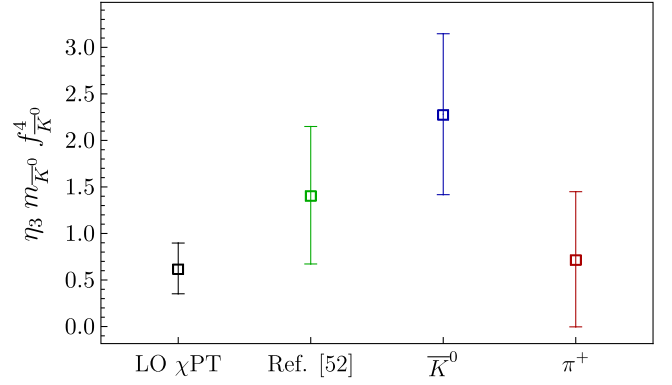

FIG. 15. The blue and red points show the best-fit values and 67% bootstrap confidence intervals for the three-body interaction parameters for neutral $\bar{K}^0\bar{K}^0\bar{K}^0$ and charged $\pi^+\pi^+\pi^+$ systems, respectively, including a common normalization factor of $f_{\bar{K}^0}^4 m_{\bar{K}^0}$ to obtain a dimensionless quantity. The green point shows the LQCD result of Ref. [53], which was obtained in a calculation using a pseudoscalar meson mass of 352 MeV similar to $m_{\bar{K}^0}$ here. The black point shows the LO χPT prediction of Eq. (48) multiplied by the same normalization factor.

$$\eta_3^{\bar{K}^0\bar{K}^0\bar{K}^0}(m_{\bar{K}^0})m_{\bar{K}^0}f_{\bar{K}^0}^4 = 2.28(86),$$
$$\eta_3^{\pi^+\pi^+\pi^+}(m_{\bar{K}^0})m_{\bar{K}^0}f_{\bar{K}^0}^4 = 0.72(73). \qquad (51)$$

The result of this work for $\eta_3^{\bar{K}^0\bar{K}^0\bar{K}^0}(m_{\bar{K}^0})$ is consistent within 1σ uncertainties with the LQCD results of Ref. [53], which were obtained in a calculation using quark masses similar to those used in this work, corresponding to a pion mass of 352 MeV, and extracted η_3 by fitting to the same $\mathcal{O}(L^{-6})$ threshold expansion as used here for multi-$\bar{K}^0$ systems. The corresponding result for $\eta_3^{\pi^+\pi^+\pi^+}(m_{\bar{K}^0})$ is about 2σ smaller than $\eta_3^{\bar{K}^0\bar{K}^0\bar{K}^0}(m_{\bar{K}^0})$, although it is also consistent within 1σ uncertainties with the LQCD results of Ref. [53]. Results for $\eta_3^{\bar{K}^0\bar{K}^0\bar{K}^0}(m_{\bar{K}^0})$ and $\eta_3^{\pi^+\pi^+\pi^+}(m_{\bar{K}^0})$ as well as comparisons to LO χPT and to the LQCD results of Ref. [53] are shown in Fig. 15. Instead of using a global fit to extract the scattering lengths and three-body interaction parameters as above, one can instead fix the scattering lengths to the results obtained using fits to $\Delta E_{\pi^+\pi^+}$, $\Delta E_{\bar{K}^0\bar{K}^0}$ shown in Eq. (46) and extract the three-body interaction parameters from fits to multi-meson results on each volume separately in order to provide an estimate of higher-order FV corrections. Using this alternative fitting procedure to extract the three-body interaction parameters from fits using only the $L/a = 32$ results gives $\eta_3^{\bar{K}^0\bar{K}^0\bar{K}^0}(m_{\bar{K}^0})m_{\bar{K}^0}f_{\bar{K}^0}^4 = 2.1(9)$ and $\eta_3^{\pi^+\pi^+\pi^+}(m_{\bar{K}^0})m_{\bar{K}^0}f_{\bar{K}^0}^4 = 0.5(9)$, while using only the $L/a = 48$ results gives $\eta_3^{\bar{K}^0\bar{K}^0\bar{K}^0}(m_{\bar{K}^0})m_{\bar{K}^0}f_{\bar{K}^0}^4 = 7.0(2.6)$ and $\eta_3^{\pi^+\pi^+\pi^+}(m_{\bar{K}^0})m_{\bar{K}^0}f_{\bar{K}^0}^4 = 5.6(2.4)$, indicating that the $L/a = 32$ results are primarily responsible for

constraining the three-body interaction parameters and suggesting that higher-order FV corrections to the extracted three-body interaction parameters may be significant. Additional consistency checks on the three-body interaction determinations are discussed in Ref. [53], where combinations of n-meson FV energy shifts with fixed n are presented that isolate the three-body interaction parameter in the threshold expansion. In all cases, differences between global fit results and results for three-body interactions parameters obtained with fixed n and fixed L/a in this way are smaller than the corresponding differences between global fits results and the combined fits to all n and fixed L/a discussed above.

Differences between $\eta_3^{\pi^+\pi^+\pi^+}(m_{\bar{K}^0})$ and $\eta_3^{\bar{K}^0\bar{K}^0\bar{K}^0}(m_{\bar{K}^0})$ might arise from QED effects on $\mathcal{M}_{3,\text{th}}$ beyond LO in χPT, or from QED effects on the matching between $\mathcal{M}_{3,\text{th}}^{\pi^+\pi^+\pi^+}$ and $\eta_3^{\pi^+\pi^+\pi^+}(m_{\bar{K}^0})$. Differences between the extracted $\eta_3^{\pi^+\pi^+\pi^+}(m_{\bar{K}^0})$ and $\eta_3^{\bar{K}^0\bar{K}^0\bar{K}^0}(m_{\bar{K}^0})$ might also spuriously arise from the mismodeling of $\mathcal{O}((ML)^{-1})$ relativistic effects estimated in Sec. III B to modify FV energy shifts by $\sim 3\%$. This estimated shift is larger or comparable to the statistical uncertainties on the three-body energy shift for all $n\pi^+$ systems on the $L/a = 48$ volume and $n\pi^+$ systems with $n \lesssim 6$ on the $L/a = 32$ volume. Given these systematic uncertainties in conjunction with the statistical uncertainties on $\eta_3^{\pi^+\pi^+\pi^+}(m_{\bar{K}^0})$ and $\eta_3^{\bar{K}^0\bar{K}^0\bar{K}^0}(m_{\bar{K}^0})$, the results of this work do not provide significant evidence for differences in nonrelativistic short-range three-meson interactions arising from QED effects.

V. CONCLUSIONS

In this work, lattice QCD + QED$_L$ has been used to study systems of up to 12 charged or neutral mesons as well as systems of one, two, and three nucleons. Calculations were performed in two lattice volumes with charge-dependent quark masses tuned such that strong isospin breaking effects are negligible and energy differences between charged and neutral systems are primarily QED effects. While the ground-state energies of two- and three-nucleon systems are determined with few-percent-level precision, QED effects leading to differences between two-nucleon and three-nucleon FV energies are not resolved. Significantly higher precision will be needed in future calculations of QED effects in multinucleon systems. Differences between charged and neutral FV energy shifts are resolved at the level of 1–2σ for systems of 3–12 mesons, demonstrating the presence of QED effects on meson-meson interactions. Analysis of the FV energy levels for multimeson systems using nonrelativistic EFT has allowed the extraction of the $\pi^+\pi^+$ and $\bar{K}^0\bar{K}^0$ scattering lengths as well as the $3\pi^+$ and $3\bar{K}^0$ interaction parameters. Differences between $a_C^{\pi^+\pi^+}$ and $a^{\bar{K}^0\bar{K}^0}$ are clearly resolved, demonstrating that additional QED effects on meson-meson interactions can be resolved beyond the Coulomb photon

exchange explicitly included in the EFT. Differences between the three-body interactions for charged and neutral mesons are not well resolved.

The QED effects on multimeson systems determined from LQCD + QED$_L$ in this work are well described by NRQED$_L$ results that incorporate short-range two- and three-body contact interactions as well as perturbative Coulomb photon exchange. Although Coulomb photon exchange must be treated nonperturbatively in sufficiently large volumes, the expansion parameter describing the size of FV Coulomb effects is found to be $\alpha/v = \alpha M L/(4\pi)$ by examining the convergence pattern of the NRQED$_L$ expansion. This includes a numerically significant factor of $1/(4\pi)$ compared to the parameter $\alpha M L$ discussed in Ref. [43]. For systems with unphysically large α and quark masses such as those studied here, $\alpha M L/(4\pi) \ll 1$ is satisfied for volumes satisfying $L \ll 20$ fm for nucleons ($L \ll 50$ fm for pions), and Coulomb corrections to the LO strong interaction FV energy shift appear perturbative for $L \lesssim 6$ fm for nucleons ($L \lesssim 15$ fm for pions). For calculations with physical α and quark masses, FV Coulomb effects are reduced by a factor of 20 for nucleons (40 for pions) and are expected to be perturbative for all practically accessible lattice volumes. The EFT analysis of this work also demonstrates that NRQED$_L$ results for FV energy shifts are unaffected by the complications of photon zero-mode subtraction up to effects suppressed by $\mathcal{O}((ML)^{-3})$ that are consistently neglected along with other relativistic effects. Future LQCD + QED$_L$ calculations, especially those using lighter quark masses and/or smaller values of the QED fine structure constant, can therefore be interpreted using hadronic EFTs with perturbative Coulomb effects with a similar procedure to the one undertaken here. Such calculations will give insight into the quark mass dependence of QED effects on meson-meson interactions, and, combined with higher-precision calculations of multinucleon FV energy levels, will permit first principles predictions of QED effects on nucleon-nucleon interactions and QED effects in light nuclei.

ACKNOWLEDGMENTS

APPENDIX A: MATCHING NRQED$_L$ AND QED$_L$

Neglecting relativistic effects suppressed by M^{-1} (including nonlocal effects from zero-mode subtraction discussed in Refs. [2,30,32,36,38,39]), the NRQED$_L$ Lagrangian is identical for bosons and fermions. For a particle with charge $Q = 1$, it is given by

$$\mathcal{L}^{\text{NRQED}_L} = \psi^\dagger \left(iD_0 - \frac{D_i D^i}{2M} \right) \psi - \frac{2\pi a}{M} (\psi^\dagger \psi)^2 + \mathcal{L}_\gamma^\xi,$$

$$= \psi^\dagger \left(i\partial_0 - \frac{\partial_i \partial^i}{2M} \right) \psi - eA_0(\psi^\dagger \psi)$$

$$- \frac{2\pi a}{M} (\psi^\dagger \psi)^2 + \mathcal{L}_\gamma^\xi, \tag{A1}$$

where in this section we work in Minkowski spacetime with $(-+++)$ signature, $A_\mu = A_\mu^\dagger$ is the photon field, $F_{\mu\nu} = \partial_\mu A_\nu - \partial_\nu A_\mu$ is the field strength tensor, $D_\mu = \partial_\mu + iA_\mu$, and in generic R_ξ gauge the photon Lagrangian is

$$\mathcal{L}_\gamma^\xi = -\frac{1}{4} F_{\mu\nu} F^{\mu\nu} + \frac{1}{2\xi} (\partial_\mu A^\mu)^2. \tag{A2}$$

Results for the Landau gauge QCD + QED$_L$ calculations performed in the main text are obtained by setting $\xi = 0$. In what follows, a finite spatial volume of extent L^3 with PBCs is considered. Zero mode subtraction can be implemented in NRQED$_L$ by defining the FV photon field as a Fourier transform of the zero-mode subtracted momentum-space field,

$$A_\mu(x) = \int \frac{dp^0}{2\pi} \frac{1}{L^3} \sum_{\mathbf{n} \in \mathbb{Z}^3 \setminus \{\mathbf{0}\}} e^{-ip^0 x^0 + \frac{2\pi i}{L}\mathbf{n}\cdot\mathbf{x}} \tilde{A}_\mu(p^0, \mathbf{n}),$$

$$\tilde{A}_\mu(p^0, \mathbf{n}) = \int d^4x\, e^{ip^0 x^0 - \frac{2\pi i}{L}\mathbf{n}\cdot\mathbf{x}} A_\mu(x), \tag{A3}$$

where $\mathbf{n} \in \mathbb{Z}^3 \setminus \{\mathbf{0}\}$ excludes the photon zero mode. Zero-mode subtraction can be defined at the path integral level as a constraint on the photon field [38], but for perturbative matching with QED$_L$ Eqs. (A1)–(A3) define NRQED$_L$.

The NRQED$_L$ massive particle propagator G^{NRQED_L} is given by

$$G^{\text{NRQED}_L}(p^0, \mathbf{n}) = \int d^4x\, e^{ip^0 x^0 - \frac{2\pi i}{L}\mathbf{n}\cdot\mathbf{x}} \langle \psi(x)\psi^\dagger(0) \rangle$$

$$= \frac{i}{p^0 - \frac{1}{2M}\left(\frac{2\pi\mathbf{n}}{L}\right)^2 + i\epsilon}. \tag{A4}$$

The photon propagator is given by

$$G_{\mu\nu}^{\gamma_L}(p^0, \mathbf{n}) = \int dx^0 \sum_{\mathbf{x}} e^{ip^0 x^0 - \frac{2\pi i}{L}\mathbf{p}\cdot\mathbf{x}} \langle A_\mu(x)A_\nu(0) \rangle$$

$$= \frac{i[g_{\mu\nu} - (1-\xi)\frac{p_\mu p_\nu}{p^2}]}{(p^0)^2 - \left(\frac{2\pi\mathbf{n}}{L}\right)^2 + i\epsilon}. \tag{A5}$$

Introducing Fourier transformed fields,

$$\tilde{\psi}(p^0, \mathbf{n}) = \int d^4x\, e^{ip^0 x^0 - \frac{2\pi i}{L}\mathbf{n}\cdot\mathbf{x}} \psi(x),$$

$$\psi(x) = \int \frac{dp^0}{2\pi} \frac{1}{L^3} \sum_{\mathbf{n} \in \mathbb{Z}^3} e^{-ip^0 x^0 + \frac{2\pi i}{L}\mathbf{n}\cdot\mathbf{x}} \tilde{\psi}(p^0, \mathbf{n}). \tag{A6}$$

Matching between QED$_L$ and NRQED$_L$ is performed for four-point correlation functions describing (off shell) particles with energy M and three-momentum $\mathbf{p} \equiv \frac{2\pi}{L}\mathbf{r}$ with $\mathbf{r} \in \mathbb{Z}_3$,

$$\mathcal{M}^{\text{NRQED}_L} = G^{\text{NRQED}_L}(0, \mathbf{r})^{-4} \langle \tilde{\psi}(0, \mathbf{r})^2 \tilde{\psi}(0, \mathbf{r})^{\dagger 2} \rangle. \tag{A7}$$

At tree level this correlation function is given by

$$\mathcal{M}_{\text{LO}}^{\text{NRQED}_L} = -\frac{8\pi a}{M}. \tag{A8}$$

The choice $\mathbf{r} \neq 0$, which does not affect the tree-level correlation function, is made in order to regulate IR

divergences in the one-loop correlation function. Although one-photon-exchange contributions lead to an IR divergence (regulated for instance by considering nonzero momentum transfer) in the NRQED analog of Eq. (A8), one-photon-exchange contributions to the NRQED_L amplitude in Eq. (A7) vanish because of zero-mode subtraction.

Matching is performed by expanding $\mathcal{M}^{\text{NRQED}_L}$ and its QED_L analog $\mathcal{M}^{\text{QED}_L}$ perturbatively in the small parameters α, $1/(ML)$, and a/L and defining higher-order terms in the NRQED_L Lagrangian so that QED_L and NRQED_L agree order by order in this expansion. Matching will be performed to leading order in $1/(ML)$ and third order in $\eta_L = \alpha ML/(4\pi)$ and a/L. This corresponds to NNLO in the power counting of Eq. (33) and is equivalent to the non-relativistic limit with up to two-loop contact interactions and Coulomb photon exchange. This matching is also sufficient for N³LO in the power counting of Eq. (34), which decreases the relative importance of Coulomb photon exchange and only requires one-loop Coulomb photon exchange effects.

This LO NRQED_L amplitude in Eq. (A8) can be straightforwardly matched to its QED_L analog. The scalar QED_L Lagrangian is

$$
\begin{aligned}
\mathcal{L}^{\text{QED}_L} &= -(D_\mu\varphi)^\dagger D^\mu\varphi - M^2\varphi^\dagger\varphi - 8\pi aM(\varphi^\dagger\varphi)^2 + \mathcal{L}_\gamma^\xi, \\
&= -(\partial_\mu\varphi)^\dagger\partial^\mu\varphi - M^2\varphi^\dagger\varphi + ieA^\mu(\varphi^\dagger\partial_\mu\varphi - (\partial_\mu\varphi)^\dagger\varphi) \\
&\quad - e^2 A_\mu A^\mu \varphi^\dagger\varphi - 8\pi aM(\varphi^\dagger\varphi)^2 + \mathcal{L}_\gamma^\xi,
\end{aligned}
\tag{A9}
$$

where $\mathcal{L}_\gamma^\xi$ is defined in Eq. (A2). The fields appearing in the QED_L and NRQED_L Lagrangians are related by

$$
\psi(x) = \sqrt{2M}e^{iMt}\varphi(x).
\tag{A10}
$$

The scalar QED_L particle propagator is

$$
\begin{aligned}
G^{\text{QED}_L}(p^0, \mathbf{n}) &= \int dx^0 \sum_{\mathbf{x}} e^{ip^\mu x_\mu}\langle\varphi(x)\varphi^\dagger(0)\rangle \\
&= \frac{i}{(p^0)^2 - (\frac{2\pi\mathbf{n}}{L})^2 - M^2 + i\epsilon}.
\end{aligned}
\tag{A11}
$$

The QED_L photon propagator is identical to the NRQED_L propagator Eq. (A5). Introducing Fourier transformed fields $\tilde{\varphi}$ as in Eq. (A6), the FV two-particle amplitude in QED_L normalized identically to the NRQED_L amplitude is given by

$$
\begin{aligned}
\mathcal{M}_{\text{LO}}^{\text{QED}_L} &= \frac{1}{4M^2} G^{\text{QED}_L}(M, \mathbf{r})^{-4}\langle\tilde{\varphi}(M, \mathbf{r})^2\tilde{\varphi}(M, \mathbf{r})^{\dagger 2}\rangle, \\
&= -\frac{8\pi a}{M},
\end{aligned}
\tag{A12}
$$

in agreement with Eq. (A8). This demonstrates that the four-fermion contact interactions in Eqs. (A1) and (A9) are normalized consistently at tree level.

Corrections to the LO amplitude arise from one-loop diagrams shown in Figs. 6–8. The one-loop diagrams shown in Fig. 6 involve similar sums/integrals over loop momenta and differ only in the number of photon propagators n_γ and contact interactions present. The contribution to the amplitude from each diagram is denoted $\mathcal{M}_{\text{NLO}}^{\text{NRQED}_L}(n_\gamma)$ where $n_\gamma \in \{0, 1, 2\}$ labels the numbers of photon propagators present,

$$
\begin{aligned}
\mathcal{M}_{\text{NLO}}^{\text{NRQED}_L}(n_\gamma) &= \frac{i16\pi^2 a^2}{M^2 L^3}\left(\frac{2\alpha M}{a}\right)^{n_\gamma}\sum_{\mathbf{n}}^{(\prime)}\int\frac{dk^0}{2\pi}\left(\frac{1}{k^0 - \frac{2\pi^2(\mathbf{n}-\mathbf{r})^2}{ML^2} + i\epsilon}\right)\left(\frac{1}{k^0 + \frac{2\pi^2(\mathbf{n}+\mathbf{r})^2}{ML^2} - i\epsilon}\right)\left(\frac{1 - (1-\xi)\frac{(k^0)^2}{(k^0)^2 - \frac{4\pi^2\mathbf{n}^2}{L^2} + i\epsilon}}{(k^0)^2 - \frac{4\pi^2\mathbf{n}^2}{L^2} + i\epsilon}\right)^{n_\gamma}, \\
&= -\frac{16\pi^2 a^2}{M^2 L^3}\left(\frac{\alpha M}{a}\right)^{n_\gamma}\sum_{\mathbf{n}}^{(\prime)}\left[\text{Res}\left(-\frac{2\pi^2(\mathbf{n}-\mathbf{r})^2}{ML^2} + i\epsilon\right) + \text{Res}\left(-\frac{2\pi|\mathbf{n}|}{L} + i\epsilon\right)\right],
\end{aligned}
\tag{A13}
$$

where $\text{Res}(x)$ indicates the residue of the integrand in the first line at the pole x and $\sum_{\mathbf{n}}^{(\prime)}$ corresponds to $\sum_{\mathbf{n}\in\mathbb{Z}^3}$ for $n_\gamma = 0$ and to $\sum_{\mathbf{n}\in\mathbb{Z}^3\setminus\{\mathbf{0}\}}$ for $n_\gamma \geq 1$. After taking the $\epsilon \to 0$ limit, the residue at the particle pole $2\pi^2(\mathbf{n} + \mathbf{r})^2/(ML^2)$ is given by

$$
\begin{aligned}
\text{Res}\left(-\frac{2\pi^2(\mathbf{n}-\mathbf{r})^2}{ML^2}\right) &= -\frac{ML^2}{4\pi^2(\mathbf{n}^2 + \mathbf{p}^2)}\left[\frac{1}{\frac{4\pi^4(\mathbf{n}-\mathbf{r})^4}{M^2 L^4} - \frac{4\pi^2\mathbf{n}^2}{L^2}} - \frac{(1-\xi)\frac{4\pi^4(\mathbf{n}-\mathbf{r})^4}{M^2 L^4}}{\left(\frac{4\pi^4(\mathbf{n}-\mathbf{r})^4}{M^2 L^4} - \frac{4\pi^2\mathbf{n}^2}{L^2}\right)^2}\right]^{n_\gamma}, \\
&= -\frac{ML^2}{4\pi^2}\left(-\frac{L^2}{4\pi^2}\right)^{n_\gamma}\frac{1}{(\mathbf{n}^2 + \mathbf{r}^2)\mathbf{n}^{2n_\gamma}}[1 + \mathcal{O}((ML)^{-2})],
\end{aligned}
\tag{A14}
$$

where the last line includes an expansion in powers of $(ML)^{-1}$. This expansion is legitimate provided that the sum over $\mathbf{n}$ converges, which holds for $n_\gamma \geq 1$. For $n_\gamma = 0$ there is a linear UV divergence that can be removed by adding a UV counterterm,

$$
\sum_{\mathbf{n}\in\mathbb{Z}^3}\frac{1}{\mathbf{n}^2 + \mathbf{r}^2} \to \lim_{\Lambda\to\infty}\sum_{\mathbf{n}\in\mathbb{Z}^3}^{|\mathbf{n}|<\Lambda}\frac{1}{\mathbf{n}^2 + \mathbf{r}^2} - 4\pi\Lambda,
\tag{A15}
$$

and after making the replacement of Eq. (A15) the $1/(ML)$ expansion can be performed in Eq. (A14). The photon pole residue at $-2\pi|\mathbf{n}|/L$ involves energy denominators of order $1/L$ and is suppressed by $\mathcal{O}((ML)^{-1})$ compared to the particle-pole contributions in Eq. (A14) where particle propagator energy denominators are of order M/L^2. For all diagrams in Figs. 7–8, particle poles only appear in either the upper or lower half of the complex plane and only photon poles contribute. After performing the energy integrals these diagrams can be straightforwardly verified to be suppressed by $\mathcal{O}((ML)^{-1})$ or $\mathcal{O}((ML)^{-2})$ compared to Eq. (A16). The full NLO amplitude in NRQED$_L$ is therefore a sum of the amplitudes $\mathcal{M}_{\text{NLO}}^{\text{NRQED}_L}(n_\gamma)$ associated with the diagrams in Fig. 6 obtained by substituting Eq. (A14) into Eq. (A13),

$$\mathcal{M}_{\text{NLO}}^{\text{NRQED}_L}(n_\gamma) = \frac{4\pi a}{M}\left(-\frac{\alpha ML}{2\pi^3}\right)^{n_\gamma}\left(\frac{a}{\pi L}\right)^{1-n_\gamma}\sum_{\mathbf{n}}^{(\prime)}\frac{1}{(\mathbf{n}^2+\mathbf{r}^2)\mathbf{n}^{2n_\gamma}}[1+\mathcal{O}((ML)^{-1})]. \tag{A16}$$

Contributions with different n_γ differ parametrically and can be matched independently between NRQED$_L$ and QED$_L$. The QED$_L$ amplitudes associated with the NLO diagrams in Fig. 6 are given by

$$\mathcal{M}_{\text{NLO}}^{\text{QED}_L}(n_\gamma) = -\frac{i64\pi^2 a^2}{L^3}\left(\frac{-\alpha}{2aM}\right)^{n_\gamma}\int\frac{dk^0}{2\pi}\sum_{\mathbf{n}}^{(\prime)}\frac{1}{(k^0+M)^2-\frac{4\pi^2(\mathbf{r}+\mathbf{n})^2}{L^2}-M^2+i\epsilon}$$
$$\times\frac{1}{(k^0-M)^2-\frac{4\pi^2(\mathbf{r}-\mathbf{n})^2}{L^2}-M^2+i\epsilon}\left(\frac{N_\gamma^\xi(k^0,\mathbf{n})}{(k^0)^2-\frac{4\pi^2\mathbf{n}^2}{L^2}+i\epsilon}\right)^{n_\gamma}, \tag{A17}$$

where

$$N_\gamma^\xi(k^0,\mathbf{n}) = (k^0)^2-4M^2+\left(\frac{4\pi^2}{L^2}\right)(4\mathbf{r}^2-\mathbf{n})^2-(1-\xi)\left[\frac{-(k^0)^4+4M^2(k^0)^2+(\frac{4\pi^2}{L^2})(4\mathbf{n}\cdot\mathbf{r}-\mathbf{n}^4)}{(k^0)^2-(\frac{4\pi^2}{L^2})\mathbf{n}^2+i\epsilon}\right]. \tag{A18}$$

The k^0 integral can be performed with contour integration. Closing the contour in the upper half plane, the result includes contributions from a particle pole $k^0 = M-\sqrt{M^2+4\pi^2(\mathbf{n}+\mathbf{r})^2/L^2} = -2\pi^2(\mathbf{n}+\mathbf{r})^2/(ML^2)[1+\mathcal{O}((ML)^{-2})]$, a photon pole at $k^0 = 2\pi|\mathbf{n}|/L$, and an antiparticle pole at $k^0 = -2M[1+\mathcal{O}((ML)^{-2})]$,

$$\mathcal{M}_{\text{NLO}}^{\text{QED}_L}(n_\gamma) = \frac{64\pi^2 a^2}{L^3}\left(\frac{-\alpha}{4aM}\right)^{n_\gamma}\sum_{\mathbf{n}}^{(\prime)}\left[\text{Res}\left(M-\sqrt{M^2+\frac{4\pi^2(\mathbf{n}+\mathbf{r})^2}{L^2}-i\epsilon}\right)\right.$$
$$\left.+\text{Res}\left(\frac{-2\pi|\mathbf{n}|}{L}+i\epsilon\right)+\text{Res}\left(-M-\sqrt{M^2+\frac{4\pi^2}{L^2}(\mathbf{n}-\mathbf{r})^2+i\epsilon}\right)\right]. \tag{A19}$$

Taking the $\epsilon \to 0$ limit and expanding to leading order in $(ML)^{-1}$, the residue at the particle pole is given by

$$\text{Res}\left(M-\sqrt{M^2+\frac{4\pi^2(\mathbf{n}+\mathbf{r})^2}{L^2}-i\epsilon}\right) = \frac{L^2}{16\pi^2 M}\left(\frac{M^2 L^2}{\pi^2}\right)^{n_\gamma}\frac{1}{(\mathbf{n}^2+\mathbf{r}^2)\mathbf{n}^{2n_\gamma}}. \tag{A20}$$

As in the NRQED$_L$ case, the residue at the photon pole $-2\pi|\mathbf{n}|/L$ is suppressed compared to the residue at the particle pole by $\mathcal{O}(ML)^{-1}$.

The residue at the antiparticle pole at $-2M(1+\mathcal{O}(ML)^{-1})$ does not appear in the corresponding NRQED$_L$ expression Eq. (A13) and is therefore associated with contributions that do not appear in loop diagrams in NRQED$_L$. This residue is given by

$$\text{Res}\left(-M-\sqrt{M^2+\frac{4\pi^2}{L^2}+i\epsilon}\right) = -\frac{1}{16M^3}\left(-\frac{\pi^2}{M^2 L^2}\right)^{n_\gamma}[2\mathbf{r}^2(-4+\xi)+\mathbf{n}^2(-3+2\xi)-4\mathbf{r}\cdot\mathbf{n}(-2+\xi)]^{n_\gamma}. \tag{A21}$$

The term involving two contact interactions involves the UV divergent sum $\sum_{\mathbf{n}}^{(\prime)}1$, which for $n_\gamma = 0$ must be consistent with the infinite-volume result $\int d^D k 1 = 0$ after subtracting UV counterterms,

$$\sum_{\mathbf{n} \in \mathbb{Z}^3} 1 \to 0. \tag{A22}$$

This leads to a vanishing contribution from the $n_\gamma = 0$ diagram appearing in the absence of QED_L, which is consistent with the expectation that antiparticle-pole contributions from off shell intermediate states that are absent nonrelativistically do not lead to power-law FV effects in local field theories. The terms with $n_\gamma \geq 1$ differ by zero mode subtraction. Since the $\mathbf{n} = 0$ contribution to $\sum_{\mathbf{n}} 1$ is unity, it follows from Eq. (A22) that

$$\sum_{\mathbf{n} \in \mathbb{Z}^3 \backslash \{\mathbf{0}\}} 1 \to -1. \tag{A23}$$

Sums with $\mathbf{n}^{2k}$ with $k > 0$ similarly require UV counterterms and vanish after including them. Zero-mode contributions to these sums vanish, and so

$$\sum_{\mathbf{n} \in \mathbb{Z}^3 \backslash \{\mathbf{0}\}} \mathbf{n}^{2k} \to 0, \tag{A24}$$

for $k > 0$. After subtracting UV counterterms the antiparticle pole contribution becomes

$$\begin{aligned}
\sum_{\mathbf{n} \in \mathbb{Z}^3 \backslash \{\mathbf{0}\}} &\mathrm{Res}\left(-M - \sqrt{M^2 + \frac{4\pi^2}{L^2} + i\epsilon}\right) \\
&\to \frac{1}{16M^3}\left(-\frac{\pi^2 2\mathbf{r}^2(-4 + \xi)}{M^2 L^2}\right)^{n_\gamma},
\end{aligned} \tag{A25}$$

for $n_\gamma \geq 1$. This leads to a finite contribution to $\mathcal{M}_{\mathrm{NLO}}^{\mathrm{QED}_L}$ that does not arise in the corresponding loop diagrams contributing to $\mathcal{M}_{\mathrm{NLO}}^{\mathrm{NRQED}_L}$. Local counterterms involving powers of L^{-1} must be added to the NRQED_L Lagrangian in order to reproduce this relativistic effect arising from zero-mode subtraction. Inserting Eq. (A25) into Eq. (A19) shows that the dominant contribution to $\mathcal{M}_{\mathrm{NLO}}^{\mathrm{QED}_L}$ arising from the $n_\gamma = 1$ diagram antiparticle pole is

$$-\frac{4\pi a}{M}\left(\frac{\alpha\pi^3(-4+\xi)\mathbf{r}^2}{4M^5 L^5}\right) = -\frac{8\pi a}{M}\left(\frac{\pi(-4+\xi)}{16}\right)\frac{\alpha}{(ML)^3}\left(\frac{\mathbf{p}^2}{M^2}\right). \tag{A26}$$

This contribution vanishes for FV systems in the two-particle rest frame where $\mathbf{p} = 0$. For boosted systems with a nonzero center-of-mass velocity [assumed to be nonrelativistic $\mathbf{p}^2 \ll M^2$ in the $(ML)^{-1}$ expansion above], this contribution is proportional to the LO contact interaction times the velocity squared times a relativistic QED suppression factor of $\alpha/(ML)^{-3}$. For boosted systems, the NRQED_L contact interaction in Eq. (A1) must therefore be supplemented with a nonlocal counterterm suppressed by the same factor of $\alpha/(ML)^{-3}$. This is analogous to the self-energy of a single scalar field, which is shown in Ref. [38] to require a nonlocal counterterm equal to the scalar mass times the velocity squared times a relativistic QED suppression factor of $\alpha/(ML)^{-3}$. The $\mathrm{LQCD} + \mathrm{QED}_L$ calculations discussed in the main text are performed in the center-of-mass rest frame, and these nonlocal counterterms vanish. Nonvanishing nonlocal counterterms appear for fermion masses in NRQED_L even in the two-particle rest frame, but since effects proportional to $(ML)^{-1}$ are neglected throughout this work it is consistent to neglect all nonlocal counterterms suppressed by $\alpha/(ML)^{-3}$.

The NLO QED_L amplitude is therefore given by inserting the particle-pole residue in Eq. (A20) into Eq. (A19),

$$\begin{aligned}
\mathcal{M}_{\mathrm{NLO}}^{\mathrm{QED}_L}(n_\gamma) = &\frac{4\pi a}{M}\left(-\frac{\alpha ML}{2\pi^3}\right)^{n_\gamma}\left(\frac{a}{\pi L}\right)^{1-n_\gamma} \\
&\times \sideset{}{'}\sum_{\mathbf{n}} \frac{1}{(\mathbf{n}^2 + \mathbf{r}^2)\mathbf{n}^{2n_\gamma}}[1 + \mathcal{O}((ML)^{-1})],
\end{aligned} \tag{A27}$$

which is identical to Eq. (A16). The $(ML)^{-1}$ suppression of diagrams in Figs. 7 and 8 arising from the absence of particle pole contributions is identical in QED_L and NRQED_L. Additional diagrams appearing in QED_L but not NRQED_L associated with the two-particle-two-photon vertex or particle-antiparticle pair creation can be similarly verified to be suppressed by powers of $(ML)^{-1}$. The NRQED_L Lagrangian in Eq. (A1) therefore reproduces QED_L at NLO.

Matching at NNLO proceeds similarly. The NNLO diagrams shown in Fig. 6 can all be expressed in terms of the amplitude

$$\begin{aligned}
\mathcal{M}_{\mathrm{NNLO}}^{\mathrm{NRQED}_L}(n_1, n_2, n_3) = &\frac{64\pi^3 a^3}{M^3 L^6}\left(\frac{\alpha M}{a}\right)^{n_1+n_2+n_3} \sideset{}{^{(\prime)}}\sum_{\mathbf{n},\mathbf{m}} \int \frac{dk^0}{2\pi} \frac{1}{(k^0 + \frac{2\pi^2(\mathbf{r}-\mathbf{n})^2}{ML^2} - i\epsilon)(k^0 - \frac{2\pi^2(\mathbf{r}+\mathbf{n})^2}{ML^2} + i\epsilon)} \left(\frac{1 - (1-\xi)\frac{(k^0)^2}{(k^0)^2 - \frac{4\pi^2\mathbf{n}^2}{L^2}}}{(k^0)^2 - \frac{4\pi^2\mathbf{n}^2}{L^2} + i\epsilon}\right)^{n_1} \\
&\times \int \frac{dq^0}{2\pi} \frac{1}{(q^0 + \frac{2\pi^2(\mathbf{r}-\mathbf{m})^2}{ML^2} - i\epsilon)(q^0 - \frac{2\pi^2(\mathbf{r}+\mathbf{m})^2}{ML^2} + i\epsilon)} \left(\frac{1 - (1-\xi)\frac{(k^0-q^0)^2}{(k^0-q^0)^2 - \frac{4\pi^2(\mathbf{n}-\mathbf{m})^2}{L^2}}}{(k^0-q^0)^2 - \frac{4\pi^2(\mathbf{n}-\mathbf{m})^2}{L^2} + i\epsilon}\right)^{n_2} \left(\frac{1 - (1-\xi)\frac{(q^0)^2}{(q^0)^2 - \frac{4\pi^2\mathbf{m}^2}{L^2}}}{(q^0)^2 - \frac{4\pi^2\mathbf{m}^2}{L^2} + i\epsilon}\right)^{n_3},
\end{aligned} \tag{A28}$$

where $n_i \in \{0, \}$ for $i \in \{1, 2, 3\}$ labels whether each interaction is a four-particle contact interaction or photon exchange and $\sum_{\mathbf{n,m}}{}^{(\prime)}$ excludes $\mathbf{n} = 0$ if $n_1 = 1$ or $n_2 = 1$ and excludes $\mathbf{m} = 0$ if $n_2 = 1$ or $n_3 = 1$. Both energy

integrands include poles where a particle is on shell as well as poles where a photon is on shell, and, as above, photon-pole contributions are suppressed by $\mathcal{O}((ML)^{-1})$. Evaluating the q^0 and k^0 integrals then gives

$$
\begin{aligned}
\mathcal{M}_{\mathrm{NNLO}}^{\mathrm{NRQED}_L}(n_1, n_2, n_3) = &-\frac{4\pi a}{M}\left(\frac{a}{\pi L}\right)^{2-n_1-n_2-n_3}\left(-\frac{\alpha ML}{2\pi^3}\right)^{n_1+n_2+n_3} \\
&\times \sum_{\mathbf{n,m}}{}^{(\prime)}\frac{1}{(\mathbf{n}^2 + \mathbf{r}^2)(\mathbf{m}^2 + \mathbf{r}^2)\mathbf{n}^{2n_1}(\mathbf{n} - \mathbf{m})^{2n_2}\mathbf{m}^{2n_3}}[1 + \mathcal{O}((ML)^{-1})],
\end{aligned}
\tag{A29}
$$

where UV counterterms should be included as in Eq. (A15). Similarly to the NLO case, the NNLO diagrams in Figs. 7 and 8 only include photon pole contributions and are suppressed by $\mathcal{O}((ML)^{-1})$ or $\mathcal{O}((ML)^{-2})$ compared to Eq. (A29).

The corresponding QED_L NNLO amplitudes are given by

$$
\begin{aligned}
\mathcal{M}_{\mathrm{NNLO}}^{\mathrm{QED}_L}(n_1, n_2, n_3) = &\frac{1024\pi^3 a^3 M}{L^6}\left(-\frac{\alpha}{4aM}\right)^{n_1+n_2+n_3}\sum_{\mathbf{n,m}}{}^{(\prime)}\int\frac{dk^0}{2\pi}\left(\frac{N_\gamma^\xi(k^0, \mathbf{n})}{(k^0)^2 - \frac{4\pi^2\mathbf{n}^2}{L^2} + i\epsilon}\right)^{n_1} \\
&\times \frac{1}{((k^0 - M)^2 - \frac{4\pi^2(\mathbf{n}-\mathbf{r})^2}{L^2} - M^2 + i\epsilon)((k^0 + M)^2 - \frac{4\pi^2(\mathbf{n}+\mathbf{r})^2}{L^2} - M^2 + i\epsilon)} \\
&\times \int\frac{dq^0}{2\pi}\left(\frac{N_\gamma^\xi(k^0 - q^0, \mathbf{n} - \mathbf{m})}{(k^0 - q^0)^2 - \frac{4\pi^2(\mathbf{n}-\mathbf{m})^2}{L^2} + i\epsilon}\right)^{n_2}\left(\frac{N_\gamma^\xi(q^0, \mathbf{m})}{(q^0)^2 - \frac{4\pi^2\mathbf{m}^2}{L^2} + i\epsilon}\right)^{n_3} \\
&\times \frac{1}{((q^0 - M)^2 - \frac{4\pi^2(\mathbf{m}-\mathbf{r})^2}{L^2} - M^2 - i\epsilon)((q^0 + M)^2 - \frac{4\pi^2(\mathbf{m}+\mathbf{r})^2}{L^2} - M^2 + i\epsilon)}.
\end{aligned}
\tag{A30}
$$

Contributions from photon and antiparticle poles are again suppressed by powers of $(ML)^{-1}$, and evaluating the q^0 and k^0 energy integrals gives

$$
\begin{aligned}
\mathcal{M}_{\mathrm{NNLO}}^{\mathrm{QED}_L}(n_1, n_2, n_3) = &-\frac{4\pi a}{M}\left(\frac{a}{\pi L}\right)^{2-n_1-n_2-n_3}\left(-\frac{\alpha ML}{2\pi^3}\right)^{n_1+n_2+n_3} \\
&\times \sum_{\mathbf{n,m}}{}^{(\prime)}\frac{1}{(\mathbf{n}^2 + \mathbf{p}^2)(\mathbf{m}^2 + \mathbf{p}^2)\mathbf{n}^{2n_1}(\mathbf{n} - \mathbf{m})^{2n_2}\mathbf{m}^{2n_3}}[1 + \mathcal{O}((ML)^{-1})].
\end{aligned}
\tag{A31}
$$

All other diagrams are again suppressed by powers of $(ML)^{-1}$, and agreement between Eqs. (A29) and (A31) shows that nonlocal counterterms are suppressed by powers of $(ML)^{-1}$ and can be neglected to the accuracy considered here.

While the matching in this section has been explicitly performed for scalar QED_L, the $(ML)^{-1}$ suppression of photon and antiparticle poles only relies on the structure of QED_L propagator denominators that are identical for scalars and fermions. The $(ML)^{-3}$ suppression of antiparticle pole contributions leading to nonlocal two-body counterterms also arises from the denominator structure of the QED_L propagators and is expected to be generic for bosons and fermions. The numerator structure of the scalar QED_L propagators above is relevant for $(ML)^{-1}$ suppressed relativistic effects, and in particular the scalar QED_L antiparticle pole in Eq. (A21) includes

vanishing numerator factors for a system at rest that lead to $\mathbf{p}^2/M^2$ velocity suppression of nonlocal counterterms in scalar NRQED_L. This cancellation might be absent for fermions, and nonlocal two-body counterterms might be relevant for QED_L calculations of charged fermions in the center-of-mass rest frame. This would parallel the situation for one-body nonlocal counterterms, which arise at $\mathcal{O}(\alpha/(ML)^3)$ for fermions with any center-of-mass velocity and for scalars with nonzero center-of-mass velocity.

APPENDIX B: FITTING PROCEDURES

1. Energy level determination

In general the spectral representation in Eq. (8) cannot be inverted to determine the full energy spectrum from finite samples of correlation functions over a finite range of

source/sink separations. Any fitting procedure to extract energies from correlation functions involves making several choices, in particular the range of t to include in the fit, the number of excited states to include in a truncation of Eq. (8) to use as a fitting model, and how to estimate the covariance matrix from a finite statistical ensemble. In order to assess the systematic uncertainties associated with these fitting choices and provide a reproducible procedure for extracting energy levels from correlation function results, we use an approach detailed here for making fitting choices based on well-defined statistical criteria and random sampling over the space of possible fitting choices.

The first step in this fitting procedure is choosing the maximum source/sink separation $t_{\max}$ included in the fit. For (multi)baryon correlation functions, the signal-to-noise (SN) problem implies that results with larger temporal separation t make exponentially smaller contributions to χ^2 when fitting energy levels from correlation functions. For the nucleon, the scaling $\mathrm{SN}(G) = G(t)/\sqrt{\mathrm{Var}(G(t))} \sim e^{-(M_N - \frac{3}{2}m_\pi)t}$ predicted by Parisi [95] and Lepage [96] applies in the limit of a large statistical ensemble size $N \to \infty$ and shows that fit results are exponentially insensitive to the choice of $t_{\max}$. Similar results apply for multinucleon systems with baryon number A where $\mathrm{SN}(G) = G(t)/\sqrt{\mathrm{Var}(G(t))} \sim e^{-A(M_N - \frac{3}{2}m_\pi)t}$ for large t. For fixed N (and, since volume-averaging increases SN, for fixed L) it is important to choose a fixed $t_{\max}$ before the SN has degraded to the point where correlation function estimates are unreliable.[11] The SN ratio decreases with t at small and intermediate t before saturating at an $\mathcal{O}(1)$ value in the noise region, and to avoid the noise region $t_{\max}$ should not exceed the smallest t where $\mathrm{SN}(G) = G(t)/\sqrt{\mathrm{Var}G(t)}$ reaches a specified $\mathcal{O}(1)$ cutoff. For positive-definite meson correlation functions this issue does not arise, and the maximum t that can be reliably included in the fit is only limited by the accuracy by which finite-temperature effects are modeled. In this work, finite-temperature excited-state effects are neglected, and finite-temperature effects on correlation functions with $t \sim T/2$, where T is the length of the Euclidean time direction, are not reliably modeled. In our fitting procedure, $t_{\max}$ is therefore chosen to be the minimum t satisfying either: the correlation function noise-to-signal ratio at $(t + a)$ is smaller than a specified tolerance (final results use $\mathrm{tol}_{\mathrm{noise}} = 1.0$), the correlation

function sample mean at $t + a$ is negative,[12] or $t + a$ is larger than a finite-temperature cutoff (final results use $\mathrm{tol}_{\mathrm{temp}} = 3T/8$). The values of $\mathrm{tol}_{\mathrm{noise}}$ and $\mathrm{tol}_{\mathrm{temp}}$ are free parameters in our fitting procedure that must be varied to assess the sensitivity of fit results to these choices; for concreteness the parameter choices are presented here that lead to the final results quoted in the main text. Results are found to be relatively insensitive to the parameter choices controlling $t_{\max}$, and for example varying the noise tolerance in the range $\mathrm{tol}_{\mathrm{noise}} \in [0.1, 1]$ leads to results with consistent central values at the 1σ level and few-percent variation of the corresponding uncertainties.

The next step in our fitting procedure is to choose $t_{\min}$, the minimum t included in the fit. The choice of $t_{\min}$ significantly impacts how well excited-state effects at small t can be resolved and how many excited states should be included in fits. Furthermore, the uncertainties of energy-level determinations are exponentially sensitive to the choice of $t_{\min}$ for baryons because of the SN problem. Fit results are therefore more sensitive to the choice of $t_{\min}$ than to the choice of $t_{\max}$. Rather than choose a single $t_{\min}$, it is preferable to sample from many possible choices of $t_{\min}$ and quantify the sensitivity to this choice as the systematic error. The minimum permissible $t_{\min}$ is fixed by the temporal nonlocality in the lattice action, and for the improved action used in this work the transfer matrix involves fields on two adjacent timeslices [98] and $t_{\min} \geq 2$ is required. The largest allowed $t_{\min}$ is limited by $t_{\min} \leq t_{\max} - t_{\mathrm{plateau}}$, where t_{plateau} is a free parameter that is not found to significantly affect final results when varied over the range $2 \lesssim t_{\mathrm{plateau}} \lesssim 8$ (final results use $t_{\mathrm{plateau}} = 4$). For each type of interpolating operator included in a combined fit, $t_{\min}$ is sampled randomly within this range until either all possible values of $t_{\min}$ have been chosen or a maximum of $N_{\mathrm{fits}} = 200$ fits have been performed.

With $t_{\min}$ and $t_{\max}$ specified, the covariance matrix $\mathcal{C}_{tt'}^{ij}$ must be estimated for $t_{\min} \leq t, t' \leq t_{\max}$ and interpolating operators $i, j \in \{1, \dots N_{\mathrm{op}}\}$. Fits involving a large number N_{pts} of time separations and interpolating operator choices may not satisfy the condition $N \gg N_{\mathrm{pts}}^2$ needed to ensure that the N terms contributing to the $N_{\mathrm{pts}} \times N_{\mathrm{pts}}$ sample covariance can accurately estimate the true underlying

---

[11]The complex phases of baryon correlation functions are circular random variables, and there is therefore a noise region at large t where $\ln N$ is not much larger than the variance of the phase distribution and the sample mean is a systematically unreliable estimator of the average correlation function [97].

[12]If the average correlation function is not expected to be positive definite, then this condition should not be enforced. In principle, the source and sink interpolating operators used in this work differ from one another, and it is possible for the sign of an average correlation function to fluctuate at small t where excited-state contributions with opposite sign to the ground-state contribution can be significant. In practice, small t fluctuations of the sign of the sample mean correlation function that could be attributed to excited-state effects are not observed in this work, and a negative sample mean correlation function is taken as an indicator of large statistical noise.

covariance matrix, where N_{pts} is the total number of source/sink separations from all interpolating operators included in the fit. Shrinkage techniques have been developed to provide more accurate estimates of the underlying covariance matrix than the sample covariance matrix when $N \gg N_{\mathrm{pts}}^2$ is not satisfied [60,61]. Shrinkage estimators $\mathcal{S}_{tt'}^{ij}(\lambda)$ of the covariance matrix are constructed as mixtures of a well-conditioned target matrix $T_{tt'}^{ij}$ and the covariance matrix $\mathcal{C}_{tt'}^{ij}$ estimated using standard bootstrap techniques from $N_{\mathrm{boot}} = 200$ samples of N correlation functions $G_{i,a}^{b}(t)$ with $a \in \{1, ..., N\}$ and $b \in \{1, ..., N_{\mathrm{boot}}\}$ drawn from the original correlation function ensemble with the replacement

$$\mathcal{S}_{tt'}^{ij}(\lambda) = \mathcal{C}_{tt'}^{ij}(1 - \lambda) + T_{tt'}^{ij}\lambda, \qquad (\mathrm{B1})$$

where $0 \leq \lambda \leq 1$ is a shrinkage parameter. A common choice of well-conditioned target matrix for many problems in statistics is the identity matrix; however, this does not accurately describe the underlying covariance matrix for correlation functions whose diagonal entries decrease exponentially with t. Following applications of shrinkage to lattice QCD in Ref. [62], we take $T_{tt'}^{ij} = \mathrm{diag}(\mathcal{C}_{tt'}^{ij})$. In this case, shrinkage corresponds to an interpolation between a fully correlated fit with $\lambda = 0$ and an uncorrelated fit with $\lambda = 1$. Shrinkage gives an unbiased estimator of the underlying covariance matrix in the infinite-statistics limit provided λ vanishes sufficiently quickly in this limit. It can be shown [61] that for finite N an optimal $\lambda^* \neq 0$ satisfying this restriction can be chosen in order to minimize the average mean-squared difference between $\mathcal{S}_{tt'}^{ij}(\lambda)$ and the underlying covariance matrix, and that a sample estimate for λ^* is given by

$$\lambda^* = \mathrm{Max}\Bigg(0,$$

$$\times \mathrm{Min}\Bigg(1, \frac{\sum_{a=1}^{N}\sum_{t,t',i,j}[\tilde{G}_a^i(t)\tilde{G}_a^j(t') - \bar{\tilde{S}}^{ij}(t,t')]^2}{N^2 \sum_{t,t',i,j}[\bar{\tilde{S}}^{ij}(t,t') - \delta^{ij}\delta_{t,t'}]^2}\Bigg)\Bigg),$$

$$(\mathrm{B2})$$

where

$$\tilde{G}_a^i(t) = \frac{G_a^i(t) - \bar{G}^i(t)}{\sqrt{\bar{S}^{ii}(t,t)}},$$

$$\bar{\tilde{S}}^{ij}(t,t') = \frac{\bar{S}^{ij}(t,t')}{\sqrt{\bar{S}^{ii}(t,t)\bar{S}^{jj}(t',t')}} \qquad (\mathrm{B3})$$

are defined in terms of the sample mean correlation function and sample covariance as in Ref. [62],

$$\bar{G}^i(t) = \frac{1}{N}\sum_{a=1}^{N} G_a^i(t),$$

$$\bar{S}^{ij}(t,t') = \frac{1}{N-1}\sum_{a=1}^{N}[G_a^i(t)G_a^j(t') - \bar{G}^i(t)\bar{G}^j(t')], \qquad (\mathrm{B4})$$

such that shrinkage of $\bar{\tilde{S}}^{ij}(t,t')$ with $T_{tt'}^{ij} = \mathrm{diag}(\bar{\tilde{S}}_{tt'}^{ij})$ corresponds to shrinkage of $\bar{\tilde{S}}^{ij}(t,t')$ with the identity matrix as a target, and the results of Ref. [61] assuming an identity matrix target can be applied. The covariance matrix estimate with optimal shrinkage is then given by $\mathcal{S}_{tt'}^{ij}(\lambda^*)$. Fits to truncations of Eq. (8) including e excited states can then be performed by minimizing the corresponding χ^2 function defined by

$$\chi^2 = \sum_{t,t'=t_{\mathrm{min}}}^{t_{\mathrm{max}}} \sum_{i,j=1}^{N_{\mathrm{op}}} (\bar{G}_i^B(t) - f(t,\mathbf{E},\mathbf{Z}))$$

$$\times [\mathcal{S}(\lambda^*)^{-1}]_{tt'}^{ij}(\bar{G}_j^B(t') - f(t',\mathbf{E},\mathbf{Z})), \qquad (\mathrm{B5})$$

where $\bar{G}_i^B = 2\bar{G}_i - \frac{1}{N_{\mathrm{boot}}}\sum_{b=1}^{N_{\mathrm{boot}}} \bar{G}_i^b$ includes a $1/N$ bias correction estimated using bootstrap techniques and $\mathbf{E}$ and $\mathbf{Z}$ denote the energies and overlap factors appearing in Eq. (8), including excited-state and thermal effects. Since the overlap factors enter f_N linearly, the values of $\mathbf{Z}$ minimizing χ^2 for fixed $\mathbf{E}$ can be determined by solving a system of linear equations analogous to variable projection techniques [99,100]. χ^2 minimization can therefore be efficiently performed by using a nonlinear optimization method to determine $\mathbf{E}$ with the optimal $\mathbf{Z}$ determined by solving a system of linear equations at each step of nonlinear optimization for $\mathbf{E}$. In order to ensure positivity of the spectrum and remove fitting degeneracies, the parameters used for nonlinear optimization are $\ln E_0$ and $\ln(E_k - E_{k-1})$ for $1 \leq k \leq e$.

For each randomly sampled choice of t_{min}, the next step in the fitting procedure is to determine the number of excited states to be included in the sum of exponentials used as a fit function. This is done by first performing a fit including zero excited states and then adding successively more excited states until the addition of the next excited state does not improve the goodness of fit according to an information criterion. This work employs the Akaike information criterion [101] (AIC) with a cutoff chosen to penalize overfitting in which a fit with e excited states is only preferred over a fit with $e - 1$ excited states if $\mathrm{AIC}(e) - \mathrm{AIC}(e-1) < -\mathcal{A}N_{\mathrm{dof}}(e)$ where $N_{\mathrm{dof}}(e) = N_{\mathrm{pts}} - N_{\mathrm{params}}(e)$ is the number of degrees of freedom of the fit, $N_{\mathrm{params}}(e)$ is the number of fit parameters for a fit with e excited states, and $\mathrm{AIC}(e) = 2N_{\mathrm{params}}(e) + \chi^2(e) + k$ with $\chi^2(e)$ the (unreduced) χ^2 of the fit defined in Eq. (B5) and k is an irrelevant e-independent constant. This choice corresponds to a preference for an e state fit only if it

improves the χ^2/N_{dof} by an $\mathcal{O}(1)$ value $\mathcal{A}$ compared to the $(e-1)$ state fit. For baryon correlation functions a value of $\mathcal{A} = -0.5$ is used, while for multimeson correlation functions a value of $\mathcal{A} = -0.1$ is used.[13]

Bootstrap resampling techniques are then used to estimate the uncertainty on the ground-state energy extracted from the fit with the preferred number of excited states in each fit region [102,103]. The same χ^2-minimization procedure and estimated covariance matrix $\mathcal{S}(\lambda^*)$ are used to determine the spectrum for each of N_{boot} bootstrap resampled ensembles. Results are found to be insensitive to the choice of N_{boot}, and final results use $N_{\mathrm{boot}} = 200$. The 67% confidence interval for the ground-state energy is then obtained from the quantiles of the distribution of differences between the bth bootstrap sample result $E_0^{b,f}$ and the fit result E_0^f obtained for fit range f,

$$\delta E_0^f = \frac{1}{2}[Q_{5/6}(E_0^{b,f} - E_0^f) - Q_{1/6}(E_0^{b,f} - E_0^f)], \quad \text{(B6)}$$

where $Q_p(x^f)$ is the pth quantile of the set of fit results with elements x^f. Using this definition δE_0^f minimizes the impact of outlier bootstrap samples compared to a definition based on the standard deviation of $E_0^{b,f} - E_0^f$ [103]. An analogous procedure is used to estimate uncertainties for excited-state energies and overlap factors.

Several additional checks are used to ensure the robustness of χ^2-minimization results: two different optimization algorithms, Nelder-Mead and conjugate gradient, are used[14] and are verified to give energies that differ by less than a specified tolerance[15] (final results use $\mathrm{tol}_{\mathrm{sol}} = 10^{-5}$), median results for ground- and excited-state energies from the bootstrap samples are verified to agree with fit results from the average correlation functions for each energy level within a specified tolerance (final results use $\mathrm{tol}_{\mathrm{med}} = 2\sigma$), uncorrelated fit results obtained by repeating the χ^2-minimization procedure with $\mathcal{S}(\lambda{=}1)$ are verified to give consistent results for each energy level within a specified tolerance (final results use $\mathrm{tol}_{\mathrm{corr}} = 5\sigma$), the χ^2/N_{dof} is verified to be less than a specified tolerance (final results use $\mathrm{tol}_{\chi^2} = 2$). This defines a reproducible and automatable

procedure for fitting correlation functions, including sampling of possible fit ranges and excited-state model selection, in which fit results are functions of only the tolerances described above and the given correlation functions. A graphical illustration of the fitting procedure is shown in Fig. 16. This fitting procedure was implemented in the JULIA language [104] using the OPTIM optimization package [105] to obtain the results of this work.

Fits that pass all of the checks above are considered reliable estimates of the energy spectrum, and the final estimate of the ground-state energy $\bar{E}_0$ and its uncertainty $\delta\bar{E}_0$ are obtained by taking a weighted average of the N_{success} successful fit results E_0^f,

$$\bar{E}_0 = \sum_{f=1}^{N_{\mathrm{success}}} w^f E_0^f, \quad \delta_{\mathrm{stat}}\bar{E}_0^2 = \sum_{f=1}^{N_{\mathrm{success}}} w^f (\delta E_0^f)^2,$$

$$\delta_{\mathrm{sys}}\bar{E}_0^2 = \sum_{f=1}^{N_{\mathrm{success}}} w^f (E_0^f - \bar{E}_0)^2, \quad \delta\bar{E}_0 = \sqrt{\delta_{\mathrm{stat}}\bar{E}_0^2 + \delta_{\mathrm{sys}}\bar{E}_0^2},$$

$$\text{(B7)}$$

where f labels the choice of fit range specified by t_{min} for each interpolating operator.[16] Each fit result provides an unbiased estimate of the ground-state energy. The relative weights w_f of each fit in the weighted average can therefore be chosen arbitrarily in the limit of large statistics; in practice it is advantageous to choose weights that penalize poor fits with larger χ^2/N_{dof} and unconstraining fits with larger uncertainties δE_0^f. Following Ref. [62], we use the weights

$$\tilde{w}^f = \frac{p_f(\delta E_0^f)^{-2}}{\sum_{f'=1}^{N_{\mathrm{success}}} p_{f'}(\delta E_0^{f'})^{-2}}, \quad \text{(B8)}$$

where $p_f = \Gamma(N_{\mathrm{dof}}/2, \chi_f^2/2)/\Gamma(N_{\mathrm{dof}}/2)$ is the p-value assuming χ^2-distributed goodness-of-fit parameters with χ_f^2 obtained by inserting E_0^f into Eq. (B5).[17] Variation to the

---

[13]Optimal shrinkage values of $\lambda^* \gtrsim 0.1$ appear for n-meson correlation functions with $n \gtrsim 6$ and χ^2 values are correspondingly lower than would be expected for fully correlated χ^2 minimization, leading to smaller absolute changes in AIC for multimeson correlation functions than for multibaryon correlation function. Increasing $-\mathcal{A}$ from 0.1 over the range $-\mathcal{A} \in [0.1, 2]$ leads to consistent results with larger uncertainties because precise and accurate two-state fits with small t_{min} are rejected in favor of one-state fits more frequently.

[14]Newton's method is used in place of Nelder-Mead if $N_{\mathrm{states}} = 1$, since Nelder-Mead does not work for a single fit parameter.

[15]Fits resulting in ground-state energies less than $\mathrm{tol}_{\mathrm{sol}}$, which appeared only for the $11\bar{K}^0$ system on the $L/a = 32$ lattice volume, were also rejected.

[16]The total error $\delta\bar{E}_0$ describes the combined statistical uncertainty on $\bar{E}_0$ plus systematic uncertainty arising from the choice of fit range and fit model. The partitioning of this error into $\delta_{\mathrm{stat}}\bar{E}_0$ and $\delta_{\mathrm{sys}}\bar{E}_0$ only partially separates statistical and systematic uncertainties because $\delta_{\mathrm{stat}}E_0$ includes statistical errors plus systematic uncertainties related to fluctuations among the δE_0^f.

[17]For large λ^*, the χ^2 function being minimized approaches an uncorrelated χ^2 and the values of χ^2 will not be distributed as χ^2-distributed random variables with N_{dof} degrees of freedom. In this regime where finite N artifacts are not negligible, the weights in Eq. (B8) still serve the purpose of penalizing comparatively less accurate descriptions of the results being fit and their correlations as estimated by $\mathcal{S}_{tt'}^{ij}(\lambda^*)$, but the absolute sizes of the p_f should not be interpreted as p values for each fit.
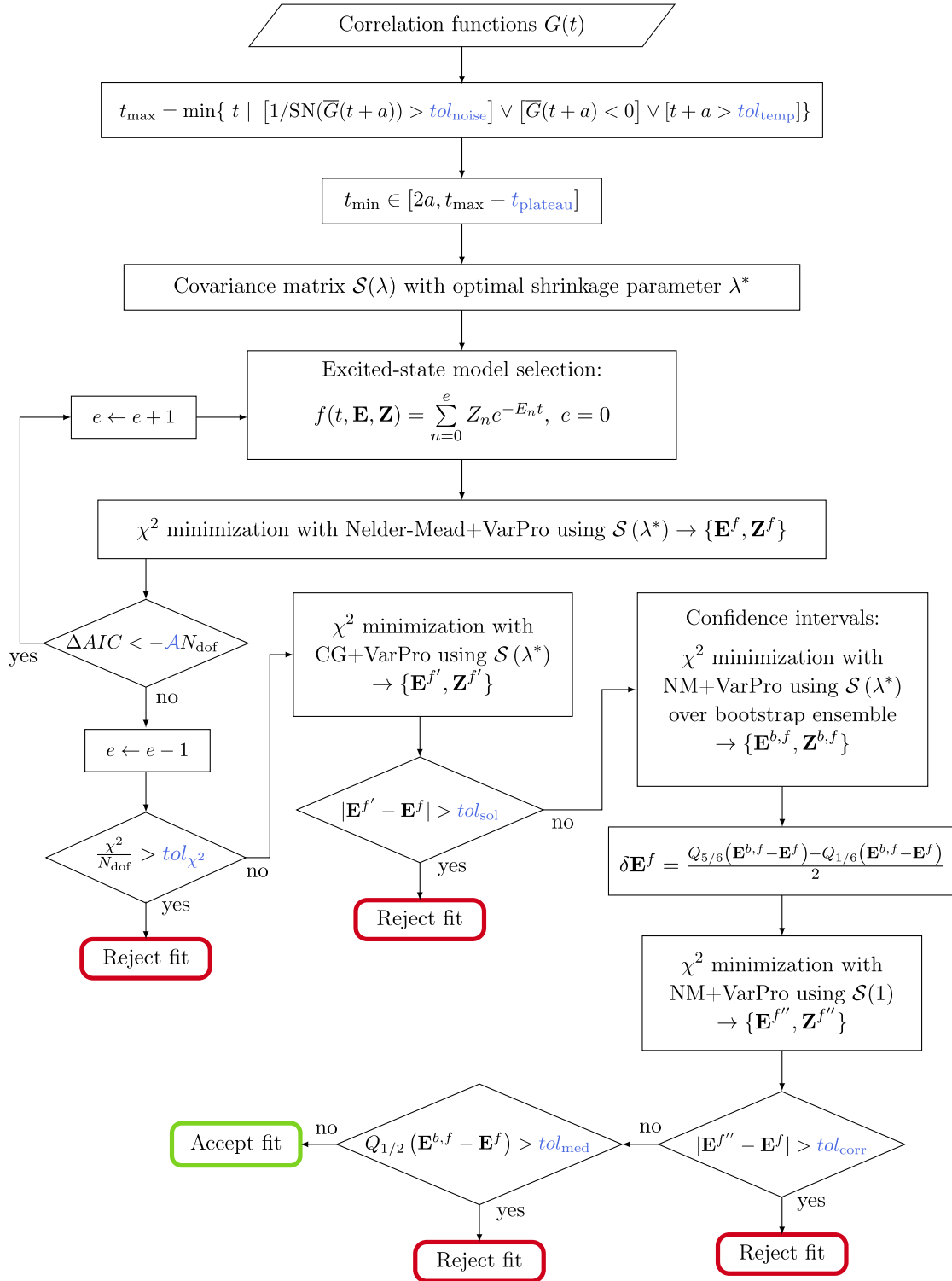
FIG. 16. Flowchart representing the steps of the fitting procedure for one specific fitting range. Rectangular shapes represent process steps, while diamond shapes represent decision steps. Input parameters to the fitting procedure are shown in blue. As described in the text, the steps illustrated here are repeated N_{fits} times with different random choices of t_{min}, and final results are obtained from weighted averages of fit results for the t_{min} choices leading to the "accept fit" rectangle. NM = Nedler $-$ Mead optimization algorithm; CG = conjugate gradient optimization algorithm.

particular choices of specified tolerances have been studied, and the subsequent variation in the ensemble of successful fits is found to have little impact on the results of this weighted averaging. The results $\bar{E}_0$ and $\delta\bar{E}_0$ obtained with this procedure are shown as the central values and uncertainties for single-particle energy results $E_{\pi^+}(L)$, $E_{\bar{K}^0}(L)$, $E_n(L)$, and $E_p(L)$ in Tables II and III. Effective mass plots showing the smallest $t_{\min}$ fit with weight over $1/2$ of the maximum weight fit as well as E_0^f and $\tilde{w}^f/\mathrm{Max}(\tilde{w}^f)$ are shown in Appendix B 4.

2. Multimeson correlation functions

To determine results for multi-meson ground-state energies with thermal effects taken into account, fits are performed iteratively starting with fits for $n = 1$ mesons and then moving to fits with increasing n. The excited-state fit form in Eq. (8) includes thermal effects describing k forwards-propagating mesons and $n - k$ backwards-propagating mesons for $k < n/2$ that are included by using the central values $\bar{E}_0$ calculated for E_k and E_{n-k} in Eq. (8). Uncertainties in E_k are found to be significantly smaller than uncertainties in E_n for $k < n/2$, and for simplicity are not incorporated into the description of thermal effects. The overlap factors for these thermal states are determined using linear algebra techniques [99,100] during each step of nonlinear optimization for the N-particle energy spectrum analogously to the procedure described above for other overlap factors. This fit function is found to provide acceptable fits to multimeson correlation functions without the need for additional free parameters describing excited-state thermal effects.

Before beginning the fitting procedure described above, correlation function results from all quark propagator sources on a given configuration are averaged and meson correlation functions are further blocked along the Markov chain to form $N_{\mathrm{block}} = 200$ approximately independent samples from the N_{cfg} configurations for each volume shown in Table I. Further averaging is found to give statistically consistent results, suggesting that autocorrelations can be neglected after this blocking. To determine correlated differences of ground-state energies for different hadron type (π^+, $\bar{K}^0$) and hadron number, fits are performed independently to determine E_0^f for each hadron type and number for each fit range sampled. A fit range is considered to give a successful

fit only if the checks on fit robustness described above are passed for each hadron type and number involved in the correlated difference. For each successful fit range, bootstrap resampling is used to determine the uncertainties on correlated differences of the resulting E_0^f. During bootstrap resampling, the same elements of these N_{block} samples are used to construct bootstrap ensembles for each hadron type and number. Correlated differences of the bootstrap results $E_0^{f,b}$ are then formed, and confidence intervals are computed by applying Eq. (B6) to the these correlated differences. Finally, weighted averages of the resulting correlated differences and their associated uncertainties are taken using Eqs. (B7) and (B8). The results of this procedure are used to determine the FV energy shifts and differences between FV energy shifts for charged and uncharged hadrons shown in Tables III–IV.

3. Multinucleon correlation functions

Differences between multinucleon ground-state energies and the corresponding sums of their constituent nucleon masses are computed using correlated differences of bootstrap results $E_0^{f,b}$ for multinucleon and single-nucleon correlation functions analogously to the multimeson case described above. Correlated differences between one-nucleon and multinucleon energies can be determined much more precisely than multinucleon energies alone, and differences of one-nucleon and multinucleon fit results with different values of N_{states} are found to describe correlated differences of $\mathrm{LQCD} + \mathrm{QED}_L$ effective energy results poorly. N_{states} is therefore restricted to be identical between single-nucleon and multinucleon systems. Otherwise, fits for multinucleon energy shifts are performed identically to fits for multimeson energy shifts not including thermal effects.

4. Fit results

Figures 17–19 show fit results for $n\pi^+$ systems with $L/a = 32$. Results with $L/a = 48$ are shown in Figs. 1–3. Figures 20–25 show analogous fit results for $n\bar{K}^0$ systems with $L/a \in \{32, 48\}$. Single-nucleon fit results for p and n are shown in Fig. 26. Two-nucleon fit results are shown for pp and nn in Fig. 27 and for np systems in Fig. 28. Three-nucleon fit results are shown in Fig. 29.
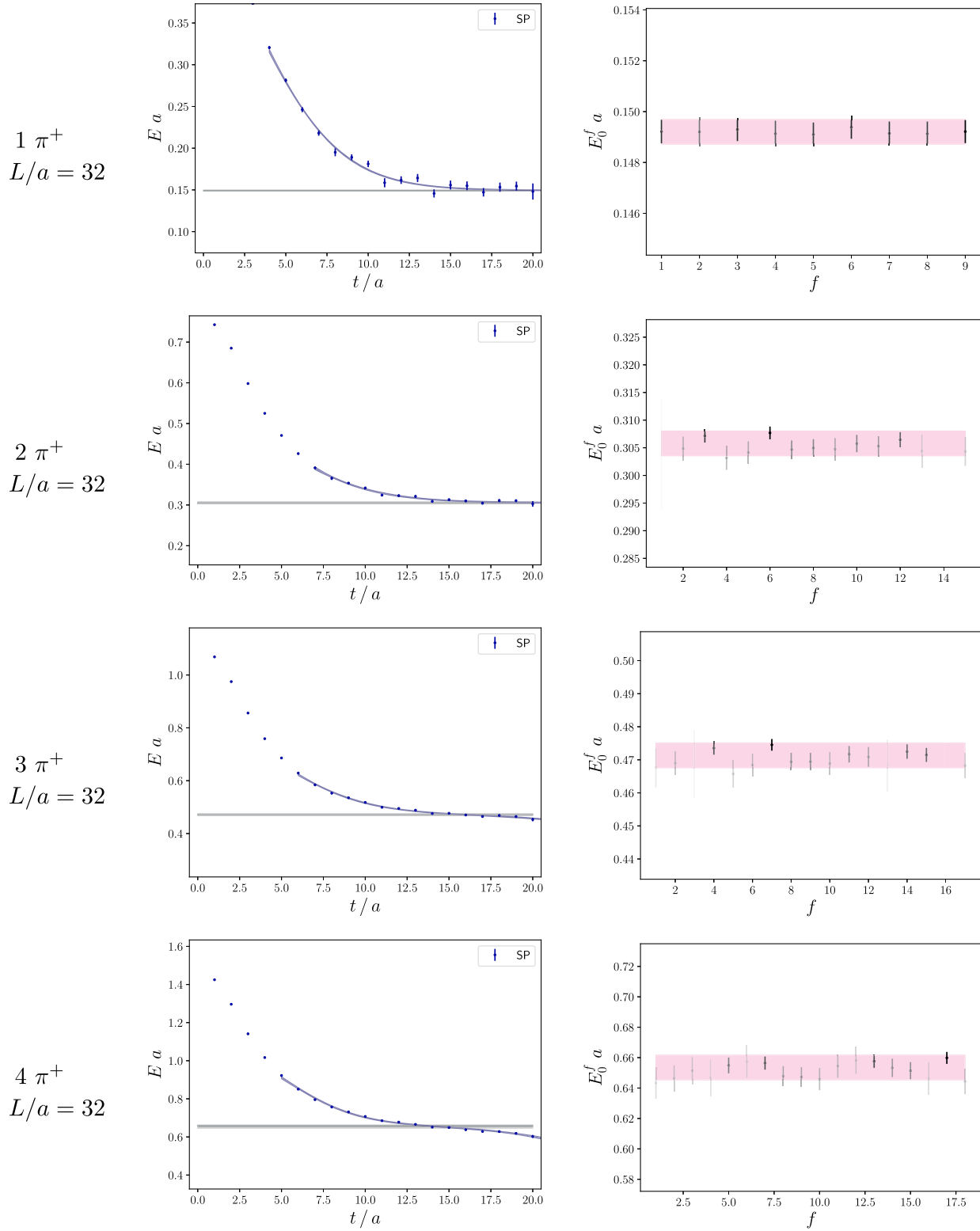
FIG. 17.   Fit results for systems of $n \in \{1, \ldots, 4\}\pi^+$ mesons for the $L/a = 32$ lattice volume. The figures are analogous to Fig. 1, see Appendix B for a definition of the fitting procedure employed.
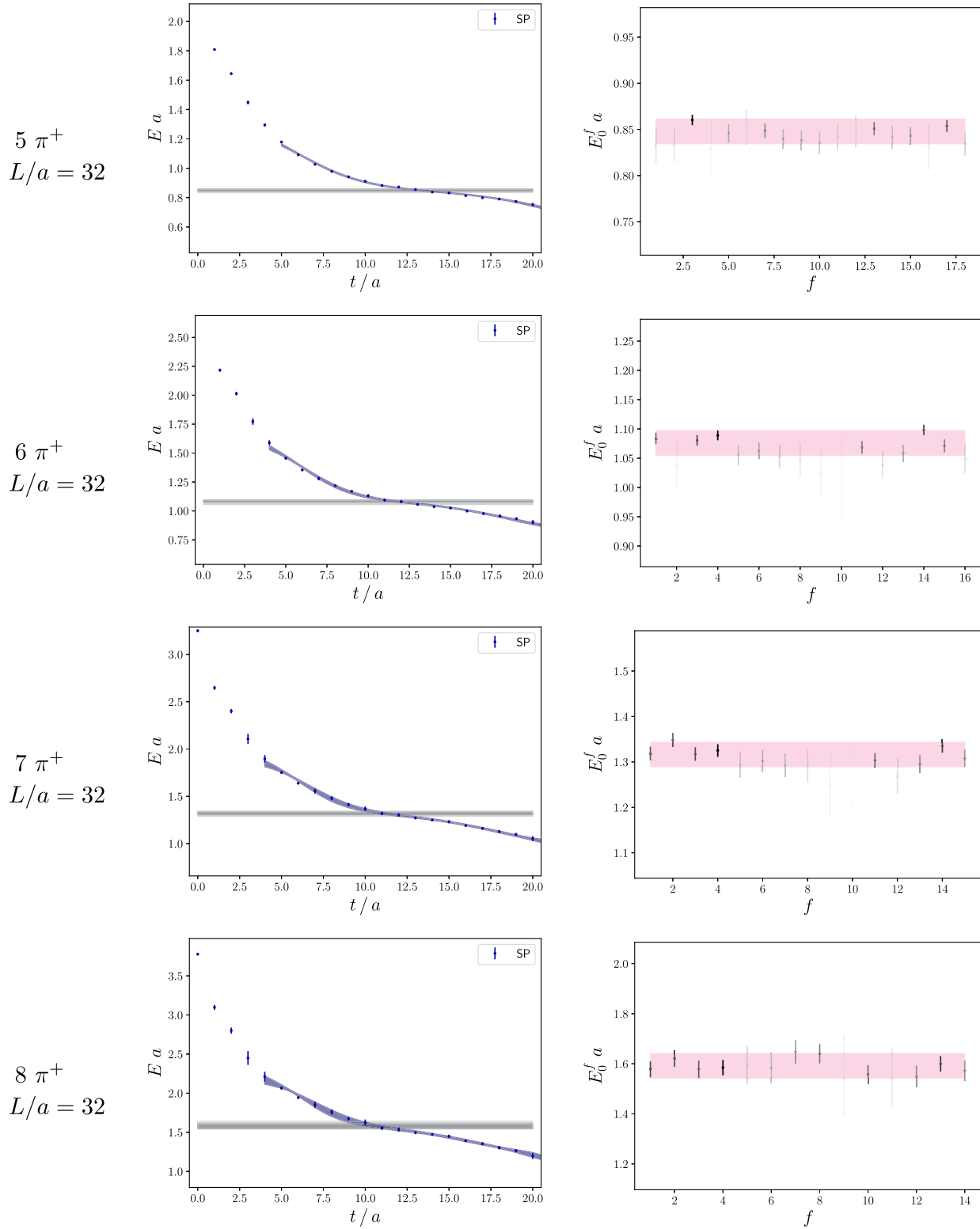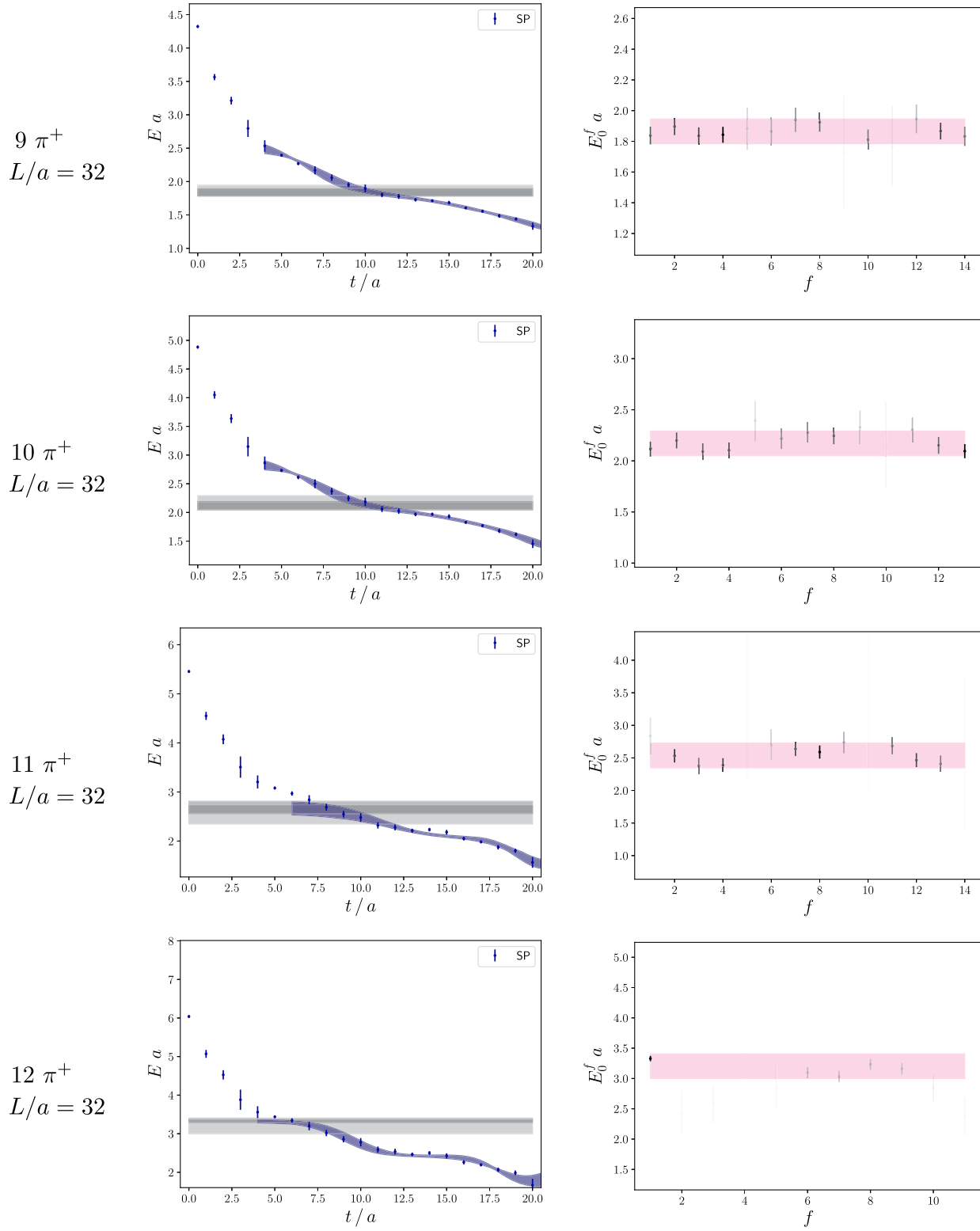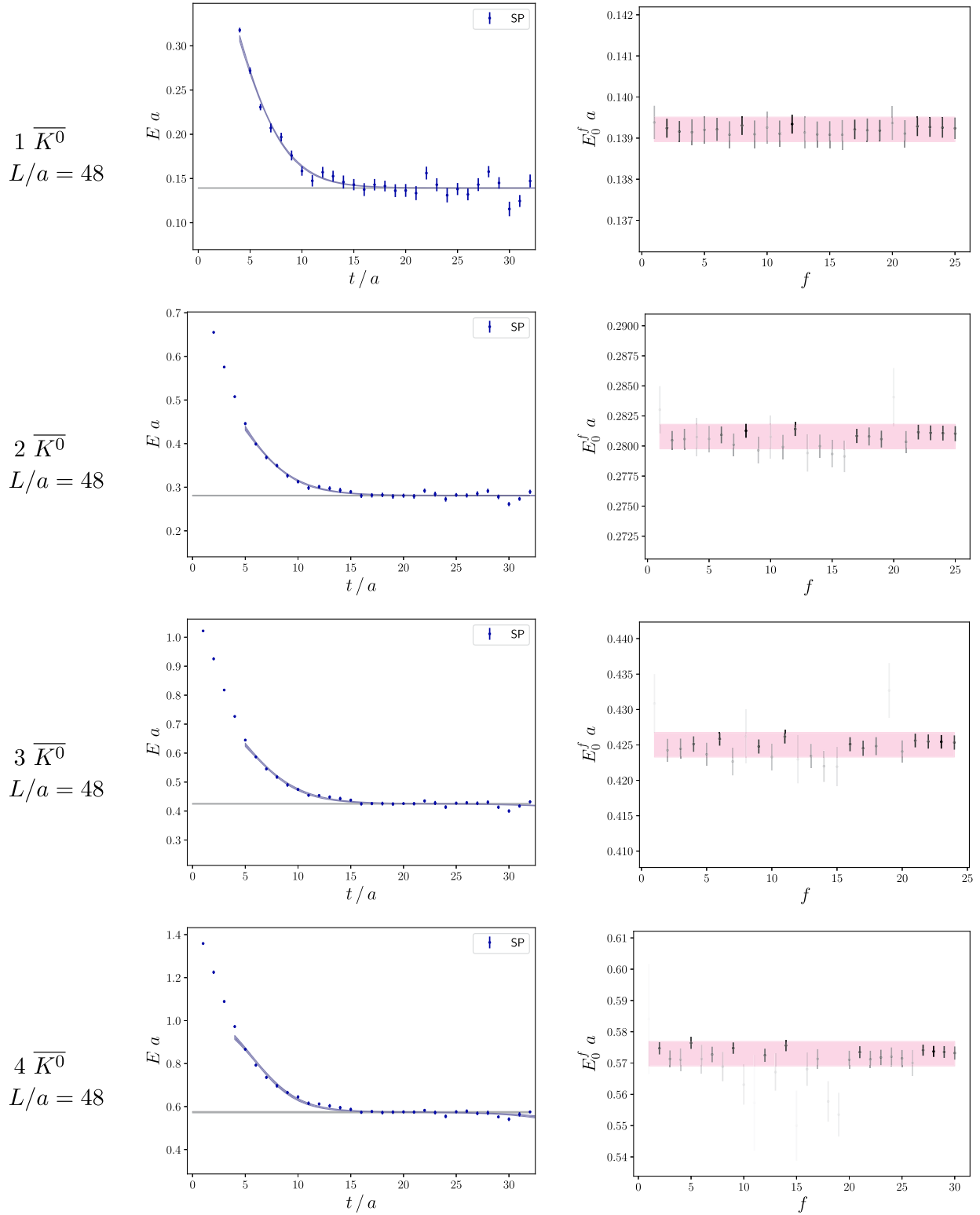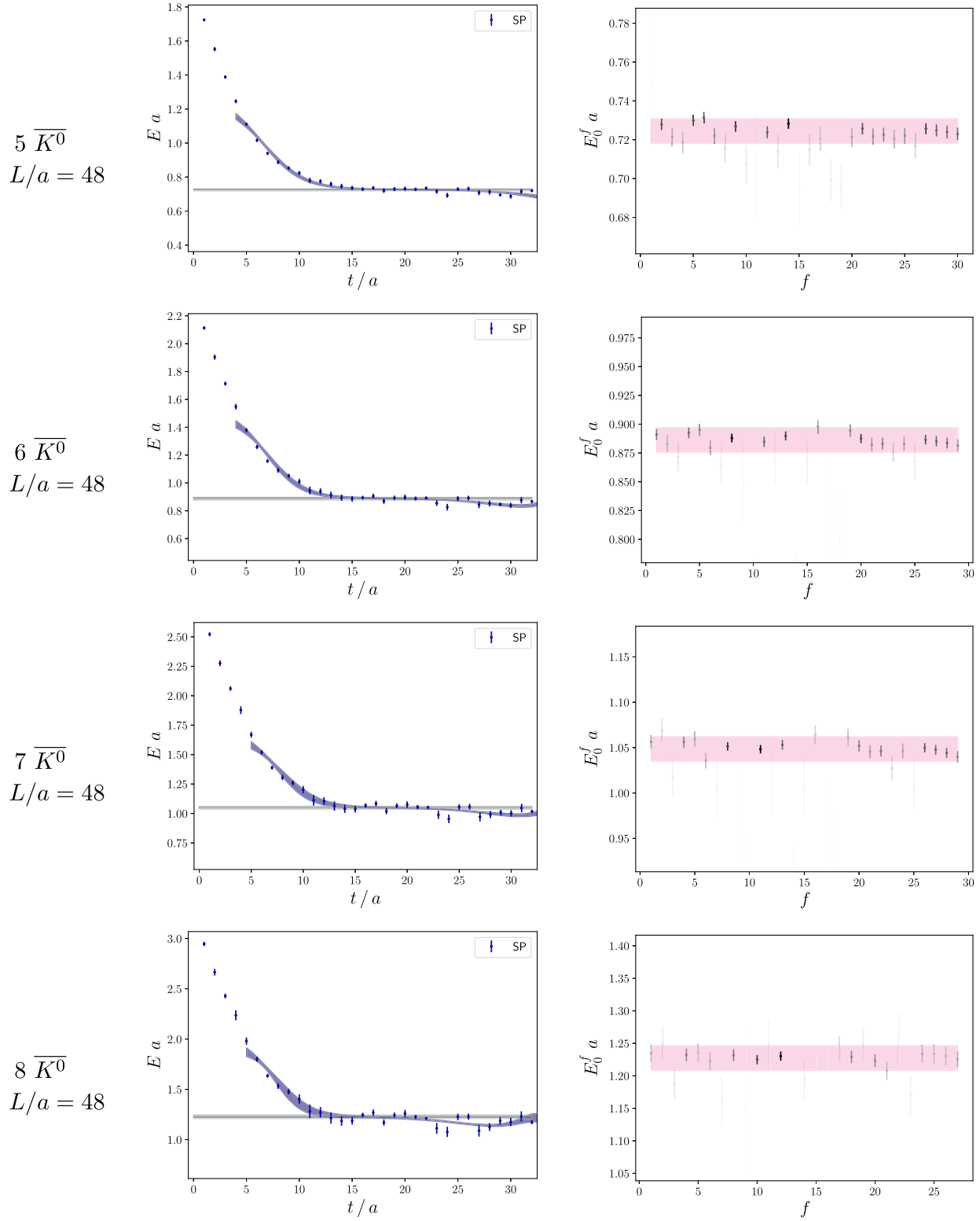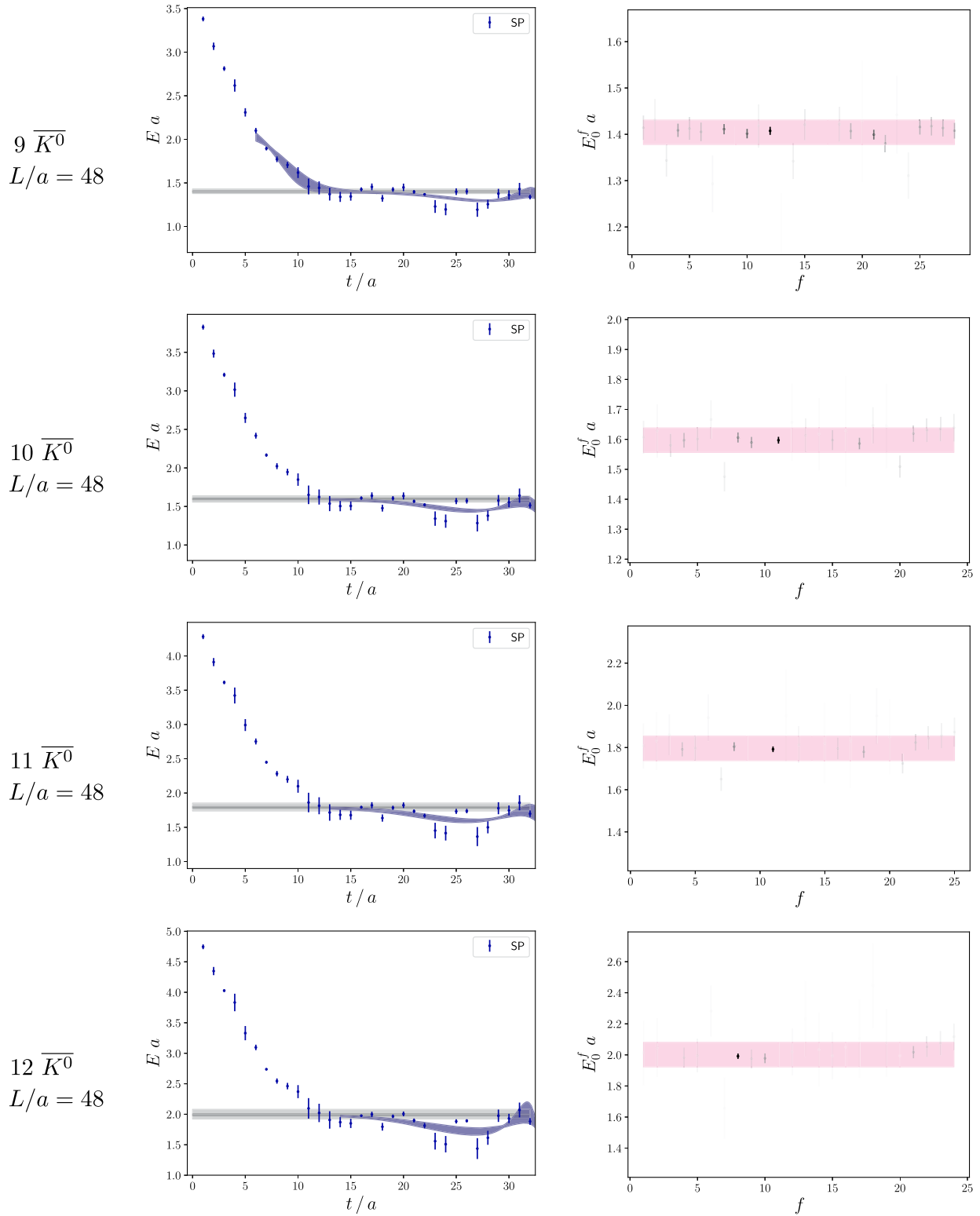
FIG. 18.   Fit results for systems of $n \in \{5, \dots, 8\}\pi^+$ mesons for the $L/a = 32$ lattice volume. The figures are analogous to Fig. 1, see Appendix B for a definition of the fitting procedure employed.
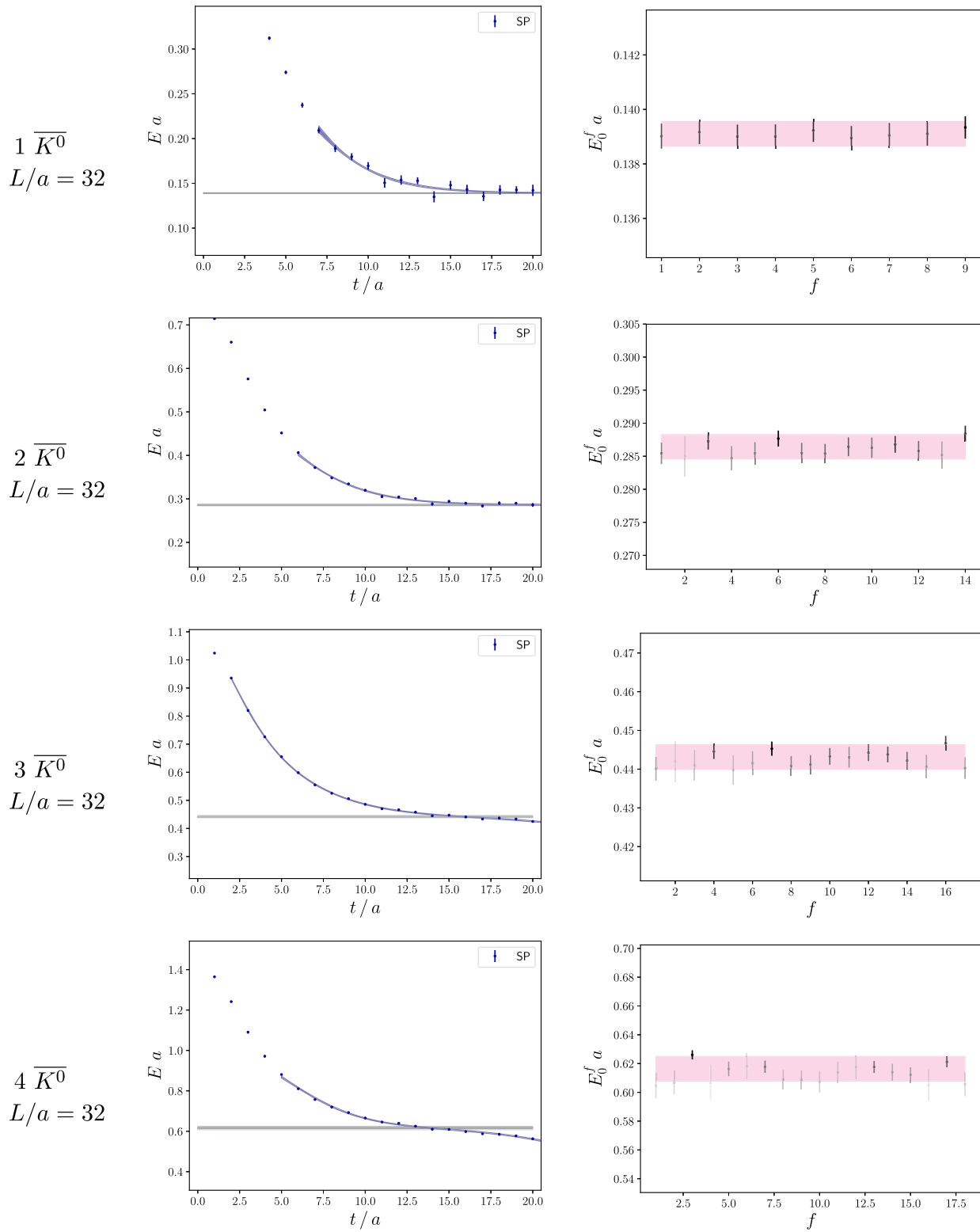
FIG. 19.   Fit results for systems of $n \in \{9, \ldots, 12\} \pi^+$ mesons for the $L/a = 32$ lattice volume. The figures are analogous to Fig. 1, see Appendix B for a definition of the fitting procedure employed.
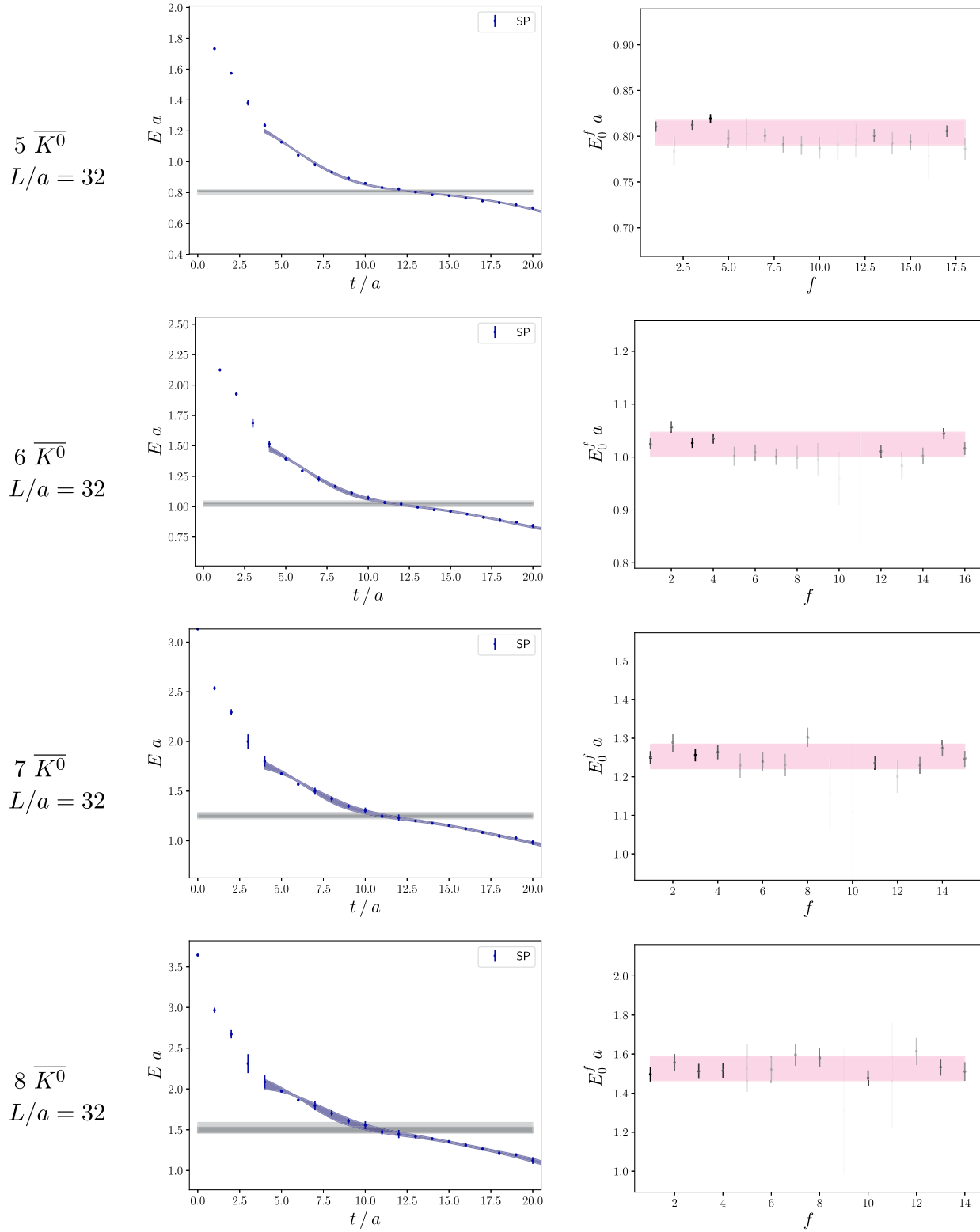
FIG. 20.   Fit results for systems of $n \in \{1, \ldots, 4\}$ $\overline{K^0}$ mesons for the $L/a = 48$ lattice volume. The figures are analogous to Fig. 1, see Appendix B for a definition of the fitting procedure employed.

FIG. 21.   Fit results for systems of $n \in \{5, ..., 8\}$ $\overline{K^0}$ mesons for the $L/a = 48$ lattice volume. The figures are analogous to Fig. 1, see Appendix B for a definition of the fitting procedure employed.
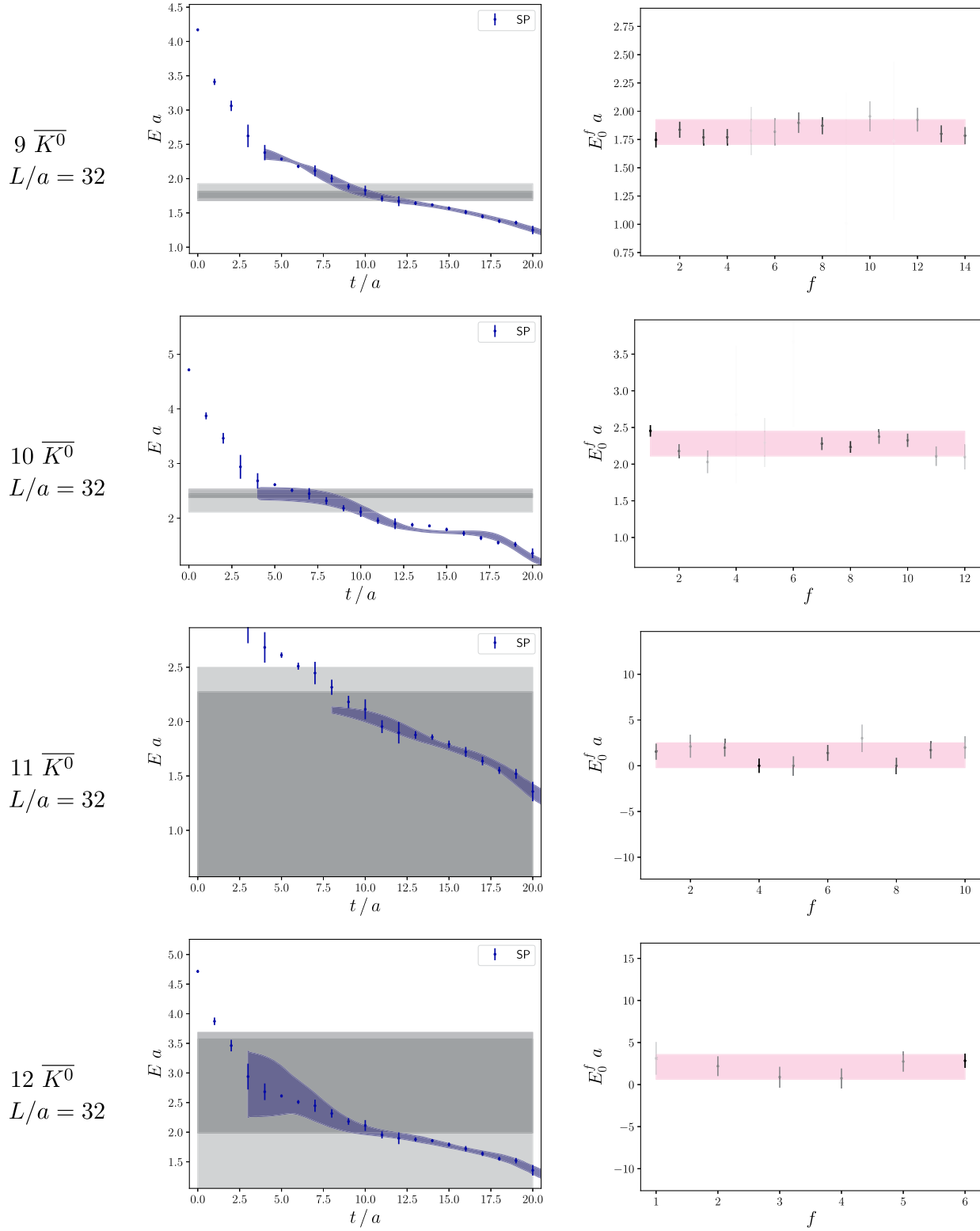
FIG. 22.   Fit results for systems of $n \in \{9, \ldots, 12\} \, \overline{K^0}$ mesons for the $L/a = 48$ lattice volume. The figures are analogous to Fig. 1, see Appendix B for a definition of the fitting procedure employed.

FIG. 23.   Fit results for systems of $n \in \{1, \ldots, 4\}\ \overline{K^0}$ mesons for the $L/a = 32$ lattice volume. The figures are analogous to Fig. 1, see Appendix B for a definition of the fitting procedure employed.
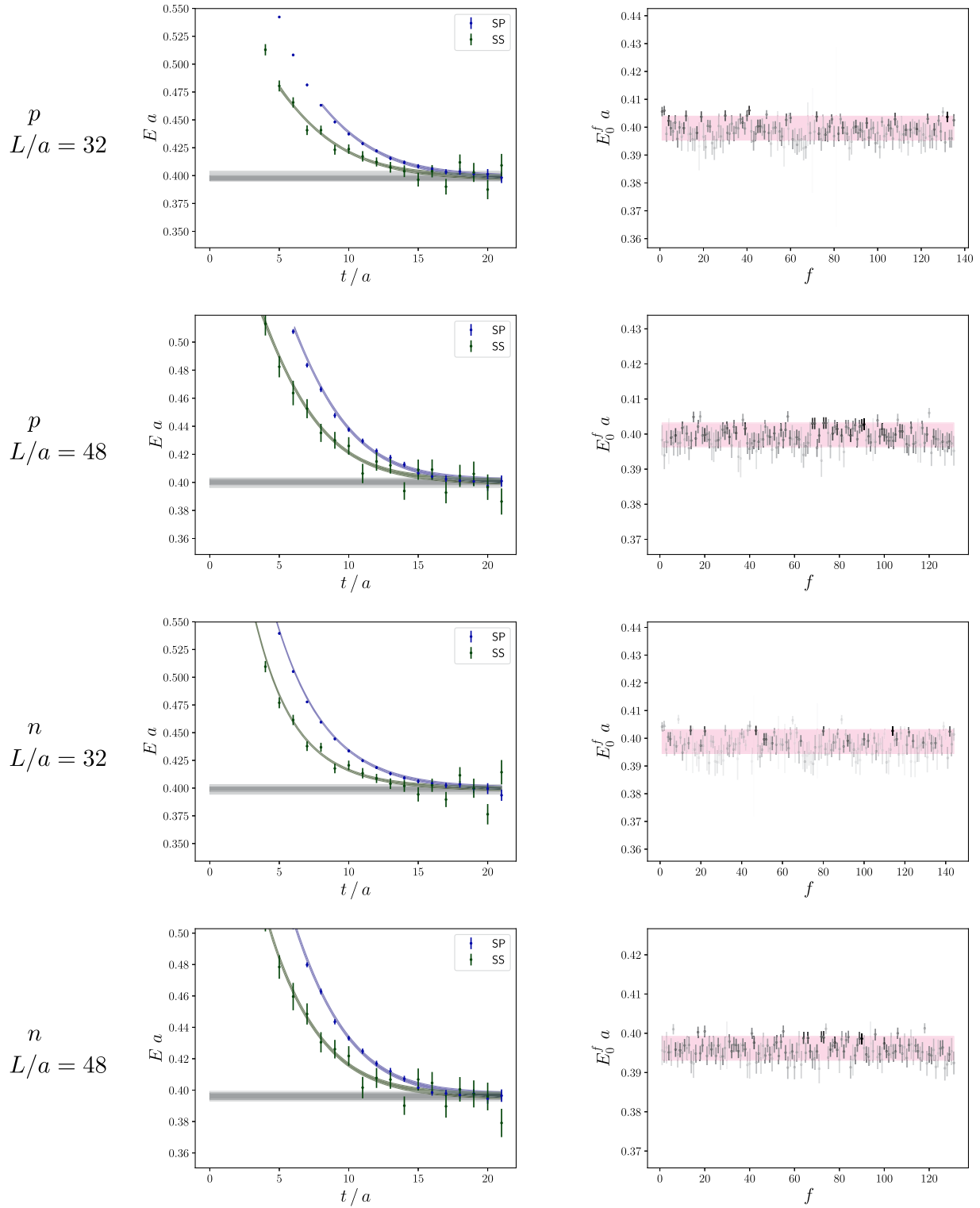
FIG. 24.   Fit results for systems of $n \in \{5, \ldots, 8\}$ $\overline{K^0}$ mesons for the $L/a = 32$ lattice volume. The figures are analogous to Fig. 1, see Appendix B for a definition of the fitting procedure employed.

FIG. 25. Fit results for systems of $n \in \{9, \ldots, 12\}$ $\overline{K^0}$ mesons for the $L/a = 32$ lattice volume. The figures are analogous to Fig. 1, see Appendix B for a definition of the fitting procedure employed.

FIG. 26. Fit results for proton and neutron systems. The figures are analogous to Fig. 1, see Appendix B for a definition of the fitting procedure employed.
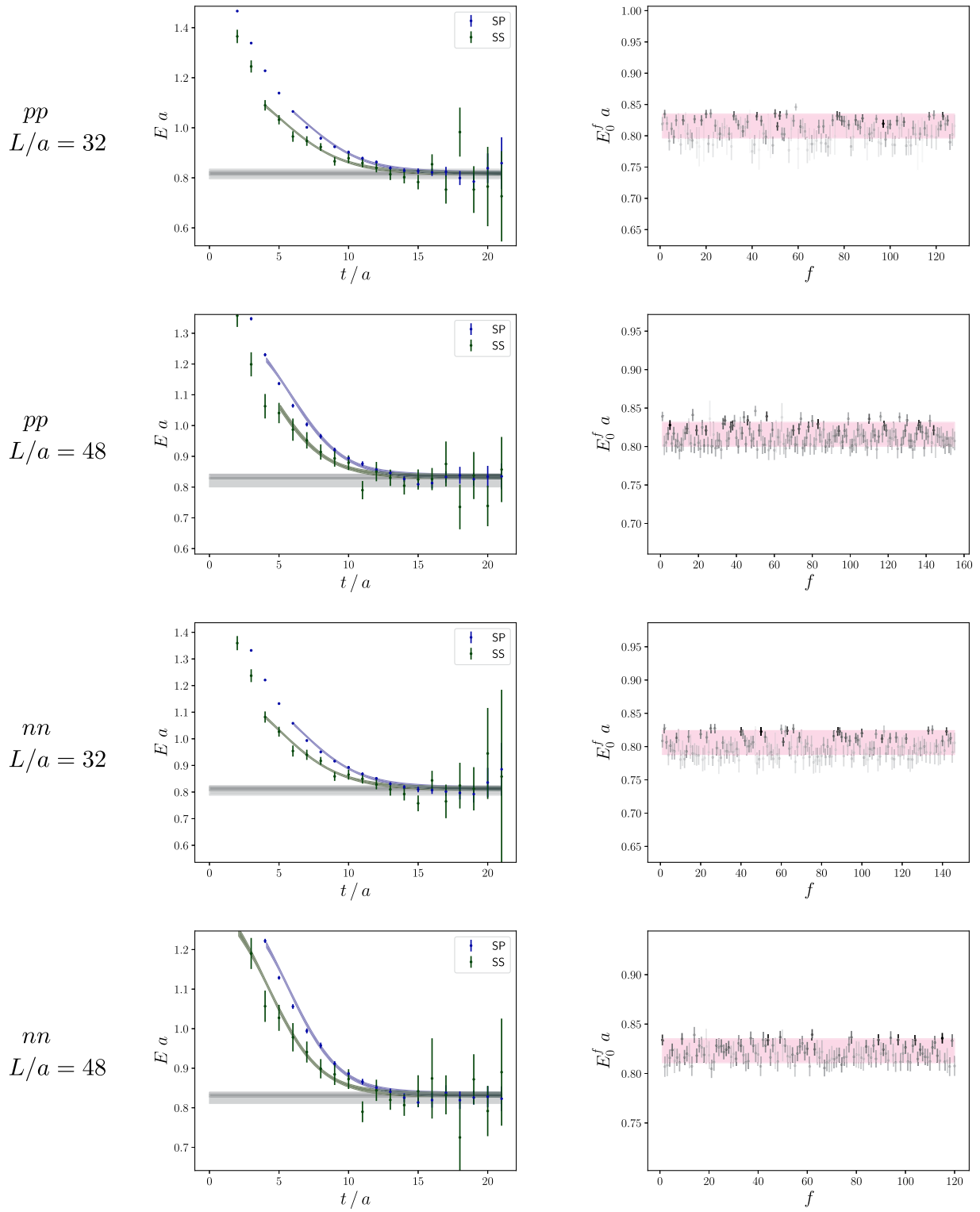
FIG. 27.   Fit results for systems of two protons and systems of two neutrons. The figures are analogous to Fig. 1, see Appendix B for a definition of the fitting procedure employed.
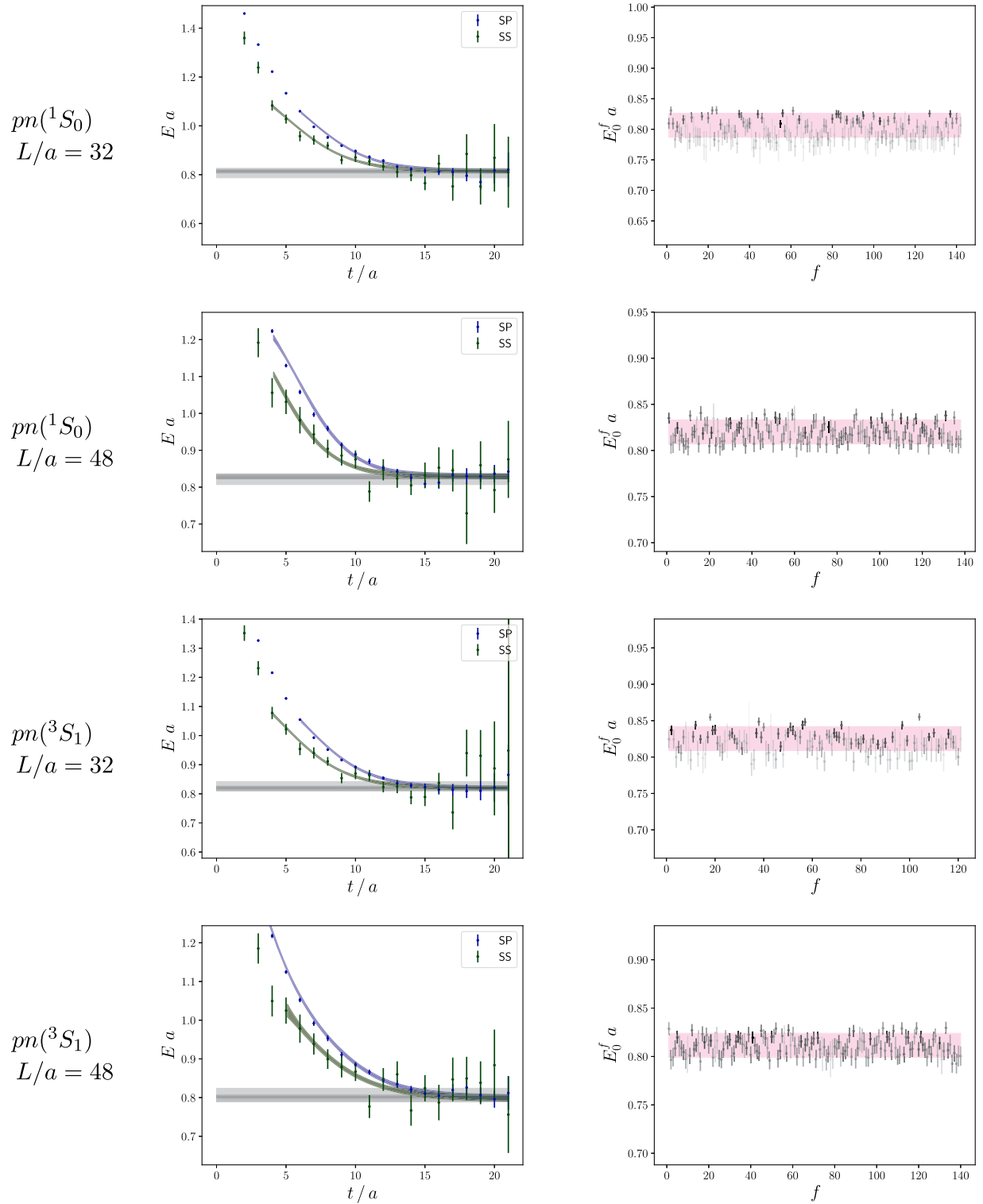
FIG. 28. Fit results for systems of one neutron and one proton in the cubic irreps associated with $^{3}S_1$ and $^{1}S_0$ systems in the infinite-volume limit. The figures are analogous to Fig. 1, see Appendix B for a definition of the fitting procedure employed.
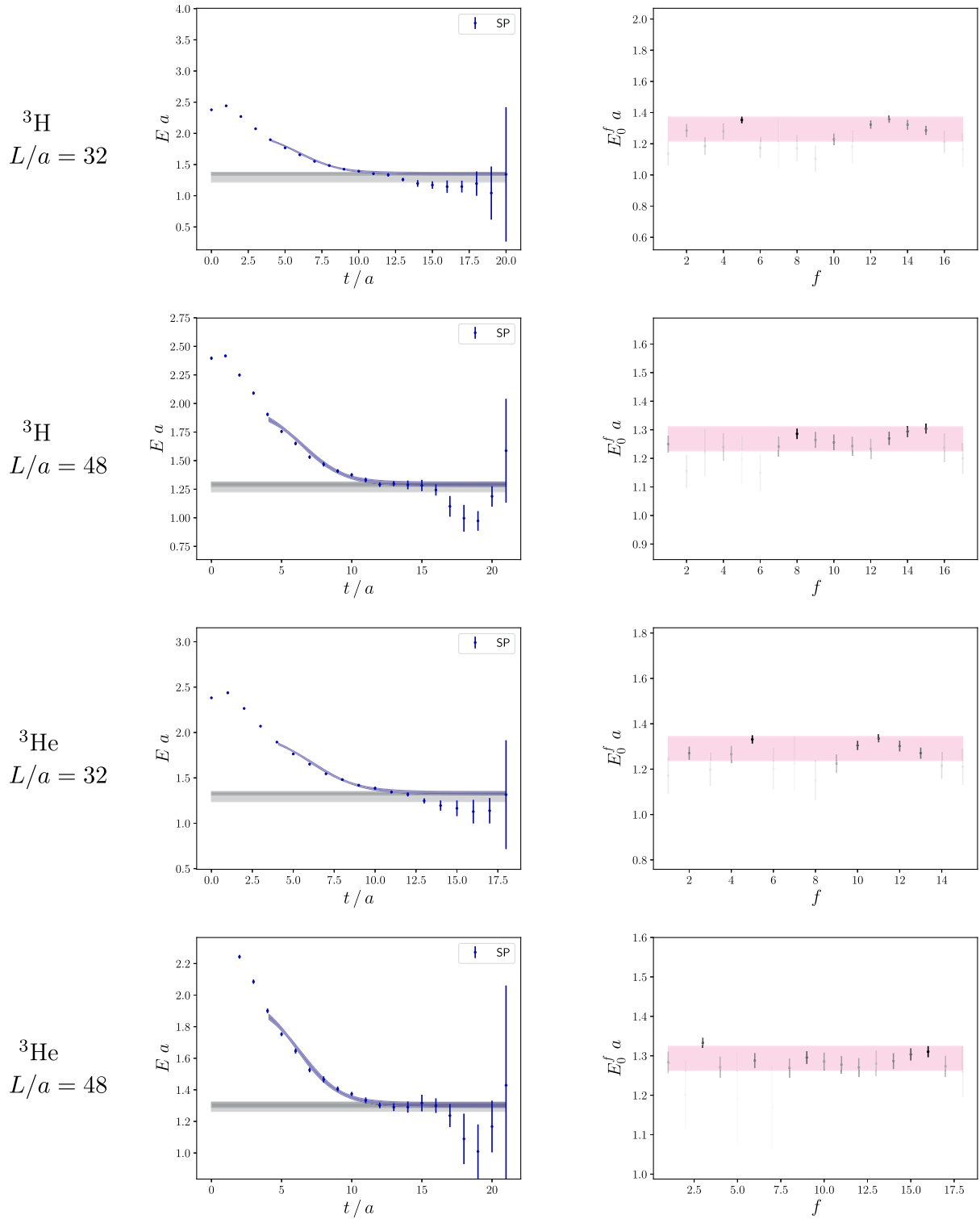
FIG. 29.   Fit results for three-nucleon systems ^{3}H and ^{3}He. The figures are analogous to Fig. 1, see Appendix B for a definition of the fitting procedure employed.

[1] S. Borsanyi *et al.* (Budapest-Marseille-Wuppertal), Phys. Rev. Lett. **111,** 252001 (2013).

[2] S. Borsanyi *et al.,* Science **347,** 1452 (2015).

[3] R. Horsley *et al.,* J. Phys. G **43,** 10LT02 (2016).

[4] R. Horsley *et al.,* J. High Energy Phys. 04 (2016) 093.

[5] S. Basak *et al.* (MILC Collaboration), Phys. Rev. D **99,** 034503 (2019).

[6] R. Horsley *et al.* (CSSM, QCDSF, UKQCD Collaborations), J. Phys. G **46,** 115004 (2019).

[7] Z. R. Kordov, R. Horsley, Y. Nakamura, H. Perlt, P. E. L. Rakow, G. Schierholz, H. Stüben, R. D. Young, and J. M. Zanotti (CSSM/QCDSF/UKQCD Collaborations), Phys. Rev. D **101,** 034517 (2020).

[8] V. Lubicz, G. Martinelli, C. T. Sachrajda, F. Sanfilippo, S. Simula, and N. Tantalo, Phys. Rev. D **95,** 034504 (2017).

[9] D. Giusti, V. Lubicz, G. Martinelli, C. T. Sachrajda, F. Sanfilippo, S. Simula, N. Tantalo, and C. Tarantino, Phys. Rev. Lett. **120,** 072001 (2018).

[10] M. Di Carlo, D. Giusti, V. Lubicz, G. Martinelli, C. T. Sachrajda, F. Sanfilippo, S. Simula, and N. Tantalo, Phys. Rev. D **100,** 034514 (2019).

[11] T. Blum, S. Chowdhury, M. Hayakawa, and T. Izubuchi, Phys. Rev. Lett. **114,** 012001 (2015).

[12] T. Blum, N. Christ, M. Hayakawa, T. Izubuchi, L. Jin, C. Jung, and C. Lehner, Phys. Rev. D **96,** 034515 (2017).

[13] S. Borsanyi *et al.* (Budapest-Marseille-Wuppertal Collaboration), Phys. Rev. Lett. **121,** 022002 (2018).

[14] P. Boyle, V. Gülpers, J. Harrison, A. Jüttner, C. Lehner, A. Portelli, and C. T. Sachrajda, J. High Energy Phys. 09 (2017) 153.

[15] D. Giusti, V. Lubicz, G. Martinelli, F. Sanfilippo, and S. Simula, J. High Energy Phys. 10 (2017) 157.

[16] T. Blum, P. A. Boyle, V. Gülpers, T. Izubuchi, L. Jin, C. Jung, A. Jüttner, C. Lehner, A. Portelli, and J. T. Tsang (RBC UKQCD Collaborations), Phys. Rev. Lett. **121,** 022003 (2018).

[17] J. Bijnens, J. Harrison, N. Hermansson-Truedsson, T. Janowski, A. Jüttner, and A. Portelli, Phys. Rev. D **100,** 014508 (2019).

[18] T. Blum, N. Christ, M. Hayakawa, T. Izubuchi, L. Jin, C. Jung, and C. Lehner, Phys. Rev. Lett. **124,** 132002 (2020).

[19] D. Giusti, V. Lubicz, G. Martinelli, F. Sanfilippo, and S. Simula, Phys. Rev. D **99,** 114502 (2019).

[20] S. Borsanyi *et al.,* arXiv:2002.12347.

[21] P. Schwerdtfeger, L. F. Pasteka, A. Punnett, and P. O. Bowman, Nucl. Phys. **A944,** 551 (2015).

[22] W. Detmold, R. G. Edwards, J. J. Dudek, M. Engelhardt, H.-W. Lin, S. Meinel, K. Orginos, and P. Shanahan (USQCD Collaboration), Eur. Phys. J. A **55,** 193 (2019).

[23] A. Duncan, E. Eichten, and H. Thacker, Phys. Rev. Lett. **76,** 3894 (1996).

[24] A. Duncan, E. Eichten, and R. Sedgewick, Phys. Rev. D **71,** 094509 (2005).

[25] T. Blum, T. Doi, M. Hayakawa, T. Izubuchi, and N. Yamada, Phys. Rev. D **76,** 114508 (2007).

[26] M. Hayakawa and S. Uno, Prog. Theor. Phys. **120,** 413 (2008).

[27] T. Blum, R. Zhou, T. Doi, M. Hayakawa, T. Izubuchi, S. Uno, and N. Yamada, Phys. Rev. D **82,** 094508 (2010).

[28] S. Aoki *et al.,* Phys. Rev. D **86,** 034507 (2012).

[29] N. Tantalo, Proc. Sci., LATTICE2013 (**2014**) 007 [arXiv: 1311.2797].

[30] Z. Davoudi and M. J. Savage, Phys. Rev. D **90,** 054503 (2014).

[31] M. G. Endres, A. Shindler, B. C. Tiburzi, and A. Walker-Loud, Phys. Rev. Lett. **117,** 072002 (2016).

[32] Z. Fodor, C. Hoelbling, S. D. Katz, L. Lellouch, A. Portelli, K. K. Szabo, and B. C. Toth, Phys. Lett. B **755,** 245 (2016).

[33] B. Lucini, A. Patella, A. Ramos, and N. Tantalo, J. High Energy Phys. 02 (2016) 076.

[34] Z. Fodor, C. Hoelbling, S. Krieg, L. Lellouch, T. Lippert, A. Portelli, A. Sastre, K. K. Szabo, and L. Varnhorst, Phys. Rev. Lett. **117,** 082001 (2016).

[35] M. Hansen, B. Lucini, A. Patella, and N. Tantalo, J. High Energy Phys. 05 (2018) 146.

[36] M. E. Matzelle and B. C. Tiburzi, Phys. Rev. D **95,** 094510 (2017).

[37] A. Patella, Proc. Sci., LATTICE2016 (**2017**) 020 [arXiv: 1702.03857].

[38] Z. Davoudi, J. Harrison, A. Jüttner, A. Portelli, and M. J. Savage, Phys. Rev. D **99,** 034510 (2019).

[39] J.-W. Lee and B. C. Tiburzi, Phys. Rev. D **93,** 034012 (2016).

[40] M. Lüscher, Commun. Math. Phys. **105,** 153 (1986).

[41] M. Lüscher, Nucl. Phys. **B354,** 531 (1991).

[42] R. A. Briceño, J. J. Dudek, and R. D. Young, Rev. Mod. Phys. **90,** 025001 (2018).

[43] S. R. Beane and M. J. Savage, Phys. Rev. D **90,** 074511 (2014).

[44] K. Symanzik, Nucl. Phys. **B226,** 187 (1983).

[45] M. Lüscher and P. Weisz, Commun. Math. Phys. **97,** 59 (1985); **98,** 433(E) (1985).

[46] W. Bietenholz *et al.,* Phys. Rev. D **84,** 054509 (2011).

[47] C. Morningstar and M. J. Peardon, Phys. Rev. D **69,** 054501 (2004).

[48] B. Sheikholeslami and R. Wohlert, Nucl. Phys. **B259,** 572 (1985).

[49] N. Cundy *et al.,* Phys. Rev. D **79,** 094507 (2009).

[50] R. F. Dashen, Phys. Rev. **183,** 1245 (1969).

[51] M. Göckeler, R. Horsley, P. E. L. Rakow, G. Schierholz, and R. Sommer, Nucl. Phys. **B371,** 713 (1992).

[52] C. R. Allton *et al.* (UKQCD Collaboration), Phys. Rev. D **47,** 5128 (1993).

[53] S. R. Beane, W. Detmold, T. C. Luu, K. Orginos, M. J. Savage, and A. Torok, Phys. Rev. Lett. **100,** 082004 (2008).

[54] W. Detmold, M. J. Savage, A. Torok, S. R. Beane, T. C. Luu, K. Orginos, and A. Parreño, Phys. Rev. D **78,** 014507 (2008).

[55] W. Detmold and M. J. Savage, Phys. Rev. D **82,** 014511 (2010).

[56] W. Detmold and B. Smigielski, Phys. Rev. D **84,** 014508 (2011).

[57] W. Detmold, K. Orginos, and Z. Shi, Phys. Rev. D **86,** 054507 (2012).

[58] W. Detmold and K. Orginos, Phys. Rev. D **87,** 114512 (2013).

[59] S. R. Beane, E. Chang, S. D. Cohen, W. Detmold, H. W. Lin, T. C. Luu, K. Orginos, A. Parreño, M. J. Savage, and A. Walker-Loud (NPLQCD Collaboration), Phys. Rev. D **87,** 034506 (2013).

[60] C. Stein, in *Proceedings of the Third Berkeley Symposium on Mathematical Statistics and Probability*, Volume 1: Contributions to the Theory of Statistics (University of California Press, Berkeley, Calif., 1956), pp. 197–206, https://projecteuclid.org/euclid.bsmsp/1200501656.

[61] O. Ledoit and M. Wolf, J. Multivariate Anal. **88**, 365 (2004).

[62] E. Rinaldi, S. Syritsyn, M. L. Wagman, M. I. Buchoff, C. Schroeder, and J. Wasem, Phys. Rev. D **99**, 074510 (2019).

[63] U. van Kolck, Nucl. Phys. **A645**, 273 (1999).

[64] J.-W. Chen, G. Rupak, and M. J. Savage, Nucl. Phys. **A653**, 386 (1999).

[65] H. A. Bethe, Phys. Rev. **76**, 38 (1949).

[66] X. Kong and F. Ravndal, Phys. Lett. B **450**, 320 (1999); **458**, 565(E) (1999).

[67] X. Kong and F. Ravndal, Nucl. Phys. **A665**, 137 (2000).

[68] K. Huang and C. N. Yang, Phys. Rev. **105**, 767 (1957).

[69] S. R. Beane, W. Detmold, and M. J. Savage, Phys. Rev. D **76**, 074507 (2007).

[70] W. Detmold and M. J. Savage, Phys. Rev. D **77**, 057502 (2008).

[71] M. H. Namjoo, A. H. Guth, and D. I. Kaiser, Phys. Rev. D **98**, 016011 (2018).

[72] E. Braaten, A. Mohapatra, and H. Zhang, Phys. Rev. D **98**, 096012 (2018).

[73] M. T. Hansen and S. R. Sharpe, Phys. Rev. D **93**, 014506 (2016).

[74] W. E. Caswell and G. P. Lepage, Phys. Lett. **167B**, 437 (1986).

[75] A. Pineda and J. Soto, Nucl. Phys. B, Proc. Suppl. **64**, 428 (1998).

[76] A. Pineda and J. Soto, Phys. Rev. D **59**, 016005 (1998).

[77] M. Göckeler, R. Horsley, M. Lage, U.-G. Meissner, P. Rakow, A. Rusetsky, G. Schierholz, and J. Zanotti, Phys. Rev. D **86**, 094513 (2012).

[78] L. Leskovec and S. Prelovsek, Phys. Rev. D **85**, 114507 (2012).

[79] M. T. Hansen and S. R. Sharpe, Phys. Rev. D **93**, 096006 (2016); **96**, 039901(E) (2017).

[80] T. Mehen and I. W. Stewart, Nucl. Phys. **A665**, 164 (2000).

[81] S. R. Beane, W. Detmold, H.-W. Lin, T. C. Luu, K. Orginos, M. J. Savage, A. Torok, and A. Walker-Loud (NPLQCD Collaboration), Phys. Rev. D **81**, 054505 (2010).

[82] S. R. Beane, E. Chang, W. Detmold, H. W. Lin, T. C. Luu, K. Orginos, A. Parreño, M. J. Savage, A. Torok, and A. Walker-Loud (NPLQCD Collaboration), Phys. Rev. D **85**, 054511 (2012).

[83] T. Yamazaki, K.-I. Ishikawa, Y. Kuramashi, and A. Ukawa, Phys. Rev. D **86**, 074514 (2012).

[84] S. R. Beane *et al.* (NPLQCD Collaboration), Phys. Rev. C **88**, 024003 (2013).

[85] K. Orginos, A. Parreño, M. J. Savage, S. R. Beane, E. Chang, and W. Detmold, Phys. Rev. D **92**, 114512 (2015).

[86] E. Berkowitz, T. Kurth, A. Nicholson, B. Joó, E. Rinaldi, M. Strother, P. M. Vranas, and A. Walker-Loud, Phys. Lett. B **765**, 285 (2017).

[87] T. Yamazaki, K.-I. Ishikawa, Y. Kuramashi, and A. Ukawa, Phys. Rev. D **92**, 014501 (2015).

[88] M. L. Wagman, F. Winter, E. Chang, Z. Davoudi, W. Detmold, K. Orginos, M. J. Savage, and P. E. Shanahan, Phys. Rev. D **96**, 114510 (2017).

[89] T. D. Blanton, F. Romero-López, and S. R. Sharpe, Phys. Rev. Lett. **124**, 032001 (2020).

[90] J. Bijnens, G. Colangelo, G. Ecker, J. Gasser, and M. E. Sainio, Nucl. Phys. **B508**, 263 (1997); **517**, 639(E) (1998).

[91] M. Tanabashi *et al.* (Particle Data Group), Phys. Rev. D **98**, 030001 (2018).

[92] https://itconnect.uw.edu/research/hpc/.

[93] T. R. Haar, Y. Nakamura, and H. Stüben, EPJ Web Conf. **175**, 14011 (2018).

[94] R. G. Edwards and B. Joó (SciDAC LHPC, UKQCD Collaborations), Nucl. Phys. B, Proc. Suppl. **140**, 832 (2005).

[95] G. Parisi, Phys. Rep. **103**, 203 (1984).

[96] G. P. Lepage, in *Boulder TASI 1989:97-120* (World Scientific, Singapore, 1989), pp. 97–120.

[97] M. L. Wagman and M. J. Savage, Phys. Rev. D **96**, 114508 (2017).

[98] M. Lüscher and P. Weisz, Nucl. Phys. **B240**, 349 (1984).

[99] G. Golub and V. Pereyra, Inverse Probl. **19**, R1 (2003).

[100] D. P. O'Leary and B. W. Rust, Comput. Optim. Applic. **54**, 579 (2013).

[101] H. Akaike, IEEE Trans. Autom. Control **19**, 716 (1974).

[102] P. Young, arXiv:1210.3781.

[103] A. C. Davison and D. V. Hinkley, *The Basic Bootstraps* (Cambridge University Press, Cambridge, England, 1997), p. 11–69, Cambridge Series in Statistical and Probabilistic Mathematics.

[104] J. Bezanson, A. Edelman, S. Karpinski, and V. B. Shah, SIAM Rev. **59**, 65 (2017).

[105] P. K. Mogensen and A. N. Riseth, J. Open Source Software **3**, 615 (2018).